Global Analysis of a Reflectometry Database for Systematic Study of Plasma Turbulence in Tokamaks

Yan Sun

Doctoral School Chemistry-Mechanics-Materials-Physics

European Doctoral School FUSION-DC

Doctoral thesis

Global Analysis of a Reflectometry Database for Systematic Study of Plasma Turbulence in Tokamaks

Yan Sun

Jury members for public defense on June 13^{th}, 2019:

Prof. Michel VERGNAT	Chair – U of Lorraine
Dr. Pascale HENNEQUIN	Referee – École Polytechnique & DR CNRS
Prof. Stefano CODA	Referee – EPFL
Dr. Sébastien HACQUIN	Examiner – IRFM-CEA
Prof. Filip DE TURCK	Examiner – UGent
Prof. Stéphane HEURAUX	Thesis director – U of Lorraine
Dr. Roland SABOT	Thesis co-director – IRFM-CEA
Prof. Geert VERDOOLAEGE	Thesis co-director – UGent & LPP-ERM/KMS
Prof. Toon VERSTRAELEN	Invited – UGent

Global Analysis of a Reflectometry Database for Systematic Study of Plasma Turbulence in Tokamaks

SUN Yan (孙彦)

Ph.D. Promoters and Supervisors:

Dr. Roland SABOT	IRFM, CEA Cadarache
Prof. Stéphane HEURAUX	University of Lorraine
Prof. Geert VERDOOLAEGE	Ghent University & LPP-ERM/KMS
Dr. Grégoire HORNUNG	Ghent University
Dr. Sébastien HACQUIN	IRFM, CEA Cadarache

This thesis has been funded by:
The Erasmus Mundus International Doctoral College in
Fusion Science and Engineering (FUSION-DC) & CEA & Ghent University

Main laboratories (Jan 2016 – May 2019):
Institute for Magnetic Fusion Research, CEA Cadarache, France
Department of Applied Physics, Ghent University, Belgium (Apr 2016 – Jan 2017)

Summary

Magnetic confinement nuclear fusion research aims at the development of a clean, safe and inexhaustible source of baseload electric power. Based on the energy released during fusion of light nuclei of hydrogen isotopes in a hot tokamak plasma, its realization depends crucially on the ability to regulate the transport of energy and particles through the plasma. It is now known that the main contribution to transport in tokamak plasmas is due to small-scale turbulence, hence understanding and control of the turbulent transport is key to achieve the desired confinement properties. In the core region of tokamak plasmas, drift-wave turbulence is mainly caused by two types of micro-instabilities: the so-called trapped electron modes (TEM) and the ion temperature gradient (ITG) modes. Considerable research efforts are directed towards understanding turbulence properties under varying plasma conditions. The degree of collisionality of the plasma is known to affect the dominating instability, since particles trapped in their motion by the magnetic well tend to be detrapped by collisions. Shedding more light on these mechanisms is one of the key purposes of this thesis.

Among the different turbulence diagnostic tools, reflectometry is a radar-like technique, used in this PhD work, which is based on detecting the properties of microwaves reflected by the plasma. Reflectometry allows to detect fluctuations of the plasma density with a high spatial resolution. In particular, standard fixed-frequency reflectometry has been extensively utilized to extract spectral characteristics and correlation properties

of turbulent fluctuations, as well as their link with the micro-instabilities and the turbulent transport.

In fusion science, most experimental studies are set up according to a carefully chosen set of plasma conditions, and attempt to vary, in a controlled way, one or a few plasma parameters at a time, in order to investigate the effect on some plasma phenomenon of interest. In contrast, in this work a large database of reflectometry measurements from the Tore Supra tokamak has been created, and specialized tools have been developed to detect patterns in the data, persisting across a broad range of plasma conditions. The database includes 350,000 spectra from 6,000 discharges in basic Ohmic operation, and in the so-called low-confinement mode (L-mode) plasmas, which are heated by means of auxiliary heating systems. The aim was to extract general trends of turbulence properties, and link them to the occurrence and behavior of the micro-instabilities driving the turbulence, hence contributing to the understanding of plasma turbulence.

To accomplishing these goals, a key ingredient is a proper quantification of the fixed-frequency reflectometry power spectra. A robust spectrum quantification scheme enables standardization, which in turn allows the kind of systematization envisaged in this work. Each spectrum in our Tore Supra database was decomposed into four components: the direct current (DC) component, the low-frequency (LF) fluctuations, the broadband (BB) turbulence and the noise level. Various parametrization functions were tested and compared to determine the optimal spectrum fit, with adequate robustness properties in the presence of a large variety of spectrum shapes and plasma conditions. The

components of the spectra at low frequencies, including the DC and LF components, were fitted by two Gaussian functions, and the noise was fitted by one constant parameter. The BB component represents the energy distribution of turbulence in the frequency domain and may assume a variety of shapes (Gaussian, Lorentzian, etc.) under different plasma conditions. For the BB component, three different fit models (generalized Gaussian, Voigt and Taylor) were compared quantitatively using a large number of spectra. This indicated excellent performance of the generalized Gaussian (GG) model, followed by the Taylor model. On the other hand, the parameters of the Taylor model are more amenable to physical interpretation.

Equipped with a robust spectrum parametrization method, the spectral parameters (width, shape and contribution) of the BB and LF components from both the GG and the Taylor model provide quantitative information about the turbulence properties. The most straightforward spectral characteristic is the BB contribution of the spectra (E_{BB}). The full radial profile of the BB component has been investigated at different edge safety factors (q_ψ), a crucial dimensionless parameter determining the plasma stability, in both Ohmic and L-mode plasmas. In Ohmic plasmas, a remarkable reduction of E_{BB}, referred to as the E_{BB} basin, was systematically observed near the central region. Further investigation revealed a direct link between the E_{BB} basin and the $q = 1$ surface. This is related to the occurrence of magnetohydrodynamic instabilities known as sawteeth. Specifically, E_{BB} was considerably reduced ($E_{\mathrm{BB}} < 0.2$) inside the $q = 1$ surface and the width of the E_{BB} basin was found to be approximately proportional to the $q = 1$ position. Outside the $q = 1$

surface, E_{BB} increases above 0.5 at both the low-field-side and high-field-side, however with a strong asymmetry. Discriminating between the linear Ohmic confinement (LOC) regime and the saturated Ohmic confinement (SOC) regime, it was discovered that E_{BB} in the SOC regime is systematically higher than in the LOC regime, throughout the entire plasma cross-section. In L-mode, we focused on plasmas with pure lower hybrid (LH) heating or pure ion cyclotron resonance heating (ICRH). In pure LH-heated plasmas, the E_{BB} basin was observed as well, at different heating powers (P_{heat}). However, with the same P_{heat} in pure ICRH plasmas, E_{BB} was found to be greatly enhanced, with a weak or disappearing broadband basin.

In the final part of the work, interpretation of the observations of the spectral trends across the database was treated. We focused on the collisional effects on different spectral characteristics in the various confinement regimes. In Ohmic plasmas, a general increase of E_{BB} with collisionality was observed at all radial positions. This global trend was seen to be consistent with gyrokinetic simulations reported in the literature. Specifically, a wider BB component was observed in the SOC regime (higher density or collisionality), compared to the LOC regime. This correspondence suggests a possible interpretation of the trends of the broadband width in terms of a transition of the dominating instability driving the turbulence. In particular, the TEM and ITG instabilities have been linked with the LOC and the SOC regimes, respectively. This possible interpretation was supported by further analysis of the LF component and the density peaking. In addition, other BB characteristics (width and shape) have also been studied to obtain a deeper understanding. In

L-mode plasmas, a similar trend of E_{BB} with collisionality was observed, suggesting a similar interpretation as in the Ohmic case. Again, this was supported by a global analysis of the LF component and the density peaking.

The main contribution of the present work has been to extend analysis of turbulence characteristics from reflectometry spectra to a broad range of plasma conditions in a large database. The standardization offered by this approach has enabled a systematic study of turbulence properties across the database. Various patterns were observed and could be linked to experimental observations or simulations carried out using a much reduced set of plasma conditions. This is the first demonstration in fusion science of systematic characterization of turbulence properties in such a large database. Additional confirmation of the link between the spectral trends and the dominating instability is to be provided by full-wave and gyrokinetic simulations. However, the present study has allowed to establish a number of important, robust trends of turbulence properties in tokamak plasmas, thus putting their interpretation on firmer ground.

Résumé étendu

La recherche sur la fusion nucléaire par confinement magnétique a pour but de développer une source d'énergie électrique propre, sûre et inépuisable. Basé sur l'énergie résultant de la fusion de noyaux d'isotopes d'hydrogène se produisant dans un plasma magnétisé chaud, la viabilité de cette source d'énergie dépend, de manière cruciale, de la maîtrise du transport d'énergie et de particules à travers le plasma. Il est maintenant connu que la principale contribution au transport dans les plasmas de tokamak est liée à la turbulence à petite échelle. Il est donc essentiel de comprendre et de contrôler le transport turbulent pour obtenir les propriétés de confinement souhaitées. Dans la région centrale des plasmas de tokamak, la turbulence associées aux ondes de dérive est principalement reliée à deux types de micro-instabilités: les modes appelés: mode d'électrons piégés (TEM) et les modes à gradient de température ionique (ITG). Beaucoup efforts en recherche sur les plasmas de fusion sont dévolus à la compréhension des propriétés de la turbulence pour diverses conditions plasma. Les collisions impactent l'instabilité dominante et le transport parce que d'une part les particules confinées dans la cage magnétique ont tendance à être éjectées par les collisions et d'autre part les collisions réduisent le nombre effectif de particules à l'origine des instabilités. La mise en évidence des différents régimes de turbulence liés aux différentes instabilités, et donc de transport, est l'un des objectifs principaux de cette thèse.

Parmi les différents moyens de diagnostic de la turbulence, la réflectométrie est une technique, de type radar, utilisée dans

cette thèse. Celle-ci repose sur la détection des propriétés des micro-ondes réfléchies par le plasma. La réflectométrie permet d'accéder aux fluctuations de la densité du plasma avec une résolution spatiale élevée. En particulier, la réflectométrie à fréquence fixe a été largement utilisée pour extraire les caractéristiques spectrales et les propriétés de corrélation des fluctuations turbulentes pour ensuite établir un lien entre les micro-instabilités et le transport turbulent.

En science de la fusion, la plupart des études expérimentales sont usuellement organisées en fonction d'un ensemble restreint de conditions plasma soigneusement choisies en tentant de faire varier de manière contrôlée un ou plusieurs paramètres plasma à la fois pour étudier l'effet de certains phénomènes plasma considérés comme pertinents. Dans ce travail de thèse une autre approche a été suivie en construisant une vaste base de données à partir de mesures de réflectométrie effectuées sur le tokamak Tore Supra. Pour cela des outils spécialisés ont été développés pour extraire les tendances globales persistantes dans l'ensemble des conditions plasma couvert par la base de données de Tore Supra. Cette base contient 350 000 spectres provenant de 6000 décharges qui sont, soit en régime "ohmique" où le chauffage est uniquement assuré par le courant plasma, soit mode à faible confinement (mode L) où un ou des systèmes de chauffage auxiliaires sont actifs. L'objectif initial était d'extraire les tendances globales des propriétés de la turbulence via une analyse systématique des données et de les relier à l'apparition et au comportement des micro-instabilités conduisant à la turbulence, contribuant ainsi à la compréhension de la turbulence plasma.

Pour atteindre ces objectifs, un élément clé est l'établissement

une paramétrisation appropriée du spectre en fréquence de réflectométrie de fluctuation. Un schéma robuste de quantification du spectre passe par une normalisation qui permet aussi une analyse systématique initialement prévue dans ce travail. Tous les spectres de notre base de données Tore Supra a été décomposé en quatre composantes: la composante de courant continu (CC) correspondant à l'onde réfléchie, les fluctuations de basse fréquence (BF), la turbulence à large bande (BB) et le niveau de bruit. Différentes fonctions génériques servant à la paramétrisation ont été testées et comparées pour déterminer l'ajustement optimal du spectre, avec des propriétés de robustesse adéquates en présence d'une grande variété de formes de spectre et de conditions plasma. Les composantes des spectres aux basses fréquences, y compris les composantes DC et BF, ont été ajustées par deux fonctions gaussiennes et le bruit par un paramètre constant. Le composant BB représente la distribution d'énergie de la turbulence dans le domaine fréquentiel et peut être identifié diverses fonctions génériques (gaussienne, lorentzienne, etc.) dans différentes conditions de plasma. Pour la composante BB, trois modèles d' ajustement différents (gaussien généralisé, Voigt et Taylor) ont été comparés quantitativement en utilisant un grand nombre de spectres. Cela indique une excellente performance du modèle gaussien généralisé (GG), suivi du modèle de Taylor. Par ailleurs, les paramètres du modèle de Taylor sont plus facilement interprétables en termes de différents effets physiques.

Dotés d' une méthode de paramétrisation spectrale robuste, les paramètres spectraux (largeur, forme et contribution) des composants BB et LF des modèles GG et Taylor fournissent des informations quantitatives sur les propriétés de turbulence. La

caractéristique spectrale la plus simple est la contribution des spectres à BB (E_{BB}). Le profil radial complet de la composante BB a été étudié pour différents facteurs de sécurité (q_ψ) évalués au voisinage de la dernière surface de flux magnétique fermée. Ce paramètre sans dimension est déterminant pour la stabilité des plasmas contenus dans la base de données. Dans les plasmas ohmiques, une réduction remarquable de E_{BB}, appelée bassin de E_{BB}, a été systématiquement observée près de la région centrale. Une analyse plus approfondie a révélé un lien direct entre le bassin E_{BB} et la surface $q = 1$. Ceci est lié à l'apparition d'instabilités magnétohydrodynamiques connues sous le nom de dents de scie. Plus précisément, E_{BB} est considérablement réduit ($E_{\mathrm{BB}} < 0,2$) à l'intérieur de la surface $q = 1$ et la largeur du bassin E_{BB} suit approximativement les positions de $q = 1$. En dehors de la surface $q = 1$, E_{BB} augmente au-dessus de $0,5$ tant du côté champ bas que du côté champ haut, mais avec une forte asymétrie. En recherchant les différences entre le régime de confinement ohmique linéaire (LOC) et le régime de confinement ohmique saturé (SOC), il a été découvert que E_{BB} dans le régime SOC est systématiquement plus élevé que dans le régime LOC, sur toute la traversée du plasma. En mode L, nous nous sommes concentrés sur les plasmas avec chauffage hybride inférieur pur (LH) ou chauffage par résonance cyclotron ionique pur (ICRH). Dans les plasmas chauffés par la LH, le bassin E_{BB} a également été observé pour différentes puissances de chauffage (P_{heat}). Cependant, avec le même P_{chaleur} dans les plasmas chauffés seulement par ICRH, E_{BB} s'est révélé être grandement amélioré, avec un bassin à large qui tend à disparaître.

Dans la dernière partie du travail, l'interprétation des ten-

dances spectrales observées dans la base de données a été abordée. Nous nous sommes concentrés sur les effets des collisions sur différentes caractéristiques spectrales dans les différents régimes de confinement. Dans les plasmas ohmiques, une augmentation générale de E_{BB} avec collision a été observée à toutes les positions radiales. Cette tendance globale a été jugée compatible avec les simulations gyrocinétiques rapportées dans la littérature. Plus précisément, une composante BB plus large a été observée dans le régime SOC (densité plus élevée ou collisionalité) par rapport au régime LOC. Cette correspondance suggère une interprétation possible des tendances de la largeur de bande large en termes de transition de l'instabilité dominante à l'origine de la turbulence. En particulier, les instabilités TEM et ITG ont été liées aux régimes LOC et SOC, respectivement. Cette interprétation possible a été basée par une analyse plus poussée de la composante de la FL et de la forme du profil de densité. De plus, d'autres caractéristiques de BB (largeur et forme) ont également été étudiées pour confirmer cette analyse. Dans les plasmas en mode L, une tendance similaire de E_{BB} avec une collisionalité a été observée, suggérant une interprétation similaire à celle des cas Ohmique. Là encore, cela a été confirmé par une analyse globale de la composante de la FL et de la forme du profil de densité.

La principale contribution du présent travail a été d'étendre l'analyse des caractéristiques de la turbulence des spectres en fréquence de réflectométrie à un large éventail de conditions plasma pour une base de données volumineuse. La standardisation offerte par cette approche permet une étude systématique des propriétés de turbulence dans une base de données qui pour-

rait être complémentaire à une analyse basée sur différents modèles restreints à des conditions plasma spécifiques correspondant à des observations expérimentales ciblées ou à des simulations. Il s'agit de la première démonstration en science de la fusion de la caractérisation systématique des propriétés de turbulence à partir d'une base de données regroupant plus de 10 années d'expériences. Une confirmation supplémentaire du lien entre les tendances spectrales et l'instabilité dominante devrait être apportée par des simulations couplant code de propagation d'ondes et code gyrocinétique. Malgré tout le travail qui reste à effectuer, ce travail de thèse a permis d' établir des tendances robustes de première importance concernant les propriétés de turbulence dans les plasmas de tokamak, confirmant l'interprétation existante à partir d'une analyse systématique originale.

Acknowledgements

During the last three years, many colleagues and other PhD students have given me lots of help and suggestions to my research work. I have gained valuable knowledge and experience from them, which are much more than the completion of this thesis.

First, I would like to give my thanks to my supervisors. Most of the time I work in IRFM, CEA Cadarache with Dr. Roland Sabot, as my thesis director, who has guided my work from the very beginning when he explained the details of the reflectometry and other diagnostics on Tore Supra to me with great patience. Even when I am in Belgium for months, we still has a regular meeting to discuss my progress. In particular, I am most impressed by his strong passion towards the scientific research and the interests to explore new problems. When I stayed in Ghent University in my first year to follow some courses, I worked directly with Dr. Grégiore Hornung and also under the supervision of Prof. dr. Geert Verdoolaege. Their initial envisions of applying the data science in the study of plasma turbulence has driven the systematic turbulence study of this thesis. Although Grégiore has left the fusion area after one year, we still stay in touch and he has been always interested in my work. Geert has been giving me suggestions in many aspects including globally the research direction to the very detailed data analysis techniques through my thesis. Even though I was not in Belgium any more for the last two yeas, we has been staying in close touch by regularly meeting together to discuss my work. In particular, Geert has helped to modify and improve my every manuscript with extreme preciseness and patience. As my thesis promoter, he also has many more promotions of the research direction to be carried out, but unfortunately many ideas have not be realised due to the limited time given for the PhD. As another director of my thesis, Prof. Stéphane Heuraux has been giving instructions in a global viewpoint. Although my stay in University of Lorraine is relatively short, I really appreciated the delight working time with him in Nancy. When most of the time we work together remotely, he always replied to my any questions by the quickest time with the most clear and detailed explains when he is very busy. In addition, since usually I was not in the University, he has helped me to handle with some complicated documents especially at the beginning when the registration documents are all written in French which I knew very little then. I also have another mentor in IRFM-CEA, Dr. Sébastien Hacquin, who has worked temporarily in Culham since my second year. Although being very busy and has one-hour time difference with me, he still deeply cares about my research work. He would like to know my progress regularly and read each of my manuscript very carefully with detailed comments.

Then, I wish to thank the colleagues who are willing to become the jury members my defense: Dr. Pascale Hennequin from École Polytechnique, Prof. Stefano Coda from EPFL, Prof. Michel Vergnat from University of Lorraine and Prof. Filip De Turck and Prof. Toon Verstraelen both from Ghent University. Thank you very much for spending the time to read my thesis and give the suggestions! Dr. Pascale Hennequin has also given me helpful instructions on my work on the development of the parametrization

method.

In IRFM-CEA, where I have spent most of my PhD time, I hope to thank all the colleagues who have participated in the operation of Tore Supra and especially the different diagnostics. Without your previous excellent work, my systematic (database) study could not be realised. The following colleagues have some specific contributions to my PhD work. I discussed with L. Vermare about spectrum fitting by the Taylor model. The analysis tool provided by D. Elbeze was helpful in validating the position of the sawteeth inversion. The discussions with P. Devynck, J. F. Artaud and C. Bourdelle help to further understand the effects of Z_{eff} on turbulence as well as the more accurate estimation of Z_{eff} by the scaling law. X. Garbet motivates the latter stage of the research work based on the collisional effects on the micro-instabilities. Many colleagues gave me a lot of help in many aspects including: C. Amador, X. Zou, F. Clairet, C. Bottereau, J. C. Giaccalone, R. Guirlet, C. Gil, Ph. Moreau and L. Lu. I would like to express special thanks to Ph. Lotte and F. Imbeaux who have given me numerous help for my stay in IRFM, especially approving me to many important conferences during my PhD time. The two secretaries in our group, N. Borio and V. Icard also helped me to handle with many document work.

When studying in Ghent University, many colleagues and students gave me different helps: Kathleen Van Oost, Frank Janssens, Eveline Indemans, Prof. Jean-Marie Noterdaeme and Prof. Christophe Leys. I also wold like to thank many other PhD students with whom I have shared many unforgettable moments during my PhD: Rennan Morales, Iaroslav Morgal, Tianbo Wang, Lei Wang, Sundaresan Sridhar, Song Xiao, Rui Mao, Zhaoxi Chen, Georgiy Zadvitskiy, Arvydas and Nicolas Ialovega.

Thanks for the funding provided by the International Doctoral College in Fusion Science and Engineering (FUSION-DC), CEA Cadarache and Ghent University!

Finally, I express my great thank to my families including my father, mother, mother-in-law, my father-in-law and my wife. Without your support I would not be able to complete this thesis. Especially, my wife has also helped to improve this manuscript.

Thank you for everyone again!

Abbreviations

BB	BroadBand
BIC	Bayesian Information Criterion
CXRS	Charge eXchange Recombination Spectroscopy
DC	Direct Current
ECE	Electron Cyclotron Emission
ECRH	Electron Cyclotron Resonance Heating
ELMs	Edge Localized Modes
EM	Electromagnetic
ETG	Electron Temperature Gradient
FFT	Fast Fourrier Transform
GENE	Gyrokinetic Electromagnetic Numerical Experiment
GG	Generalized Gaussian
HFS	High Field Side
H-mode	High-confinement mode
ICRH	Ion Cyclotron Resonance Heating
ITG	Ion Temperature Gradient
LF	Low Frequency
LFS	Low Field Side
LH	Lower Hybrid
LHCD	Lower Hybrid Current Drive
L-mode	Low-confinement mode
LOC	Linear Ohmic Confinement
LPs	Langmuir Probe
MCF	Magnetic Confinement Fusion
MHD	Magnetohydrodynamics
NBI	Neutral Beam Injection
QC	Quasi-Coherent
RF	Radio Frequency
RSS	Residual Sum of Squares
SOC	Saturated Ohmic Confinement
SNR	Signal-to-Noise Ratio
TEM	Trapped Electron Modes
TEP	Turbulence Equi-Partition

V-H mode	Very High Confinement mode
WKB	Wentzel - Kramers - Brillouin
ZFs	Zonal Flows

Symbols

$A_{\mathrm{BB}}, A_{\mathrm{LF}}, A_{\mathrm{DC}}$	Amplitude of the BB, LF and DC component
a	Plasma minor radius
$\mathbf{B}, B$	Magnetic fields
$\mathbf{B_0}$	Background magnetic fields
B_0	Magnetic fields on the axis
B_ϕ, B_θ	Toroidal and poloidal magnetic fields
B_{tot}	Total magnetic fields
$C_{\mathrm{BB}}, C_{\mathrm{LF}}, C_{\mathrm{DC}}$	The BB, LF and DC component of the frequency spectrum
c	Speed of light
D	Diffusive coefficient
D_{turb}	Turbulent diffusive coefficient
$\mathbf{E}$	Electric fields
$E_{\mathrm{BB}}, E_{\mathrm{LF}}, E_{\mathrm{DC}}$	Energy contribution of the BB, LF and DC component
E_k	Energy of turbulent flows
E_ϕ	Toroidal electric fields
F_{cost}	Cost function
f_t	Fraction of the trapped particles
I_p	Plasma current
$\mathbf{j}, j$	Plasma current density
$\mathbf{k}, k$	Wavenumber
K	Number of parameters in the parametrization model
k_{eff}	Effective wavenumber
L	Characteristic dimension of fluid system
m_e, m_i	Electron and ion mass
N	Refractive index
$\tilde{n}, \tilde{T}, \tilde{\phi}, \tilde{B}$	Fluctuation of density, temperature, electrical phase and magnetic fields
n_e	Electron density
n_t	Density of trapped particles
n_l	Central line integrated density
$\langle n_e \rangle$	Averaged electron density
p	Plasma pressure
P_{ICRH}	Power of ion cyclotron resonance heating
P_{LH}	Power of lower hybrid heating

q	Safety factor
$\mathbf{q}$	Particle heat flux
q_ψ	Edge safety factor
Q	A factor measuring the fusion reaction efficiency
q_e, q_i	Electron and ion charge
r	Radial position to the plasma center
R	Radial position to the central axis
R_e	Reynolds number
R_p	Plasma major radius
T_e, T_i	Electron and ion temperature
$\mathbf{v}$	Fluid velocity
$\boldsymbol{v}_E$	Electrostatic drift velocity of charged particles
$\boldsymbol{v}_E$	Diamagnetic drift velocity of charged particles
V	Plasma pinch velocity
V_{neo}, V_{turb}	Neoclassical and turbulent particle pinch velocity
V_p	Plasma loop voltage
W	Plasma energy
$W_{\mathrm{BB}}, W_{\mathrm{LF}}$	Width of the BB and LF component
Z	Vertical position
Z_{eff}	Effective charge number
Z_i	Ion charge number
β_{BB}	Exponent parameter of from the GG function for the BB component
$\delta n, \delta n_e$	Density fluctuation
Δ_r^{cor}	Turbulence radial correlation length
$\boldsymbol{\varepsilon}$	Dielectric tensor
η	Plasma resistivity
θ	Poloidal coordinate in tokamaks
κ	Plasma elongation
μ	Magnetic moment
$\mu_{\mathrm{BB}}, \mu_{\mathrm{LF}}, \mu_{\mathrm{DC}}$	Central position of the BB, LF and DC component
ν	Fluid viscosity
$\nu_{ee}, \nu_{ii}, \nu_{ei}$	Electron-electron, ion-ion and electron-ion collision frequency
ν_{eff}	Effective collisionality
ρ	Normalized radial position
ρ_e, ρ_i	Larmor cyclotron radius of electron and ion

$\boldsymbol{\sigma}$	Plasma conductivity
$\sigma_{\mathrm{DC}}, \sigma_{\mathrm{LF}}, \sigma_{\mathrm{BB}}$	Standard deviation of the DC, LF and BB component
$\tau(f)$	Time Delay
τ_{coll}	Characteristic collisional time for the trapped particles
τ_{detrap}	Detrapping time of the trapped particles by collisions
Γ	Particle transport flux
$\Gamma_{neo}, \Gamma_{turb}$	Neoclassical and turbulent particle transport flux
τ_E	Energy confinement time
$\upsilon_{\parallel}, \upsilon_{\perp}$	Particle velocity parallel and perpendicular to the magnetic fields
ϕ	Toroidal coordinate in tokamaks
	Phase difference
χ	Heat transport coefficient
$\chi_e^{exp}, \chi_i^{exp}$	Experimental electron and ion heat transport coefficient
χ_e^{NC}, χ_i^{NC}	Neoclassical electron and ion heat transport coefficient
χ_e^{C}, χ_i^{C}	Coulomb collisional coefficient of electron and ion
ω	Frequency of waves
ω_b	The bounce frequency of the trapped particles
ω_{ce}, ω_{ci}	Electron and ion cyclotron frequency
ω_{pe}	Electron plasma frequency

Contents

For my dear wife F. J.

Chapter 1

Introduction

Contents

The physics of plasma turbulence is among the most important problems in fusion research and has been extensively studied experimentally and theoretically. However, a global physical picture is still lacking. The contribution of this thesis is to explore trends of turbulence properties over a broad range of plasma conditions. This is different from the previous work, which is conventionally based on a limited number of dedicated experiments under specific plasma conditions. With the increasing size of databases over the past few decades, techniques have been developed to detect patterns in large data sets. It is this type of approach that we have intended to transfer to the investigation of turbulence in fusion plasmas, based on diagnostic measurements that are sensitive to turbulent fluctuations.

In particular, in this thesis a parametrization method is developed for frequency spectra obtained from reflectometry, for a systematic turbulence study in tokamak plasmas. The method is applied to a large database from the Tore Supra tokamak, in order to extract patterns (trends, clusters) reflecting interesting underlying physics across a wide range of plasma conditions. The statistical approach is able to provide useful information which is difficult to obtain through the traditional shot-to-shot analysis.

This chapter provides an introduction to the topics that the present thesis is concerned with. Section 1.1 touches upon the background of the worldwide energy problem and discusses a number of alternative solutions for sustainable energy generation. Fusion turns out to be one possible solution, where one promising experimental configuration is the tokamak device, which is discussed in section 1.2. One of the main obstacles on the route to fusion energy is the problem of turbulent energy transport. Solving this problem requires a better understanding and control of the micro-instabilities responsible for the turbulent activity. This serves as the basic motivation of this thesis, as presented in section 1.3.

1.1 Energy issues and solutions

The energy problem is related to a scarceness of resources as well as environmental problems, affecting countries all over the world. These issues will become even more severe in the future considering the continuous increase and development of world population. Several alternative energy sources are being developed, which are sustainable and environmentally friendly. Fusion energy is one of them, with magnetic confinement fusion currently the main research avenue.

1.1.1 Demand for new energy sources

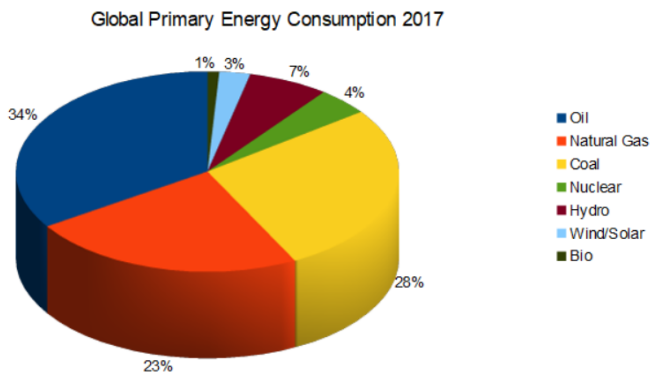

Figure 1.1: World energy consumption in 2017 [BP 2017].

Fossil fuels (coal, oil and natural gas) have greatly influenced our lives for a long time and still play a dominant role in the current world energy consumption, as shown in figure 1.1. However, fossil fuels not only have a harmful effect on the environment, e.g., air pollution and the global warming by greenhouse gases, but also face the problem of exhaustion [Abas 2015]. It has been estimated that coal, oil and natural gas resources will be depleted within about 110, 50 and 50 years, respectively [Shafiee 2009]. As a result, increasing efforts are devoted to development and implementation of renewable energy [Akella 2009], which are economic viable. However, the main renewable energy sources, including hydro-energy, solar, wind, geothermal and biomass [Fridleifsson 2001,

Momirlan 2005, Jacobson 2011], are limited by the local natural conditions and, as a result, their applicability depends on one region to another[Panwar 2011]. Other problems are related to storage (due to intermittency) and transport of energy [Agbossou 2004, Kaldellis 2007, Rentizelas 2009].

On the other hand, nuclear energy based on the mass-energy equation $E = mc^2$ is an alternative option and there are basically two approaches: fission and fusion, as shown in figure 1.2. While fission involves the splitting of heavy atomic nuclei, fusion of light nuclei also releases energy, as shown in figure 1.2. Fission energy has been used in the industrial electricity generation for many years, and it does not generate greenhouse gases. However, the radioactive nuclear waste and risk of nuclear accidents, such as the Fukushima event [Bolsunovsky 2011], are reducing its acceptability. In addition, considering the limited reserves of uranium, fission has been estimated to be usable for limited time before exhaustion [Dittmar 2013].

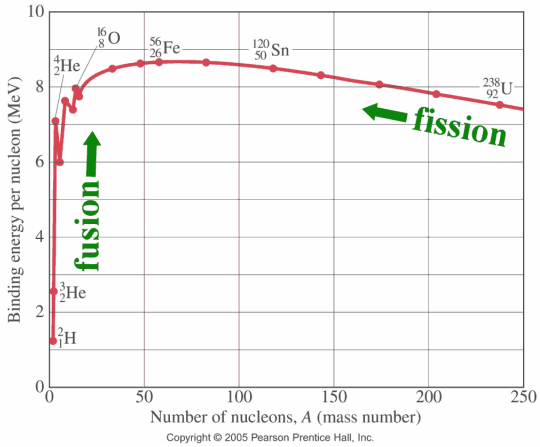

Figure 1.2: Binding energy per nucleon evolves with the atomic mass number.

In contrast, fusion energy is clean, with low radioactivity [Khvesyuk 2002] and also without emission of greenhouse gases. The basic fuel reserves are as good as endless: deuterium and tritium come from the ocean and the self-breeding from $_3Li^6$ (abundant in the earth's crust), respectively. The mere resources on the earth can already support the energy consumptions of humans for at least thousands of years [Ongena 2012].

1.1.2 Principles of fusion

Although any combination of light nuclei could lead to the realization of fusion reactions, the most effective ones with the largest cross-sections are [Freidberg 2007]:

$$\mathrm{D} + \mathrm{T} \rightarrow \alpha + \mathrm{n} + 17.6\ \mathrm{MeV}, \tag{1.1}$$

$$\mathrm{D} + \mathrm{D} \rightarrow (50\%)\ \mathrm{He}^3 + \mathrm{n} + 3.27\ \mathrm{MeV}, \tag{1.2}$$

$$\mathrm{D} + \mathrm{D} \rightarrow (50\%)\ \mathrm{T} + \mathrm{p} + 4.03\ \mathrm{MeV}, \tag{1.3}$$

$$\mathrm{D} + \mathrm{He}^3 \rightarrow \alpha + \mathrm{p} + 18.3\ \mathrm{MeV}. \tag{1.4}$$

Here, D is deuterium (^{2}H), T is tritium (^{3}H), ^{3}He is helium-3, α is the helium nucleus (alpha particle, $^4_2\mathrm{He}^{2+}$), n is neutron, p is proton.

In fusion reactions, the reaction rate is proportional to the cross-section for the different reactions. The cross-section is strongly affected by the reaction temperature, as shown in figure 1.3. In order to obtain a large cross-section, thus an effective reactivity, the temperature should be at least tens of keV, corresponding to $\sim$ 100 millions °C. At such high temperatures, the kinetic energy per particle becomes much larger than its ionization energy (order of eV), so the reaction fuel constituents no longer form neutral atoms but exist in the plasma state.

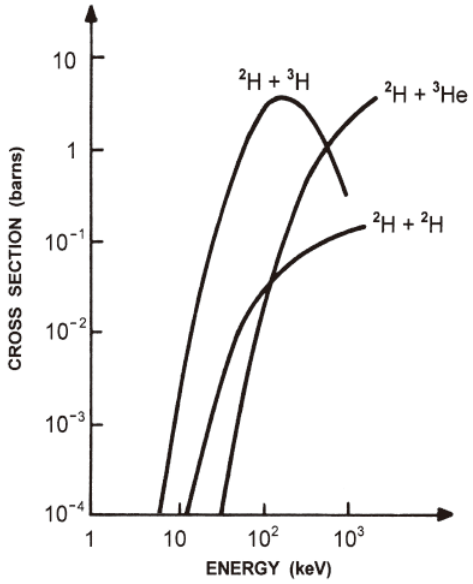

Figure 1.3: Cross -section of some basic fusion reactions as a function of the particle energy. Reprinted from [Bittencourt 2004].

However, the difficulty is not the fusion reaction itself, which has already been achieved by the explosion of hydrogen bombs, but an effective control of the reaction process to obtain a stable and continuous output of energy. Therefore the confinement of the reaction fuel is of fundamental importance. Studies have shown that, in order to realize a controlled self-sustaining reaction (burning) of the fuel, the product of the fuel density (n) and the energy confinement time (τ_E) must satisfy the so-called ignition condition [Wesson 1997]:

$$n\tau_E > 1.5 \times 10^{20}\ m^{-3}s, \tag{1.5}$$

given that the optimal temperature is realized. On the other hand, in terms of the power balance, the loss power is balanced by the externally supplied power plus the $\alpha-$particle power: $P_L = P_H + P_\alpha$. The power amplification factor Q is a measure of reactor performance:

$$Q = \frac{P_\alpha}{P_H}. \tag{1.6}$$

Here, $Q = 1$ means that 20% of the applied heating power comes from the $\alpha-$particles.

At ignition, P_H should be zero and $Q \to \infty$, thus all the loss power is compensated by the $\alpha-$particle power.

There are mainly two distinct methods to approach a self-burning fusion reaction: magnetic confinement fusion (MCF) [Artsimovich 1972] and inertial confinement fusion (ICF) [Miller 2004, Craxton 2015]. MCF aims at increasing the confinement time of low-density plasmas using magnetic fields, whereas in ICF the fuel is heated and compressed using a high-power short laser pulse. ICF has been studied for instance at the National Ignition Facility (NIF) [Moses 2016], but the ignition condition has not been reached due to various unresolved problems, such as controlling the symmetry of the imploding fuel [Michel 2009], Rayleigh-Taylor instabilities [Nagel 2017], shockwave convergence [Ma 2016], etc. In addition, the Q value obtained in ICF has not met expectations so far [Ross 2015, Le Pape 2018]. On the other hand, in MCF there has been significant progress towards the ignition condition and the Q value has been steadily raised. Confinement times of the order of seconds and $Q > 1$ have been obtained[Romanelli 2015]. This thesis is situated in the area of MCF, which is the more promising fusion scheme for the near future.

1.2 Tokamaks

In the study of MCF, many different devices with different magnetic geometries have been invented since 50's. Among the other devices such as magnetic mirrors, stellarators, and reversed-field pinches, the tokamak has shown the most promising performance towards realising net fusion power generation. This section covers only some general concepts of tokamaks.

1.2.1 Motions of charged particles in magnetic fields

As mentioned before, the fusion reaction fuels are ionized to form the state of plasma at high temperature. At that point, the motion of the charges plasma particles, i.e. electrons and ions, is no longer predominately determined by short-range Coulomb collisions between the particles, but by long-range electromagnetic forces. This has inspired scientists to utilize external magnetic fields to confine the fuel (i.e., the plasmas).

Therefore, in order to understand the confinement performance of tokamaks, the first ingredient is the motion of charged particles in external magnetic fields.

The theory of magnetohydrodynamics (MHD) [Goldston 1995, Freidberg 2007] and kinetic theory [Stix 1992, Bittencourt 2004] have been developed to describe the complex plasma behavior in the presence of external magnetic fields. In the MHD model, a plasma is regarded as a fluid in the presence of electromagnetic fields. Kinetic theory is based on the distribution function in six-dimensional phase space to completely describe the plasma motion from a statistical point-of-view.

Here, for simplicity, a single particle in a uniform magnetic field is considered, to capture the most important features of the motion. Figure 1.4 shows the helical motion of a positively charged particle in an external uniform magnetic field ($\mathbf{B}$). In the direction

parallel to **B**, the parallel velocity of the particle ($\boldsymbol{v}_{\parallel}$) is constant. In the direction perpendicular, the particle undergoes a gyro-motion with velocity ($|\boldsymbol{v}_{\perp}|$). The cyclotron frequency (ω_c) of the perpendicular motion is

$$\omega_{cs} = \frac{q_s B}{m_s}, \tag{1.7}$$

where q_s and m_s are the charge and mass of the particle, and B is the magnitude of the magnetic fields. The gyro-radius (Larmor radius) is

$$\rho_s = \frac{m_s v_{\perp}}{q_s B}, \tag{1.8}$$

where $v_{\perp}$ is the magnitude of the velocity perpendicular to **B**, with $s = e, i$ for electron and ion. As a result, the composite motion of the particle is a helical motion around **B**.

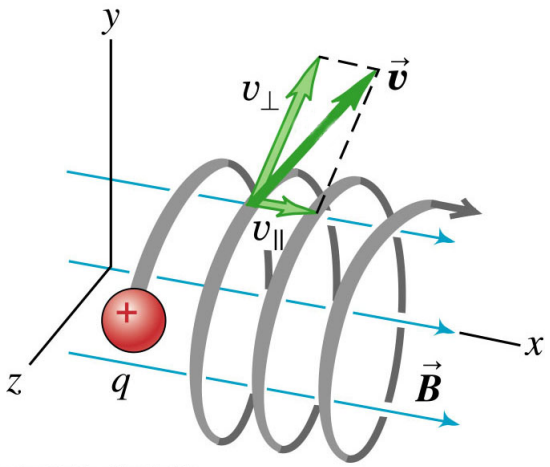

Figure 1.4: Illustration of the gyro-motion of the charged particles in a uniform magnetic field. Copyright@ 2004 Pearson Education, Inc., publishing as Addison Wesley.

1.2.2 Magnetic configurations

Since the charged particles tend to gyrate around the magnetic lines of force, they are limited in their motion across the magnetic field. Hence, the simplest idea to confine a plasma is to use a linear device in cylindrical shape with strong magnetic fields generated by the external coils to confine the particles. However, there would still be particles losses at both ends of such a device, even when the magnetic fields around the open ends have been further strengthened to help confine the particles, like in magnetic mirrors.

The solution is to connect the ends of the device by bending the linear (cylindrical) configuration into a torus. The transformation of the device shape avoids particle losses at the two ends, thus greatly enhancing the confinement performance. However, several other forms of particle losses exist, i.e. particle drifts due to the toroidal geometry of the device. Therefore, to further compensate the particle drifts, the magnetic fields

have to be twisted to become helical field lines. Moreover, further studies have shown that the twisted magnetic fields could effectively reduce several instabilities, thus further improving the confinement.

There are two methods to generate helical magnetic fields. One straightforward way is to construct helical magnetic coils, and the corresponding apparatus is called *stellarator*. However, the construction of such magnetic coils needs extremely high accuracy and it is very complicated to guarantee the precise magnetic fields [Motojima 2000]. The tokamak is the other concept to realize the required magnetic configuration through large plasma currents, as shown in figure 1.5. First, in figure 1.5 (a), the toroidal magnetic field (B_ϕ) is generated by external magnetic coils. Then, in figure 1.5 (b), the poloidal magnetic fields (B_θ) are induced by large toroidal plasma currents (I_p). The resulting total helical magnetic field B_{tot}, the composition of B_ϕ and B_θ, is shown in figure 1.5 (c). Note that in tokamaks, I_p is usually very large (in the order of MA). Nevertheless, the self-generated B_θ ($\sim$ tens of Gauss) is much smaller than B_ϕ (a few Tesla). Accordingly, the charged particles in tokamaks move along the magnetic field lines around the torus and thus are confined, to a large extent, in the device.

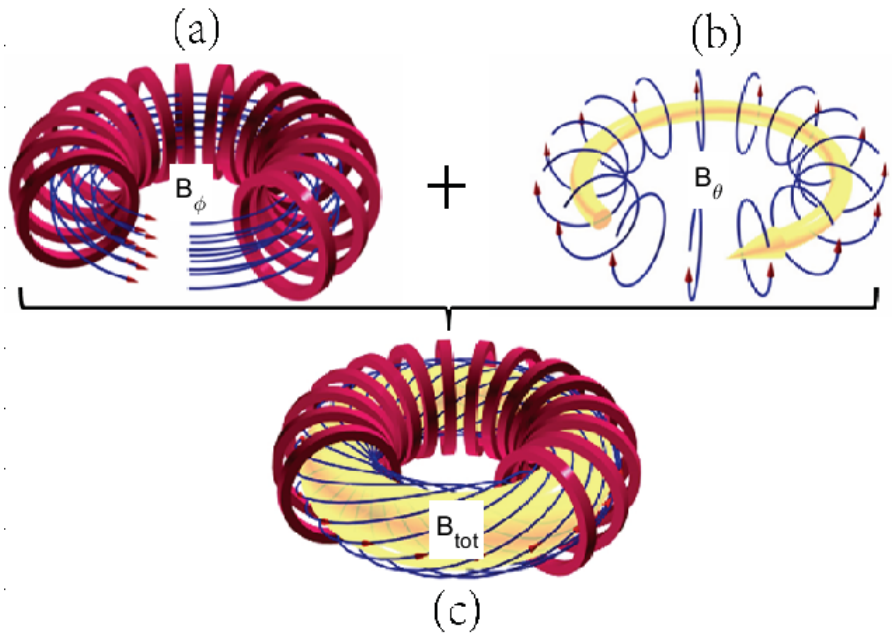

Figure 1.5: Composition of the total helical magnetic fields B_{tot} (c) in tokamaks from (a) toroidal B_ϕ and (b) poloidal B_θ magnetic fields.

From the analysis above, the magnetic configuration of a tokamak is crucial to its confinement performance. Therefore, it is important to further understand the complicated magnetic fields generated by the varying B_ϕ and B_θ with respect to spatial coordinates. Before that, some definitions of the spatial geometry are necessary, as shown in figure 1.6. A simple circular plasma cross-section has been considered here to illustrate the spatial coordinates and parameters. The directions of ϕ, θ, R indicate the toroidal, poloidal and radial coordinate, respectively. The plasma major radius (R_p) is defined as the distance

between the plasma center (O) and the central axis (L_0). The plasma minor radius (a) is just the distance between the plasma edge and the center. According to the relative ratio between R_p and a, the tokamaks can be further categorized into the conventional tokamaks ($R_p \gg a$) and the spherical tokamaks ($R_p \sim a$). Most of the tokamak fusion studies have been focused on the conventional tokamaks, while the study on the spherical tokamaks has been advocated in recent years due to their compactness and thus lower cost, although normally higher magnetic fields are required. In the plane of the poloidal cross-section (ϕ = constant), the plasma position can be described by two different coordinate systems: cylindrical coordinates (R, Z) $(0 \leq R < +\infty, -\infty < Z < +\infty)$ and polar coordinates (r, θ) $(0 \leq r < +\infty, 0 \leq \theta < 2\pi)$. These provide the absolute spatial position and the relative position w.r.t. the plasma center, respectively. For many studies focusing on the poloidal cross-section and assuming toroidal symmetry, the relative positions (r, θ) are more convenient to describe the plasma position. Specifically, for the study only on the mid-plane ($Z = 0$), the one-dimensional normalized radial position can be expressed as $\rho = rcos(\theta)/a$. Then, since the magnetic field decreases from the central axis (L_0) towards the outer boundary ($B_\phi \propto 1/R$), $\rho < 0$ and $\rho > 0$ are referred as the high-field side (HFS) and the low-field side (LFS), respectively.

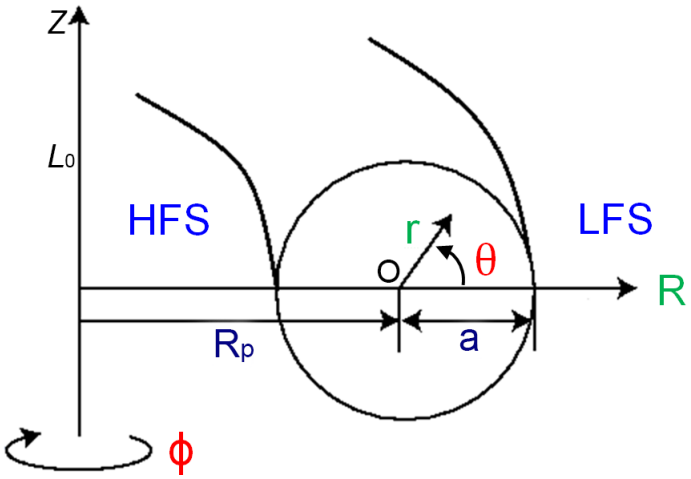

Figure 1.6: Illustration of a simple circular cross-section of tokamaks to define the basic parameters in tokamak configurations.

We continue our understanding of the tokamak magnetic configuration through the safety factor q. From figure 1.5 (c), the magnetic field lines (or the charged particles) follow a helical trajectory when travelling around the torus. When the field lines (or particles) return to their initial positions after m laps in the toroidal direction and n laps in the poloidal direction, the *safety factor* is defined as: $q = m/n$. The safety factor is a measurement of twist or helicity of the magnetic fields, i.e. weaker twist leads to larger q. In general, higher q leads to better stability of operation, explaining the origin of the term 'safety factor'. However, the optimal operation scenarios usually have moderate values of q, since some mechanisms of confinement and instabilities must be balanced. In normal equilibrium states, q increases monotonously from the plasma center towards the plasma edge and is symmetrical with respect to the plasma center. Then, the radial

profile of q can be approximated by

$$q(r) = \frac{2\pi r^2 B_\phi}{\mu_0 I(r) R}, \tag{1.9}$$

where μ_0 is the vacuum permeability. In the q profile, the radial positions with rational numbers in the safety factor ($q = 1/1, 2/1, 3/2, 4/3, ...$) are important, since MHD instabilities such as magnetic islands and tearing modes can form at these locations under certain conditions. Specifically, the $q = 1$ position (surface) is related to the sawtooth instabilities [Chapman 2011], which is a quasi-periodic crash and subsequent relaxation of the core plasma temperature affecting the plasma confinement. However, sometimes accurate measurement of the complete q profile is not available and only the edge safety factor ($q_\psi = q(a)$) is measured. The edge safety factor q_ψ is one of the most important dimensionless parameters determining confinement performance.

1.2.3 Trapped and passing particles

Now we further discuss the motion of charged particles in the tokamak magnetic field. The magnetic moment of a particle is defined as the ratio between its perpendicular kinetic energy and the magnetic field: $\mu = \frac{1}{2}mv_\perp^2/B$, where $v_\perp$ is the perpendicular ($\perp$ **B**) velocity of the particle. Since the magnetic moment μ is an adiabatic invariant in slowly varying magnetic fields, higher B leads to larger perpendicular velocity $v_\perp$. Furthermore, because of energy conservation $\frac{1}{2}mv^2 = \frac{1}{2}mv_\perp^2 + \frac{1}{2}mv_\parallel^2$ ($v_\parallel$ the parallel velocity $\parallel$ **B**), particles with small $v_\parallel$ can be reflected back when $v_\parallel = 0$ in an area of high magnetic field strength, as shown in figure 1.7 (a). As a result, in the poloidal cross-section, some particles undergo a reflection back and forth, forming a banana-shaped trajectory (projected in the cross-section). In other words, these particles are trapped at the LFS by the mechanism of magnetic mirrors and are called *trapped particles* (or banana particles). The bounce (reflection) frequency of the trapped particles is:

$$\omega_b = \frac{v_\perp}{qR_p}\left(\frac{r}{2R_p}\right)^{1/2}. \tag{1.10}$$

When the parallel velocity $v_\parallel$ of the particles is sufficiently large, the particles are no longer trapped but take a round path in the poloidal cross-section, and these particles are called *passing particles*, as shown in figure 1.7 (b). The fraction of trapped particles can be calculated as: $f_t = (\frac{2r}{R_p+r})^{1/2}$. In conventional tokamaks, the fraction of trapped particles can become relatively high.

The previous discussion has not considered any collisional effects. Collisions can prevent particle trapping by changing the particle velocities. The detrapping time is: $\tau_{detrap} \simeq \frac{2r}{R_p}\tau_{coll}$, where τ_{coll} is the characteristic collision time for the particles. Then, the collisionality condition for particle detrapping is that the detrapping time should be shorter than the bounce time of the trapped particles: $\tau_{detrap} < \omega_b^{-1}$ [Wesson 1997].

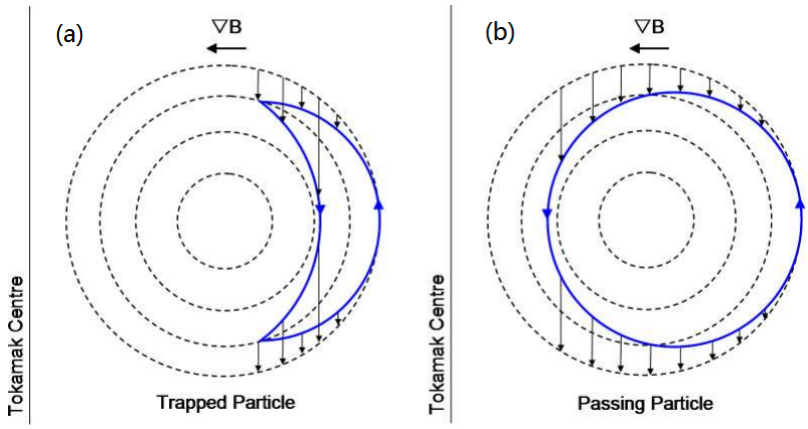

Figure 1.7: (a) Trapped and (b) passing particles in the view of the poloidal cross-section of tokamaks.

1.2.4 Heating scenarios

As discussed in section 1.1.2, in self-burning fusion plasmas, the radiation power losses are balanced by the heating from the slowing down of the α particles. However, external heating is required in two situations:

- At the initial stage to ignite the reaction.
- In experimental plasma studies when the number of fusion reactions is negligible or the power output from the α particles is not enough to compensate the losses.

In tokamaks, the fundamental heating method is Ohmic heating by the large toroidal plasma current through the Joule effect. The Ohmic heating power density is $p_{\mathrm{Ohmic}} = \eta j^2$, where η and j are the plasma resistivity and the current density, respectively. Although the intrinsic Ohmic heating is strong at low temperatures, it becomes less efficient at high temperatures, since η decreases rapidly with temperature ($\eta \propto T_e^{-3/2}$). Therefore, auxiliary heating methods are required.

There have been mainly two auxiliary heating methods: the injection of energetic neutral beams and the resonant energy absorption of electromagnetic fields in the radio-frequency (RF) domain. Both methods can provide power levels of the order of MW. Neutral beam injection (NBI) heats both electrons and ions through Coulomb collisions between the neutral particles and the charged plasma particles. The RF heating can be further categorized into three types according to their frequencies:

- Ion cyclotron resonance heating (ICRH) transfers the energy of the electromagnetic waves to ions at the resonance condition $\omega = \omega_{ci}$ (in tens of MHz).
- Electron cyclotron resonance heating (ECRH) directly heats the electrons through microwaves in the frequency range of hundred of GHz.
- Lower-hybrid (LH) heating uses electromagnetic waves in the frequency range 1-8 GHz, which is between the ion and electron cyclotron frequency: $\omega_{ci} < \omega <$

ω_{ce}. LH heating is particularly useful for current drive because of its effect on current profiles. LH heating is also the conventional heating method in long-pulse operations.

The development of heating scenarios contributes to accomplishing the goals of tokamak experiments in several ways. Most importantly, auxiliary heating allows reaching the power threshold to trigger the transition from the low-confinement regime (L-mode) to high-confinement regime (H-mode). However, in auxiliary heated plasmas, the dynamics of the charged particles becomes even more complicated because, energetic particles form after gaining kinetic energy from the injected electromagnetic waves or beams. The energetic particles can further drive various instabilities. Specifically, ECRH and LH heating could generate fast electrons, which can further drive the electron fishbone instabilities. ICRH and NBI give rise to different types of instabilities such as the energetic-ion-driven Alfvén waves.

1.2.5 Basic diagnostics

In tokamaks, various diagnostics have been developed to measure the basic plasma parameters [Hutchinson 2002, Wesson 1997]. First of all, magnetic loops or coils provide the most fundamental plasma properties such as the plasma current (I_p), loop voltage (V_p), plasma position and shape (elongation, triangularity), plasma energy (W), etc. Specifically, the energy confinement time can be obtained by the ratio between the plasma energy and the input heating power: $\tau_E = W/P_{\text{input}}$.

The basic plasma parameters include the electron density (n_e) and the electron temperature (T_e). Interferometry has been a standard tool to measure the line integral of the electron density by the phase difference between the measuring beam and the reference beam. Multiple channels (arrays) of interferometry measurements combined with an inversion technique can provide the local n_e profile in a poloidal cross-section, with a spatial resolution depending on the number and coverage of the set of chords. A reflectometry diagnostic measures the reflected part of an emitted wave to provide the local n_e with a much higher spatial resolution, as discussed in more detail in chapter 3. Two different methods have been developed to measure the electron temperature in tokamaks: Thomson scattering and electron cyclotron emission (ECE). Thomson scattering directly measures the plasma pressure (n_e, T_e) by actively launching laser beams into the plasma and spectrum broadening of the scattered beams provides T_e, whereas ECE determines T_e by passively measuring the intensity of harmonic frequencies of electron cyclotron emission ($\omega = n\omega_{ce}$, n the harmonic number, ω_{ce} the electron cyclotron frequency). Although both methods can provide the radial profile of T_e, Thomson scattering can also provide the accurate edge values where the plasma optical depth is not sufficient to obtain an accurate T_e estimation by ECE. On the other hand, ECE has a much higher temporal resolution with lower noise, which can be used to study the fast physical process such as the sawtooth instability. Although Langmuir probes can usually provide accurate measurements of n_e and T_e, their application is constrained to the edge region where the temperature does not exceed the capability of the probes.

Information about the ion properties, including the ion temperature (T_i) and the effective charge number (Z_{eff}) is also important. T_i is generally estimated from the Doppler broadening of line radiation from charge exchange recombination spectroscopy (CXRS). Z_{eff} is a measure of the degree of impurity, defined as $Z_{\text{eff}} = \sum n_i Z_i^2 / n_e$, where Z_i is the charge number of each ion species. In a fully ionized pure hydrogen isotope plasma, $Z_{\text{eff}} = 1$, and normally $Z_{\text{eff}} > 1$. Measurement of bremsstrahlung radiation is typically used to estimate Z_{eff}.

1.2.6 Tore Supra

Since this thesis is totally based on the database of the Tore Supra tokamak, which was located in the Institute for Magnetic Fusion Research (IRFM) at CEA Cadarache in Southern France, the basic parameters, heating methods and diagnostics of Tore Supra are briefly introduced.

Tore Supra (from "torus" and "superconductor") operated from 1988 to 2011 and has in the meantime been upgraded to the WEST machine (Tungsten Environment in Steady-state Tokamak), since 2016. Tore Supra had a circular cross-section with actively cooled plasma-facing components and a set of pump limiters. Equipped with superconducting toroidal magnets, it was initially developed to investigate technical and physical issues in long-pulse steady-state plasmas. Tore Supra once held the world record for the longest tokamak pulse (6 mins 30 secs) in 2003. Table 1.1 lists some typical values of basic operational parameters of Tore Supra. Tore Supra was a conventional tokamak ($R_p \gg a$) operating at high magnetic fields (> 3 T) with relatively long plasma pulses (> 10 s).

On-axis toroidal magnetic field B_0	3.4/3.8 T
Plasma current I_p	1 MA
Major radius R_p	2.38 m
Minor radius a	0.72 m
Plasma elongation κ	1.0
Line-averaged electron density $\langle n_e \rangle$	2×10^{-19} m^{-3}
Central line-integrated density n_l	4×10^{-19} m^{-2}
Plasma volume	25 m^3
Pulse duration	20 s

Table 1.1: Typical operational parameters of the Tore Supra tokamak.

Tore Supra was equipped with lower hybrid current drive (LHCD), ICRH and ECRH systems, the locations of which are shown in figure 1.8. The 3.7 GHz LHCD system was designed to inject 8 MW of additional power in long-pulse operations [Bibet 2001]. Note that LHCD can generate suprathermal electrons, which could increase the parasitic noise of some diagnostic measurements. ICRH is another main auxiliary heating system on Tore Supra and its operational frequencies are between 35 MHz to 80 MHz. Three

ICRH antennas were installed in port Q1, Q2 and Q5, respectively (figure 1.8), and the antenna positions were kept almost constant. Each antenna can inject up to 4 MW power [Colas 2006]. ECRH heats the electrons by microwaves at the frequency of 118 GHz, generated by 2 gyrotrons of 400 kW [Lennholm 2003]. However, due to technical problems, the number of ECRH plasmas is relatively limited in the Tore Supra database.

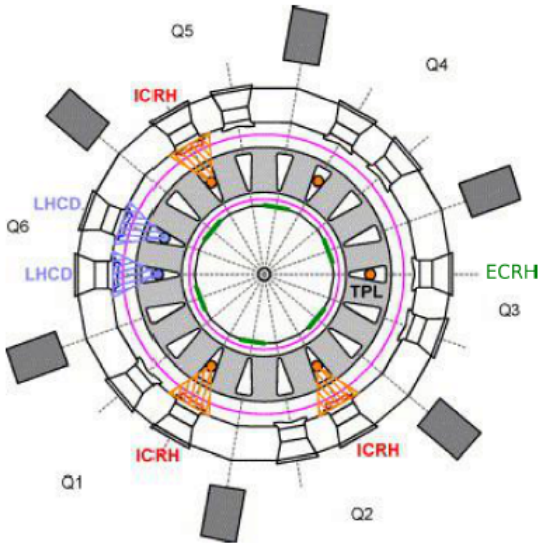

Figure 1.8: The locations of the LHCD, ICRH and ECRH systems installed at Tore Supra from the top view.

The details of the Tore Supra diagnostics can be found in [Gil 2009]. For the basic parameters, a 10-channel far-infrared interferometry system was installed to measure the radial profile of n_e with 1 ms time resolution. However, measurements of edge density have larger uncertainties due to the lack of spatial points in the strong ∇n region. A 32-channel ECE system [Ségui 2005] was installed to measure the radial profile of T_e with both slow (1 ms) and fast (1 μs) acquisition and spatial resolution of $2 - 3$ cm. T_i was measured from CXRS but only in a very limited number of discharges. Z_{eff} was measured by bremsstrahlung in both vertical and tangential directions. More dedicated diagnostics have been designed for various specific physics studies such as turbulence research. Three reflectometry systems, viz. the D-band core fixed-frequency reflectometer [Sabot 2006b], the V- and W-band edge fast-sweeping reflectometer [Clairet 2010] and the Doppler reflectometer [Hennequin 2006] (discussed in more detail in chapter 3) enable a comprehensive study of density turbulence from the edge to the core region.

1.3 Motivation of this thesis

The motivation of this thesis is related to both the issue of plasma turbulence and the methodology for extracting information about the turbulence. The unsolved problems of turbulent fluctuations and their link with micro-instabilities and transport have es-

sentially driven the turbulence study for this thesis (as well as many other theses). The specificity of this thesis lies in the fact that it is the first attempt of a database approach in the context of fusion turbulence studies. A systematic study is possible thanks to the large amount of accumulated experimental data over many years of operation of Tore Supra. In addition, a dedicated methodology was developed to enable such a study, using methods from the field of probability and statistics.

1.3.1 Gradient-driven turbulence

In tokamak fusion plasmas, the electron density n_e and temperature T_e are very high in the core region. The typical n_e and T_e are $1 \times 10^{20}\ m^{-3}$ and $10\ keV$, respectively. However, in the edge plasma near the wall, n_e and T_e decrease to the order of $10^{17}\ m^{-3}$ and $10\ eV$, respectively, to avoid excessive heat and particle loads on the wall. Figure 1.9 illustrates the large disparity of n_e and T_e in the central and edge regions, as well as the typical electron density profile $n_e(r)$ and temperature profile $T_e(r)$. A region with strong gradient of n_e, T_e, and thus pressure gradient ($p = nKT$, K the Boltzmann constant), exists between the central and edge regions. This strong gradient provides the free energy to create micro-instabilities which can develop into the saturation state called *turbulence*. Furthermore, particles and energy can transfer across the turbulent vortices rapidly. Consequently, the cross-field transport increases and the confinement degrades.

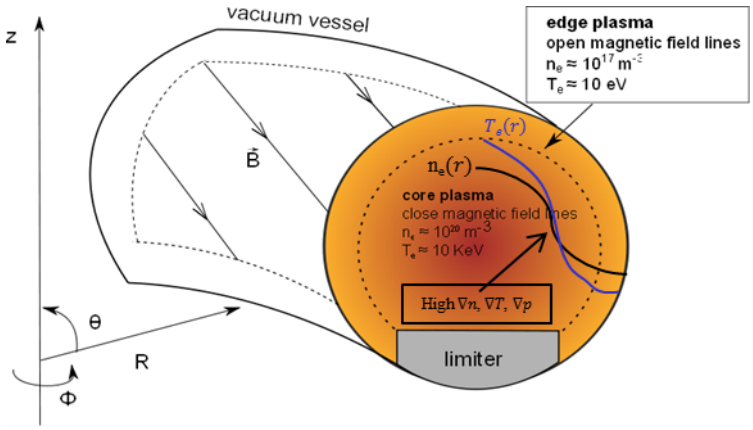

Figure 1.9: Strong n_e and T_e gradient between the central and edge region of tokamaks.

Experimentally, many diagnostics and analysis methods have been developed to measure the fluctuations of density ($\tilde{n}$), temperature ($\tilde{T}$), electric potential ($\tilde{\phi}$) and magnetic field ($\tilde{\mathbf{B}}$) originating from plasma turbulence. The relations between turbulence and transport are also unclear so far. Since turbulence has deleterious effects on the confinement, it is very important to understand the underlying physics of the instabilities, turbulence, and turbulent transport.

1.3.2 Towards a systematic study

The fixed-frequency reflectometry on Tore Supra has been dedicated to detect local turbulence properties in the core region. After years of measurements, a large reflectometry database covering a wide range of plasma conditions has been obtained. This drives this thesis to carry out a database study of plasma turbulence by systematic analysis of the frequency spectra obtained from the reflectometry measurements in order to find more general trends or patterns.

This systematic study originates from the extensive application of data science, involving methods from probability theory, statistics, machine learning, etc., throughout science and engineering. In fusion research,the global energy confinement time [Greenwald 1984] or the power threshold for the transition from low to high confinement [Martin 2008] are two well-known examples of database analysis. Trends are often described in terms of other quantities through semi-empirical scaling laws [Yushmanov 1990a, Verdoolaege 2015]. The parameters of these scaling laws, estimated using statistical regression methods, are instructive to the underlying turbulent transport properties and micro-instabilities. A database approach with statistical tools can be very useful for making an inventory of the characteristics of some aspects of the plasma, allowing investigations of systematic trends that could remain hidden in smaller-scale studies. Although physical explanation of observed trends is not always straightforward, knowledge of trends can drive the development of physical models, contribute to their verification and enable predictions.

A database approach is complementary to the more traditional shot-to-shot analysis, the latter involving a more strictly controlled range of plasma conditions and accurate measurements. The shot-to-shot analysis is usually supported by simulations to interpret the experimental observations, which in turn help to validate the simulation models and tools for dedicated discharges [White 2008, Sung 2016, Holland 2016, Creely 2017]. However, undertaking systematic simulations for even a part of a database may be hampered by prohibitive computing time and human resources. On the other hand, trends identified through a database analysis can lead to new experimental proposals and shot-to-shot analysis to explain or confirm the trends. For instance, in the dimensionless energy confinement time scaling law [Petty 1995], the dependence of confinement on the normalized Larmor radius can give clues on the Bohm or gyro-Bohm scaling of the turbulent eddies. This dependence has also been investigated through dedicated Larmor scaling experiments [Christiansen 1993, Vlad 2005].

Furthermore, in the majority of studies of trends in fusion science, the response variable is usually a single scalar quantity, such as the energy confinement time or power threshold for the transition from low to high confinement. However, this study aims at characterizing frequency spectra by multiple quantities, such as the spectrum shape, width, components, etc. In order to make the problem manageable, each spectrum has to be described using a sufficiently succinct model, that captures the essential characteristics of the spectrum. Since the frequency spectrum obtained by the Fourier transform algorithm requires several hundreds to a thousand frequency bins for a good spectral resolution, some kind of dimensionality reduction is needed, in order to decrease the number

of parameters used to describe each spectrum. The earlier work regarding frequency spectrum decomposition [Vershkov 2005, Vershkov 2011, Krämer-Flecken 2004, Krämer-Flecken 2015], as shown in figure 1.10, inspires us to further parameterize the spectra by a few parameters. With the few identified turbulence parameters, we will be able to investigate globally the turbulence properties in different plasmas heating scenarios and extract the general trends. The realization process of this database turbulence analysis is shown in figure 1.11, which contains the main work of this thesis.

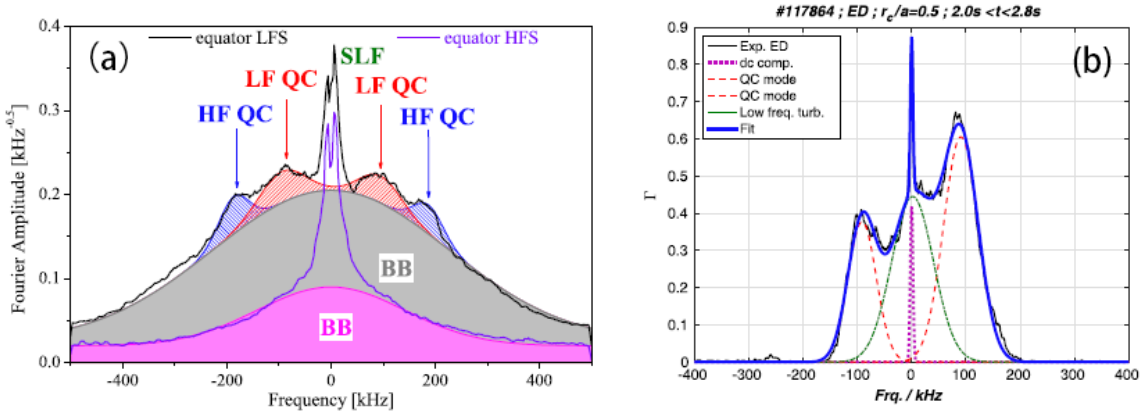

Figure 1.10: Spectrum decomposition by (a) the power spectrum from [Vershkov 2005] and (b) the coherence spectrum from [Krämer-Flecken 2015].

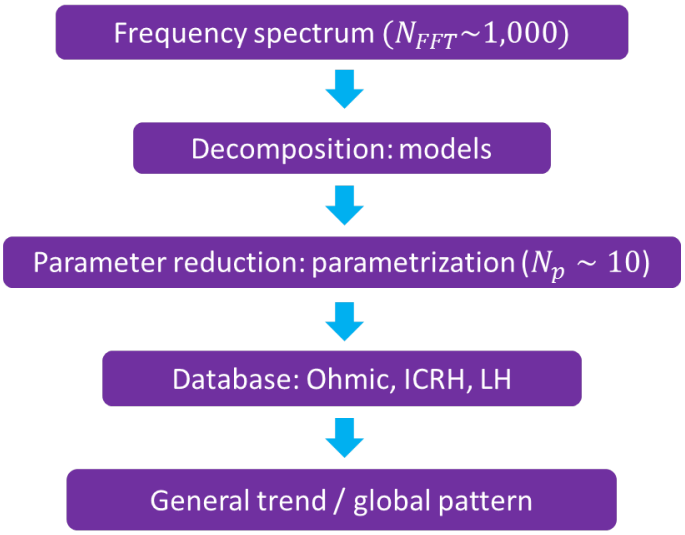

Figure 1.11: The process of a systematic turbulence study from frequency spectra of density fluctuation measurements by fixed-frequency reflectometry.

1.3.3 Outline of this thesis

As this study has been focused on a systematic study of frequency spectra from reflectometry fluctuation measurements, chapters 2 and 3 are dedicated to a detailed discussion on turbulence and reflectometry before carrying on with the actual thesis work:

- **Chapter 2** starts from the general properties of turbulent phenomena before focusing on the turbulent transport in magnetic confinement devices. We then introduce the origin of turbulence in tokamak fusion plasmas from micro-instabilities, focusing on TEM and ITG instabilities and the effects of collisionality. Finally, some properties of the density fluctuations are presented.

- **Chapter 3** first derives the dispersion relation from the classical theory of electromagnetic wave propagation. Next, we focus on the effects of turbulent fluctuations on electromagnetic wave propagation. Then, the principles of reflectometry for both profile and fluctuation measurements are presented, based on the concept of wave reflection on plasma cut-off layers. The fixed-frequency reflectometer used in this thesis is then introduced.

After the introduction of turbulence and reflectometry, the main studies of this thesis are included in chapters 4–6:

- **Chapter 4** is dedicated to the parametrization of the fluctuation frequency spectra, focusing on the optimization of the spectrum fitting process. Different fitting models will be compared..

- **Chapter 5** focuses on the radial profiles of the broadband fraction of the frequency spectra in both Ohmic and L-mode plasmas. In the end, a link between the broadband fraction and the density fluctuation level is developed.

- **Chapter 6** discusses collisional effects on the frequency spectra in Ohmic and L-mode plasmas. We then propose an interpretation in terms of a transition of the dominating instability, supported by earlier gyrokinetic simulations, to explain the observed results. Further evidence is provided by analysis of the density peaking and study of the low-frequency components of the spectra.

Finally, **chapter 7** summarizes the main results and provides conclusions of this thesis. Some pending issues and motivation for future work is discussed.

Chapter 2

Turbulence

Contents

Turbulence gives rise to fluctuations of density $\tilde{n}$, temperature $\tilde{T}$, electric potential $\tilde{\phi}$ and magnetic field $\tilde{\mathbf{B}}$ in fusion plasmas, and therefore has an influence on the confinement performance and the radial transport of energy and particles. In this chapter, first the general properties of turbulence are introduced in section 2.1. Then, we focus on plasma turbulence in magnetic confinement devices and its effects on the confinement and transport, as discussed in Section 2.2. Plasma turbulence in tokamaks is driven by drift wave instabilities, among which TEM and ITG modes play the most important role in the core region, as detailed in Section 2.3. Finally, we focus on the properties of density fluctuations $\tilde{n}$ in Section 2.4.

2.1 General properties of turbulence

Turbulence is a state of irregular fluid motion (liquids, gases, plasmas). It is a commonly observed phenomenon in both nature and our daily lives, such as water flow around an obstacle, air flow in the atmosphere or around the wing of an aeroplane, smoke from a chimney, etc. Although turbulence is ubiquitous, experimental characterization and computer modeling of the phenomenon are highly complicated due to the nonlinearity, hence strong dependence on initial conditions, and dynamics at multiple length and time scales. A comprehensive theoretical model is still lacking, although various aspects of turbulence have been studied in detail, e.g., the transition from laminar to turbulent flow in liquids [Chu 1993] or the effects of plasma turbulence on global energy confinement and transport [Truc 1986, Garbet 1992].

2.1.1 Generation of turbulent phenomena

Considering first a neutral fluid, the onset of turbulence can be characterized empirically by a dimensionless parameter called the *Reynolds number*:

$$R_e = \frac{uL}{\nu}. \tag{2.1}$$

Here, u, L and ν denote the fluid velocity, the characteristic linear dimension of the system and the kinematic viscosity, respectively. The Reynolds number can be regarded as the ratio between the inertial forces and the viscous forces in a fluid. At low Reynolds number, when the viscous forces are dominant, the fluid exhibits relatively regular motion, referred to as *laminar flow*. At high Reynolds number, when the fluid motion is typically dominated by inertial forces, a turbulent flow develops because of instabilities driven by the inertial forces. Figure 2.1 shows an example where a cylinder is positioned in a flowing fluid with varying Reynolds number (R_e). When $R_e \gg 1$, turbulent flow appears in the downstream region of the cylinder.

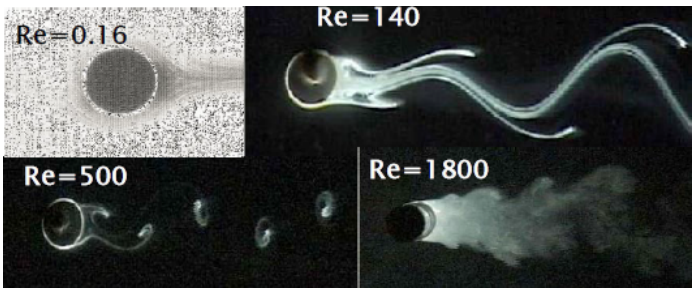

Figure 2.1: Formation of turbulence behind a cylinder placed in a fluid flow, gradually increasing the Reynolds number (R_e). The experimental conditions to change the characteristic parameters of u, L, ν can be found in [Acheson 1990, Pope 2000].

Historically, Reynolds's dye experiments in 1883 led him to define the Reynolds number as a good indicator of fluid turbulence. However, no clear origins or driving mechanisms of turbulence were proposed following this experimental investigation. Deeper

theoretical studies revealed that turbulence is caused by fluid instabilities[1]. From figure 2.1, one observes a highly distorted surface that separates regions of turbulent and non-turbulent flow. Regions of turbulent flow are characterized by large vorticity, which describes the local spinning motion of a continuum near some point or in other words the tendency of rotation [Acheson 1990]. In contrast, non-turbulent flow is essentially irrotational. Another feature of turbulence is its intermittency, meaning that at fixed position in a fluid, the motion may at times be irregular and other times non-turbulent [Acheson 1990]. Together, the high irregularity at multiple scales and the intermittent nature call for a statistical description of turbulence.

2.1.2 Energy cascade, eddies and vortices

Now consider a fully turbulent flow at high Reynolds number. An important property in turbulence is the appearance of *vortices* [Ting 1991]. A vortex is a region in a fluid in which the flow revolves around an axis line with non-vanishing vorticity (curl of the velocity). Once formed, vortices can move, stretch, twist and interact with each other in complicated ways. A moving vortex carries with it momentum, energy, and mass.

In addition, a region of swirling, moderately coherent motion of fluid in a turbulent flow is called an *eddy*. A region occupied by a large eddy can also contain smaller eddies [Pope 2000], as can be seen in figure 2.1. The largest eddies are characterized by a length scale which is comparable to the turbulent flow scale. According to the important concept of Richardson's *energy cascade* [Richardson 1922], the large eddies are unstable and transfer their energy to smaller eddies. At the smallest scales the Reynolds number is sufficiently small such that viscosity becomes effective in dissipating the kinetic energy [Pope 2000].

Figure 2.2 illustrates the energy cascade process by means of the wavenumber (k) and energy $E(k)$. Large eddies have low wavenumber and small eddies have large wavenumber. The intermediate range of scales is called inertial subrange and has been studied by A. Kolmogorov using self-similarity [Kolmogorov 1941]. Kolmogorov's hypotheses led to the following universal form for the energy spectrum:

$$E(k) \propto k^{-5/3}, k > k_{inj}. \tag{2.2}$$

Thus, in a turbulent system energy is injected at large spatial scales (low k) and dissipated at small spatial scales (high k). This energy transfer from large towards small structures is observed in three-dimensional isotropic turbulence and is usually called the direct cascade. However, in the framework of a two-dimensional anisotropic turbulent system [Kraichnan 1971], except for the direct cascade, the energy can also be transferred from small to large scales, called the inverse cascade. In this case, the energy spectrum can be

[1] To the turbulent flow in fluids, the main instabilities are the Kelvin-Helmholtz instability and the Rayleigh-Taylor instability.

described as:

$$E(k) = k^{-5/3}, k < k_{inj}, \tag{2.3}$$
$$E(k) = k^{-3}, k > k_{inj}. \tag{2.4}$$

Here, a knee point ($k = k_{inj}$) appears in the energy spectrum. Note that in plasma turbulence observed experimentally, the situation can be even more complicated and several injection scales can coexist simultaneously, leading to possible changes of the spectral indices. The energy spectrum will be useful to determine the main contributions to the turbulence signals in the remainder.

Due to the formation of eddies and vortices in turbulent flow, energy and particles exhibit additional transverse motions which enhances the rate of energy and momentum exchange between different regions of the flow. This increases heat transfer, particle transport and friction coefficient. In fact, in engineering applications, most systems with fluid motion are in a turbulent regime rather than a stable state. In these systems, energy and particle transport is dominated by turbulent transport rather than collisional transport. Turbulence and the resulting enhanced transport can be harmful or beneficial, depending on the situation.

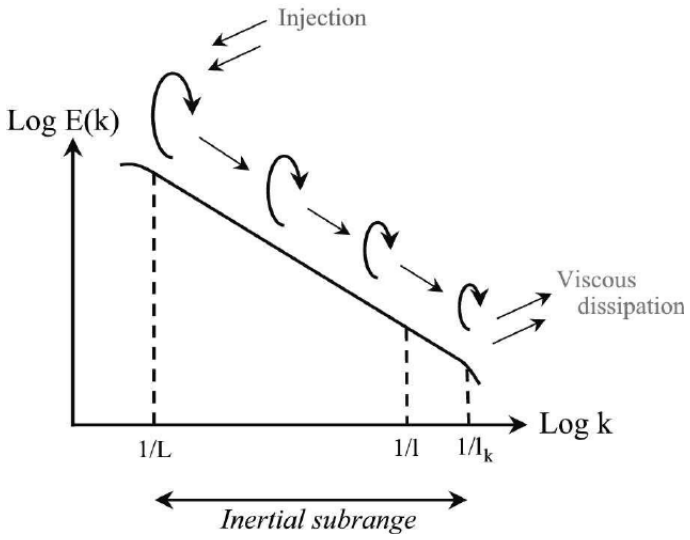

Figure 2.2: Schematic illustration of the energy cascade process of turbulence. The energy injection and viscous dissipation occur at large (low k) and small (high k) scale, respectively. Here, the energy injection occurs at $k_{inj} \sim 1/L$. Adapted from [Frish 1995].

2.2 Turbulent transport in magnetically confined fusion plasmas

In analogy with fluids, in MHD theory fusion plasmas are considered as quasi-neutral fluids of charged particles subject to hydrodynamic and electromagnetic forces. Under

certain conditions, fusion plasmas exhibit turbulence, involving irregular, self-regulating structures and dynamics, causing energy [Wootton 1990, Rice 2012] and particle transport [Angioni 2009] to be dominated by turbulent transport rather than collisional transport. Here, the same two-edged situation may occur for fusion plasma turbulence. Although plasma turbulence can be advantageous to lessen impurity accumulation in the core region in fusion devices, it is deleterious to the confinement performance by increasing the loss rate of energy and particles. Therefore, understanding and controlling plasma turbulence is a key research topic in fusion science. In this section, we focus on magnetically confined fusion plasmas and the turbulence-related energy and particle transport, as well as different confinement regimes..

2.2.1 Turbulence-induced confinement degradation

The most straightforward way to demonstrate the link between turbulence and transport in fusion plasmas is to build a relation between the characteristics of the turbulence level and the energy confinement time. The global energy confinement time is defined as the typical time it would take for the plasma energy to leave the system through transport processes (not accounting for radiation), if all heating sources were suddenly switched off. It is calculated as the ratio of the total stored plasma energy over the power lost through the separatrix.

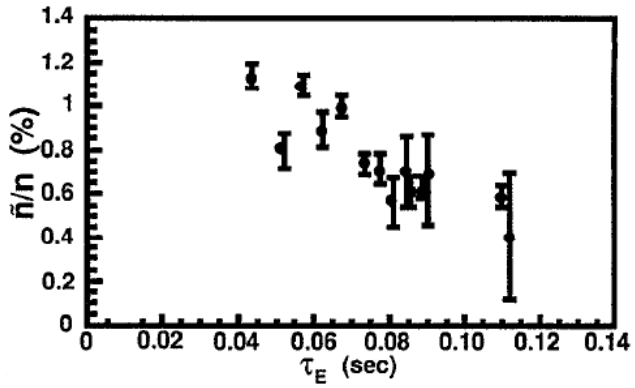

Figure 2.3: Turbulence level ($\widetilde{n}/n$) measured from beam emission spectroscopy (BES) versus the energy confinement time (τ_E) for an Ohmic discharge in TFTR. Adapted from [Paul 1992].

Quantitative analyses of the turbulence level and the confinement time have been carried out through power scans in many tokamaks such as TFR (Tokamak de Fontenay-aux-Roses) [Truc 1986] and TFTR (Tokamak Fusion Test Reactor) [Paul 1992]. In TFR, The analyses have been conducted with ICRH and NBI and a negative correlation between the turbulence level and the confinement time was observed. In TFTR, the similar trend, i.e., the global energy confinement time (τ_E) is approximately inversely proportional to the density fluctuation level ($\widetilde{n}/n$), was recovered in Ohmically heated plasmas, as shown in figure 2.3. These results (together with many confirms from other devices) indicate that turbulence indeed plays a major role in determining the confinement time.

2.2.2 Heat transport

One way to quantify the relation between turbulence and transport is to experimentally determine the corresponding effective heat transport coefficients. The effective heat transport coefficient χ_s is defined through the following formula:

$$\mathbf{q_s} = -n_s \chi_s \nabla T_s, \tag{2.5}$$

with $\mathbf{q_s}$, n_s and T_s the heat flux vector, density and temperature of each specific species s. The heat transport coefficient of electron and ions (χ_e and χ_i) can be estimated experimentally, roughly resulting in $\chi_e^{exp} \sim \chi_i^{exp} \sim 1 m^2 s^{-1}$.

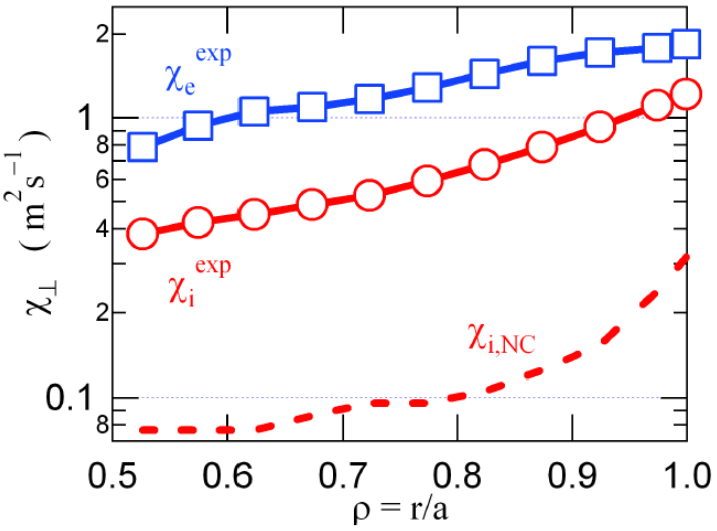

Figure 2.4: Experimental estimates of electron and ion heat transport coefficients and neoclassical value from the tokamak Tore Supra. From [Sarazin 2012].

On the other hand, Coulomb collisions also contribute to the radial transport. Transport in a toroidal geometry is described by neoclassical transport theory, considering the inhomogeneity of the magnetic fields and the population of trapped particles (figure 1.7). The precise derivation of the neoclassical transport coefficients in the different collisional regimes can be found in [Hinton 1976]. They can be related to the corresponding coefficients in classical cylindrical geometry, as follows:

$$\chi_s^{NC} \sim q^2 (r/R)^{-3/2} \chi_s^C, s = e, i. \tag{2.6}$$

Here, q is the safety factor, r the radial position in a poloidal cross-section and R the major plasma radius. The classical coefficients are given by $\chi_e^C \sim \nu_{ee} \rho_e^2$ and $\chi_i^C \sim \nu_{ii} \rho_i^2$, where ν_{ee} (ν_{ii}) and ρ_e (ρ_i) are the electron (ion) collision frequency and Larmor radius. The transport spatial scale of neoclassical theory is the width of the banana orbit, which is much larger than the classic Coulomb collision scale (the Larmor radius). This explains why neoclassical transport is stronger than the corresponding classical transport.

The experimentally determined transport coefficients (χ_i^{exp}, χ_e^{exp}) and the theoreti-

cal prediction from neoclassical theory (χ_i^{NC}) are shown in figure 2.4 for a Tore Supra discharge. The experimental estimates are still much larger than those obtained from neoclassical theory, at all the radial positions. Numerous experiments indicate that $\chi_i^{exp} \gg \chi_i^{NC}$ and $\chi_e^{exp} \gg \chi_e^{NC}$. The large unexpected transport coefficients observed experimentally thus can not be explained by any collision-based theory and is conventionally referred as *anomalous transport*, which is believed to be caused by turbulence.

2.2.3 Particle transport

After evaluating the influence of turbulence on energy confinement, now we focus on another important transport in fusion plasmas: particle transport. Particle transport is a central question due to the fact that fusion power increases as the square of the density, so the existence and nature of any process that leads to density peaking deserves attention [Garbet 2004]. The degree of density peaking is also useful to self-generate a large fraction of non-inductive current required for continuous operation [Bourdelle 2005].

Particle transport in tokamaks is different from heat transport, since the heat source is usually located in the core region but the particle source is often only located in the edge region. Nevertheless, density profiles can still be peaked in the central region due to an inward particle pinch. Therefore, the particle transport flux includes a diffusive and a convective (pinch) term:

$$\mathbf{\Gamma} = -D\nabla n + \mathbf{V}n. \tag{2.7}$$

Here, n is the local density, D the diffusion coefficient and $\mathbf{V}$ the pinch velocity. In terms of generation mechanism, the particle flux $\mathbf{\Gamma}$ can be divided into two parts:

$$\mathbf{\Gamma} = \mathbf{\Gamma}_{neo} + \mathbf{\Gamma}_{turb}, \tag{2.8}$$

where $\mathbf{\Gamma}_{neo}$ and $\mathbf{\Gamma}_{turb}$ are generated by the neoclassical transport and the turbulence, respectively. Here, we assume there is no coupling effect between the two terms. The neoclassical part is attributed to the Ware pinch [Ware 1970], causing the trapped particles with density n_t to move towards the magnetic axis with a radial velocity V_{neo}, satisfying:

$$\mathbf{\Gamma}_{neo} = \mathbf{V}_{neo} n_t, \tag{2.9}$$

with

$$\mathbf{V}_{neo} = -\frac{E_\phi}{B_\theta}\mathbf{e_r}, \tag{2.10}$$

with $\mathbf{e_r}$ the unit vector in the radial direction. Here, E_ϕ and B_θ are the magnitude of the toroidal electric field and the poloidal magnetic field, respectively. The anomalous part of the particle flux caused by turbulence can be written as [Bourdelle 2005]:

$$\mathbf{\Gamma}_{turb} = -D_{turb}\nabla n + \mathbf{V}_{turb} n, \tag{2.11}$$

where $\mathbf{V}_{turb}$ is the turbulent pinch velocity, D_{turb} is the turbulent diffusion coefficient, and n is the density. There are two main mechanisms that contribute to $\mathbf{\Gamma}_{turb}$: the turbulence equipartition (TEP) and the thermodiffusion. TEP is related to the geometric

effect of magnetic fields. It is found that the density of trapped particles is inversely proportional to q. Since q increases from the core to the edge, a peaked profile forms. The thermodiffusion term predicts a velocity pinch when $(\nabla T/T)/(\nabla n/n)$ is sufficiently high. The existence of the turbulent pinch velocity has been proved experimentally in modulated Tore Supra discharges, as shown in figure 2.5 [Hoang 2003]. The inward pinch velocity $\mathbf{V}$ from the peaked density profile can only be explained by a turbulent pinch, as the poloidal electric field hence the neoclassical Ware pinch are kept at zero in these shots.

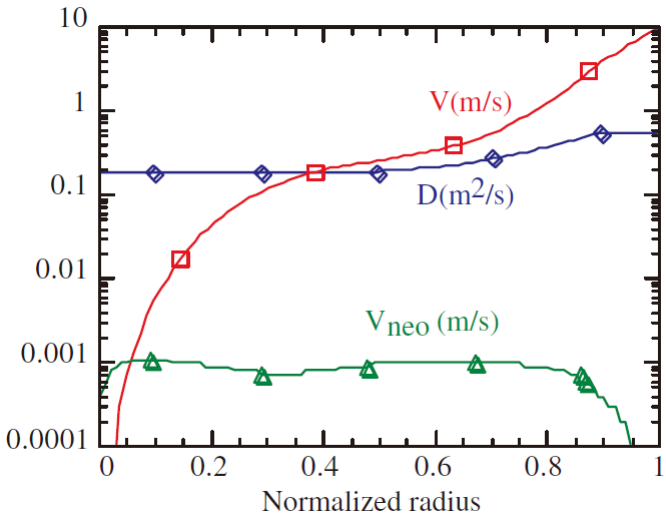

Figure 2.5: The pinch velocity (V) and the diffusion coefficient (D) calculated from the density profile when the neoclassical contribution remains small. This has been realized by long-pulse LHCD discharges with zero toroidal electric field E_ϕ [Hoang 2003].

2.2.4 Confinement regimes

The effects of turbulence on confinement and transport depend on confinement regime. The various confinements regimes can be achieved by adapting global plasma parameters and external heating power. Optimization of confinement performance and exploration of suitable confinement regimes constitutes a central topic in fusion science.

Ohmic confinement regime

When only Ohmic heating is applied to the plasmas, it is said to be in the Ohmic confinement regime. In this regime, the relation between the confinement time and the density has been studied extensively [Yushmanov 1990b]. At low densities, the confinement time τ_E increases linearly with the increase of the density, characterizing the so-called *linear Ohmic confinement* (LOC). Above a critical density threshold, the confinement time τ_E saturates, reaching the *saturated Ohmic confinement* (SOC) regime. Figure 2.6 shows the energy confinement time as a function of average electron density for a series of Ohmic

discharges, exhibiting a clear transition from LOC to SOC as density increases. In between the two regimes, a transition regime exists. The saturation of the confinement in the SOC regime may be linked to different regimes of micro-instabilities, as discussed in the next section.

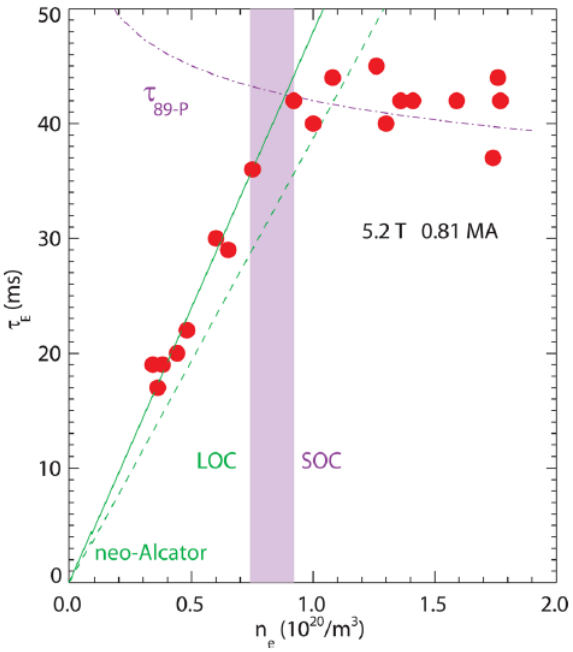

Figure 2.6: Energy confinement time as a function of the central line-averaged electron density. Adapted from [Rice 2012].

L-mode confinement

As the effectiveness of Ohmic heating decreases for increasing temperatures (decreasing plasma resistivity), additional heating methods are required to increase the plasma energy content beyond that obtained with Ohmic heating. This can be achieved by injecting energetic neutral particles or radio-frequency waves. At relatively low levels of auxiliary heating power, it was found that the confinement time decreases with heating power—a regime referred to as the *low confinement mode* (L-mode). Studying L-mode physics is important to increase understanding of turbulent transport and confinement, hence providing useful information for reaching and maintaining H-mode.

H-mode and other improved confinement regimes

It was found that tokamak operation makes an abrupt transition from the low confinement mode (L-mode) to the *high confinement mode* (H-mode) when the auxiliary heating power reaches a critical value with the diverter in X point configuration. The underlying physical mechanisms of the L-H transition are still unclear, but it is known to be related to the suppression of turbulent transport [Shaing 1990, Groebner 1990, Manz 2012, Schmitz 2012]. Empirical scaling laws for the threshold power in terms of global plasma parameters have

been investigated extensively [Ryter 1998, Connor 2000, Verdoolaege 2015]. The confinement time of the H-mode regime is at least twice as large compared to the L-mode regime. However, the price to pay is the spontaneous appearance of MHD instabilities near the plasma boundary, the so-called *edge-localized modes* (ELMs) [Zohm 1996, Connor 1998, Howard 2008, Leonard 2014]. The study of ELMs is an important topic in itself, primarily since in ITER they may pose a danger for the plasma-facing components.

Apart from the H-mode, several other types of improved confinement regimes have been achieved by local turbulence suppression. This includes the supershots on TFTR [Levinton 1995], the pellet-enhancement performance (PEP) on JET (Joint European Torus) [Smeulders 1995], the very high confinement mode (V-H mode) on DIII-D (Doublet III-D tokamak) [Jackson 1991]. In the region where turbulence is suppressed, the formation of a barrier at the edge reduces the radial transport and thus promote the confinement.

The many different types of the confinement regimes reflect a lack of understanding of the underlying physics. In the present PhD work, we concentrate on Ohmic and L-mode confinement with the goal to increase understanding of the general properties of turbulence and transport.

2.3 Drift wave turbulence

In the core region of fusion plasmas, drift waves are the main turbulence mechanism. Drift waves have many different forms, depending on the driving source. The main drift waves that strongly affect transport are the *trapped electron modes* (TEM), *ion temperature gradient* (ITG) modes and *electron temperature gradient* (ETG). In this section, drift motion in magnetic fields and drift wave generation mechanisms are described first. Then, we discuss the scale and driving mechanism of TEM and ITG modes, the two main instabilities treated in this study. Finally, turbulence saturation due to zonal flows is touched upon.

2.3.1 Drift motion in magnetized plasmas

In magnetized plasmas, when an electric field arises perpendicular to the magnetic field, the charged particles undergo a drifting motion perpendicular to both electric and magnetic fields. This $E \times B$ drift occurs with a velocity given by

$$\boldsymbol{v}_E = \frac{\mathbf{E} \times \mathbf{B}}{B^2}. \tag{2.12}$$

Note that $\boldsymbol{v}_E$ is independent of charge and mass, so it is the same for electrons and ions.

In the MHD description [Freidberg 2007, Bittencourt 2004, Goldston 1995], a fluid element including many charged particles can also undergo an $E \times B$ drift. However, another drift motion occurs due to the appearance of the pressure gradient term (∇p) in

the equation of motion:

$$mn\left[\frac{\partial \mathbf{v}}{\partial t} + (\mathbf{v}\cdot\nabla)\mathbf{v})\right] = qn(\mathbf{E} + \mathbf{v}\times\mathbf{B}) - \nabla p, \tag{2.13}$$

where m, n, q and $\mathbf{v}$ are the mass, density, charge and velocity of the fluid element, $\mathbf{E}$ and $\mathbf{B}$ the electric and magnetic fields. Then, the drift velocity of this so-called *diamagnetic drift* is given as

$$\boldsymbol{v}_D = -\frac{\nabla p \times \mathbf{B}}{qnB^2}. \tag{2.14}$$

The drift $\boldsymbol{v}_D$ does depend on the type of charges, giving rise to charge separation, and thus an electrostatic field.

2.3.2 Drift wave instabilities

Figure 2.7 illustrates the physical mechanism of drift waves in a cylindrical geometry. First, consider an electric potential perturbation according to a plane wave $\exp[i(k_y y - \omega t)]$. The electrons can flow along the magnetic field to establish a thermodynamic equilibrium. So in the isothermal compression limit, the Boltzmann relation of the electron response $n_e = n_0 \exp(e\phi/T_e)$ gives:

$$n_1/n_0 \approx \exp(\phi_1/T_e), \tag{2.15}$$

where n_1 and ϕ_1 are the electron density and electric potential perturbations. The potential perturbation ϕ_1 corresponds to an electric field perturbation $\mathbf{E}_1$, causing a drift $\boldsymbol{v}_1 = \mathbf{E}_1 \times \mathbf{B}_0/B^2$ in the x direction. $\boldsymbol{v}_1$ changes sign periodically because $\mathbf{E}_1$ changes sense. Since n_1 and ϕ_1 are in phase, the net result is an oscillation of the drift wave with a phase velocity along the y direction. The drift wave frequency satisfies:

$$\omega = k_y v_{De}, \tag{2.16}$$

where v_{De} is the electron diamagnetic drift velocity.

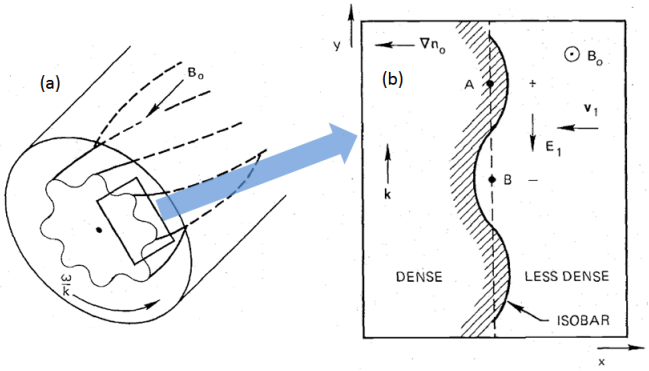

Figure 2.7: Physical mechanism of the drift waves. (a) is an enlarged part from (b) the cross section in a cylindrical geometry. Adapted from [Chen 2006]

Consider now the case when n_1 and v_1 are out of phase, which can be caused by various mechanisms such as the plasma resistivity. The resistivity effect makes the potential perturbation ϕ_1 lag behind the density perturbation n_1. This phase lag causes $\boldsymbol{v}_1$ to be outward where the plasma has already been shifted outward and the perturbation grows.

2.3.3 Microinstabilities in the core region

Many types of drift wave instabilities can coexist in fusion plasmas. In the core region, the dominating instabilities are trapped electron modes (TEM), ion temperature gradient (ITG) modes, and electron temperature gradient (ETG) modes. The typical wavenumber scales of these modes are shown in figure 2.8.

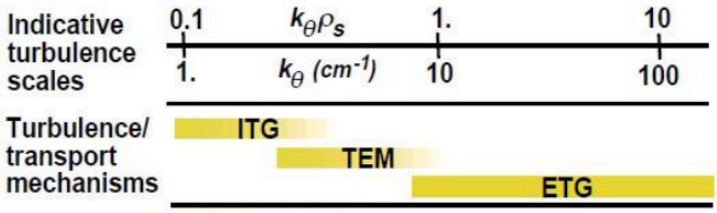

Figure 2.8: Spatial scale of ITG, TEM and ETG instabilities in wavenumber and normalized wavenumber.

TEM and ITG are driven by the electron temperature gradient R/L_{T_e} and the ion temperature gradient R/L_{T_i}, respectively. Here, L_{T_e} and L_{T_i} are the electron and ion temperature scale length ($L_{T_s} = -T_s/\nabla T_s, s = i, e$). Accordingly, TEM has its phase velocity in the electron diamagnetic direction and ITG has a phase velocity in the ion diamagnetic direction. The stabilization of the modes is also related to the electron density gradient R/L_{n_e}, with $L_{n_e} = -n_e/\nabla n_s$ the density scale length. The stability diagram of TEM and ITG is shown in figure 2.9, reflecting the complicated interactions and transitions between the two instabilities [Garbet 2010].

One important issue in studying turbulence in fusion plasmas is to identify the dominating plasma instability, depending on plasma conditions. From figure 2.8, TEM and ITG are partly overlapping in terms of wavenumber, making it difficult to distinguish between them. An effective experimental technique to discriminate among TEM and ITG is through the so-called thermodiffusion term in the particle transport analysis [Bourdelle 2007]. From (2.11), both the turbulence equipartition (TEP) and the thermodiffusion term contribute to the convection velocity V_{turb}. The TEP term (the curvature pinch) is always directed inwards, whereas the thermodiffusion term can be directed outwards when TEM are dominant and inwards when ITG modes are dominant [Bourdelle 2005].

With a much larger wavenumber, ETG modes can be easily distinguished from the other two instabilities. Moreover, since ETG modes usually make a weaker contributions to the radial transport due to their small scales [Garbet 2001] and the high wavenumber is beyond the capability of the diagnostic systems used in this study, we will focus on TEM and ITG hereafter.

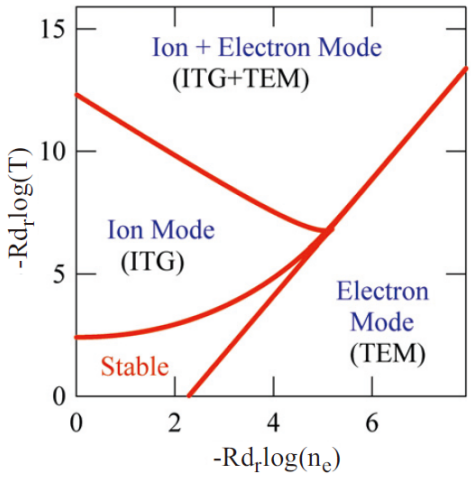

Figure 2.9: Stability range of ITG and TEM under the condition $T_e = T_i$. Adapted from [Garbet 2004].

2.3.4 Effects of collisions

Collisions have been found to have a crucial impact on the determination of the micro-instabilities [Vermare 2011], since collisions can affect the trapped particle modes via the detrapping mechanism, i.e. collisions tend to stabilize the TEM modes. Among various definitions of collisionality, the effective collisionality (ν_{eff}) for drift wave instabilities has been adopted as an excellent indicator for TEM stabilization. It is defined as the ratio between the electron-ion collision frequency and the curvature drift frequency: $\nu_{\text{eff}} = \nu_{\text{ei}}/\omega_{\text{De}}$ [Angioni 2003, Garbet 2004]. For ITG and TEM instabilities, the curvature drift frequency provides an estimate of the mode growth rate, and is defined as $\omega_{\text{De}} = 2k_\perp \rho_L c_s/R$, with $k_\perp$ the perpendicular wave number, ρ_{L} the ion Larmor radius, R (m) the major radius and c_{s} the ion acoustic velocity. Accordingly, ν_{eff} has been approximated as follows [Angioni 2003, Conway 2006]:

$$\nu_{\text{eff}} \approx 0.1\, R\, Z_{\text{eff}}\, n_{\text{e}}\, T_{\text{e}}^{-2}, \tag{2.17}$$

where Z_{eff} is the effective charge number, n_{e} (10^{19} m^{-3}) the electron density and T_{e} (keV) the electron temperature. In this approximation, the normalized perpendicular wave number $k_\perp \rho_L$ has been estimated to be $\sqrt{0.1}$, which is the characteristic value for core density fluctuations.

In Ohmic plasmas, the transition from the LOC to SOC confinement regime has been attributed in previous studies to a change in the dominant instability from TEM to ITG modes [Angioni 2005, Erofeev 2017]. Experimentally, this connection between confinement regime and dominant micro-instability has also been studied through the dependence of the density peaking on the collisionality in various devices such as Alcator C-Mod and ASDEX Upgrade [Rice 2012, Lebschy 2018] in both L-mode and H-mode plasmas. The density peaking can be seen as a signature of turbulent pinch velocity. A net inward turbulent pinch gives rise to a peaked density profile with large density

peaking and a net outward pinch leads to a flat profile with small density peaking.

Figure 2.10 (b) shows the evolution of density peaking with effective collisionality (ν_{eff}) at different safety factors. At lower ν_{eff}, when TEM instability dominates, the density peaking decreases rapidly with ν_{eff}, whereas at higher ν_{eff} when TEM may be stabilized, the trend in the density peaking becomes weak and reaches saturation. This may indicate a transition between two turbulence regimes, with a threshold around $\nu_{\text{eff}} = 1$. Since the effective collisionality is influenced by density, temperature and ion effective charge number, the trends in 2.10 (b) is more clear than in 2.10 (a), where only the change of density is considered.

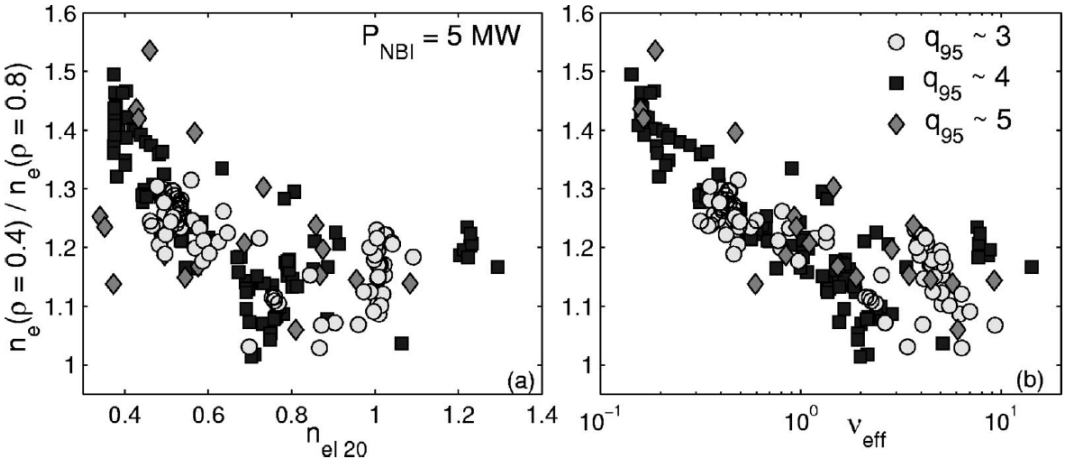

Figure 2.10: Evolution of density peaking with (a) the density and (b) collisionality with NBI in ASDEX Upgrade. Adapted from [Angioni 2003].

2.3.5 Turbulence saturation and suppression

In the linear growth phase, where the increase of the free energy is driven by strong gradients, the magnitude of drift wave instabilities increases, while the linear damping decreases. After the magnitude reaches a threshold, nonlinear interactions appear such as the wave-wave coupling, when $\omega = \omega_1 \pm \omega_2$ or $\mathbf{k} = \mathbf{k}_1 \pm \mathbf{k}_2$. Finally, the nonlinear phase develops into a saturated turbulent state. Different from turbulence in fluids, the parameters in plasma turbulence in tokamaks are usually around the density and temperature threshold. This could be due to the existence of zonal flows (ZFs), which exhibit complex interaction with turbulence through the predator-prey model [Diamond 2005].

ZFs are symmetric in both poloidal and toroidal direction, in other words, ZFs have finite wavenumber only in the radial direction. They are elongated vortex modes with zero frequency, which make it very difficult to detect them. From the theoretical point-of-view, zonal flows are generated by turbulence, but they have a suppressing effect on turbulence generation and propagation. ZFs can break the turbulent eddies into smaller ones and thus greatly reducing their radial transport. Other turbulence suppression effects are velocity shear from plasma rotation and magnetic shear by constructing proper profiles of the safety factor (or plasmas current).

2.4 Density fluctuations

In the saturated (fully developed) state, turbulence can induce fluctuations of various plasma parameters, such as δn, δT, $\delta\phi$ and $\delta\mathbf{B}$. Most measurements of turbulence rely on δn due to the higher sensitivity of diagnostics than the other fluctuations.

2.4.1 Radial profiles of the fluctuation level

The density fluctuation level δn is very important due to its direct link with confinement performance. The relative magnitude $\delta n/n$ is usually connected with different confinement regimes. Many studies have been dedicated to the determination of $\delta n/n$ under various plasma conditions and heating scenarios.

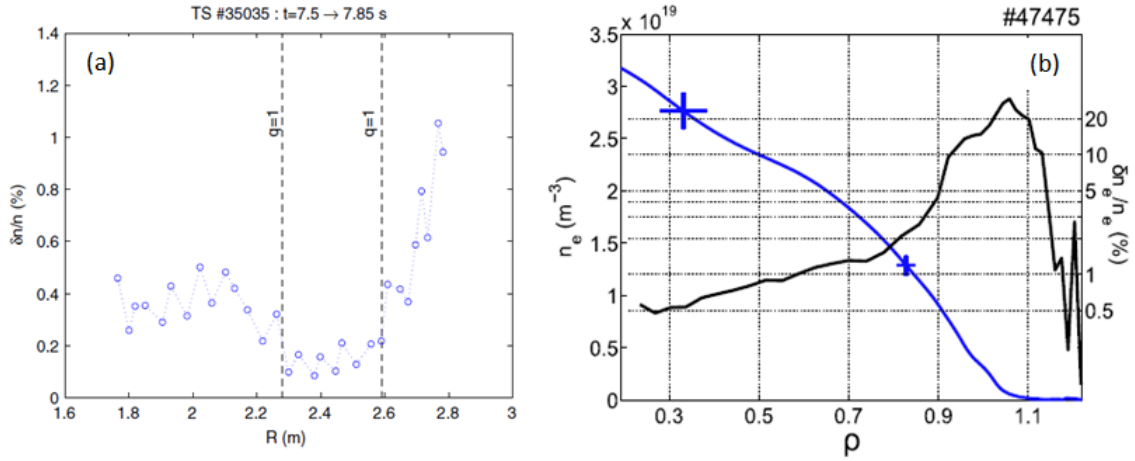

Figure 2.11: Density fluctuation level in the (a) core and (b) edge region in Tore Supra ohmic discharges. From [Sabot 2006b, Hornung 2013a].

Figure 2.11 shows the radial profile of $\delta n/n$ in Ohmic plasmas. The complete radial profile, from the LFS through the center to the HFS, of $\delta n/n$ measured by fixed-frequency reflectometry is shown in figure 2.11 (a). It is clear that $\delta n/n$ remains at a low level ($<$ 0.2%) near the central region, especially inside the $q = 1$ surface, where linear turbulence dominates. Towards the edge region, $\delta n/n$ increases rapidly and specifically at the LFS near the edge $\delta n/n$ can be larger than 1%. At the HFS, $\delta n/n$ remains at a moderate level. Figure 2.11 (b) shows the profiles of density (n) and density fluctuation level (2.11) measured by fast-sweeping reflectometry in the edge region for another discharge. From the core region to the edge region, $\delta n/n$ first increases slowly, then rapidly near the last-closed magnetic surface ($\rho \sim 1$), which is consistent with the observations in figure 2.11 (a).

Furthermore, $\delta n/n$ with different heating scenarios is shown in figure 2.12. With auxiliary heating, $\delta n/n$ still increases from the center to the edge, but the magnitude of $\delta n/n$ is systematically higher at all radial positions. Comparing the pure ICRH ($P_{\mathrm{ICRH}} =$ 4.7 MW) with the mixed heating scheme ($P_{\mathrm{ICRH}} + P_{\mathrm{LH}} = 4$ MW), the effect of ICRH turns out to be stronger than that of LH heating.

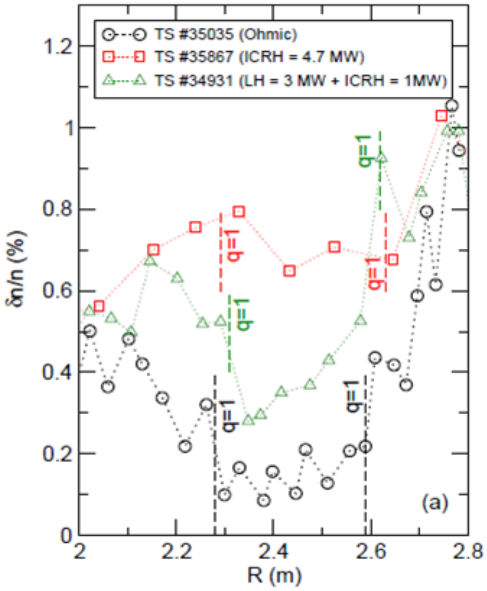

Figure 2.12: Density fluctuation level with auxiliary heating methods compared with the Ohmic plasmas. From [Sirinelli 2006].

2.4.2 Diagnostics for density fluctuations

Although the above profiles of the density fluctuation level have been measured by reflectometry diagnostics, many other diagnostic methods have been developed for measuring density fluctuations. Every diagnostic has its specific working conditions and limitations.

Langmuir probes (LPs) are the simplest and most accurate measurement technique, able to measure fluctuations of n, T and ϕ simultaneously. By measuring the fluctuation of saturation currents $\widetilde{I_{sat}}$, one can obtain directly the density fluctuations $\widetilde{n}$. Although LPs have been widely used in low-temperature plasmas, their application in tokamaks is restricted to the edge region, due to the hostile plasma conditions. Even the improved fast-reciprocating LP can only be inserted a few centimeters deeper, but can not reach the central plasma region. Other diagnostics such as heavy ion beam probes (HIBP) and beam emission spectroscopy (BES) have been developed to detect density fluctuations in the core region, but they can probe only a limited spatial range and have limited accuracy and spatial resolution [Bretz 1997].

On the other hand, reflectometry is a versatile diagnostic, able to measure $\widetilde{n}$ at multiple positions with high spatial and temporal resolution. By measuring the phase fluctuation $\widetilde{\phi}(t)$ in the acquired signal, the density fluctuations $\widetilde{n}(t)$ can be obtained through a transfer function. Moreover, by using multiple antennas and a correlation technique (see appendix A), reflectometry can also provide the energy distribution from the power or wavenumber spectra, as well as the correlation length and time of the turbulent eddies, and the rotation of the turbulence structures. These advantages make reflectometry a powerful diagnostic tool for studying turbulence in fusion plasmas. The details of reflectometry are presented in the next chapter.

Chapter 3

Reflectometry

Contents

Reflectometry is a radar-like technique, which uses the reflection of waves inside the plasmas to measure the electron density and density fluctuations in fusion plasmas. Since the intensity of the waves is usually very low (< 1 W), the waves cause negligible perturbation to the local plasmas properties.

In this chapter, in section 3.1 we first provide the theoretical basis for reflectometry through propagation of electromagnetic waves in plasmas. The dispersion relations and the refraction index of EM waves in plasmas are derived from the Maxwell equations and plasma properties. This is followed by some important concepts, viz. polarization, resonance and cut-off. The effect of fluctuations on the wave propagation is discussed in section 3.2. Then, the experimental principles of reflectometry are presented in section 3.3. Finally, in section 3.4 we focus on the core reflectometry diagnostic at Tore Supra, as well as the density fluctuation measurements by this diagnostic that are used in this study.

3.1 Electromagnetic waves propagation in plasmas

Wave propagation in magnetized plasmas is significantly more complicated compared to propagation in non-magnetized media, as the magnetic field causes highly anisotropic dynamics parallel and perpendicular to the magnetic field. We therefore focus first on the basics of EM wave propagation in magnetized plasmas, before proceeding to the particularities of wave propagation for reflectometry applications.

3.1.1 Dispersion relation

In the MHD approach to plasma dynamics, a plasma is treated as a continuous medium wherein currents can flow. The corresponding electric and magnetic fields have to obey the Maxwell equations, the differential forms of which are:

$$\nabla \times \mathbf{E} = -\frac{\partial \mathbf{B}}{\partial t}, \tag{3.1}$$

$$\nabla \times \mathbf{B} = \mu_0 \mathbf{j} + \frac{1}{c^2}\frac{\partial \mathbf{E}}{\partial t}. \tag{3.2}$$

The plasma properties are reflected by the current density $\mathbf{j}$. There could be unperturbed (or equilibrium) values of the magnetic and electric fields $\mathbf{B_0}$ and $\mathbf{E_0}$ that are independent of the waves being considered. In this case, (3.1) and (3.2) are applied to the unperturbed and wave parts separately and here only the wave parts are considered. One can eliminate $\mathbf{B}$ by taking $\nabla\times$ of (3.1) and $\frac{\partial}{\partial t}$ of the second, amounting to the following wave equation:

$$\nabla \times (\nabla \times \mathbf{E}) + \frac{\partial}{\partial t}\left(\mu_0 \mathbf{j} + \frac{1}{c^2}\frac{\partial \mathbf{E}}{\partial t}\right) = 0. \tag{3.3}$$

Now, assuming that the wave fields are small compared to the equilibrium values and that the plasma is spatially homogeneous, the wave fields can be expressed by the sum of Fourier series (modes):

$$\mathbf{E}(\mathbf{x}, t) = \int \mathbf{E}(\mathbf{k}, \omega) e^{i(\mathbf{k}\cdot\mathbf{x} - \omega t)} \mathrm{d}\mathbf{k}\mathrm{d}\omega, \tag{3.4}$$

where each Fourier mode $\mathbf{E}(\mathbf{k}, \omega)$ satisfies (3.3). As the wave fields are small, the current ($\mathbf{j}$) is a linear function of the electric field ($\mathbf{E}$). Therefore, for each Fourier mode, the relation between $\mathbf{j}$ and $\mathbf{E}$ can be expressed by Ohm's law:

$$\mathbf{j}(\mathbf{k}, \omega) = \boldsymbol{\sigma}(\mathbf{k}, \omega) \cdot \mathbf{E}(\mathbf{k}, \omega), \tag{3.5}$$

where $\boldsymbol{\sigma}$ is the conductivity of the plasma. In general for an anisotropic plasma, $\boldsymbol{\sigma}$ becomes the conductivity tensor, which will be discussed later.

Next, through the Fourier transform $\mathbf{E}(\mathbf{x}, t) \rightarrow \mathbf{E}(\mathbf{k}, \omega)$ ($\frac{\partial}{\partial t} \rightarrow -i\omega, \nabla \rightarrow ik\mathbf{e_x}$) and

linearization, (3.3) becomes:

$$\left(\mathbf{kk} - k^2\mathbf{I} + \frac{\omega^2}{c^2}\boldsymbol{\varepsilon}\right) \cdot \mathbf{E} = 0, \tag{3.6}$$

where $\mathbf{I}$ is the second-order unit tensor and $\boldsymbol{\varepsilon}$ the dielectric tensor of the plasma:

$$\boldsymbol{\varepsilon} = \mathbf{I} + \frac{i}{\omega\varepsilon_0}\boldsymbol{\sigma}. \tag{3.7}$$

The dielectric tensor is a more convenient quantity to describe the properties of the plasma than the conductivity.

Now (3.6) represents three homogeneous simultaneous equations for the three components of the electric fields $\mathbf{E}$. To have a nontrivial (nonzero) solution, the determinant of the matrix coefficients must be zero:

$$\det\left(\mathbf{kk} - k^2\mathbf{I} + \frac{\omega^2}{c^2}\boldsymbol{\varepsilon}\right) = 0. \tag{3.8}$$

This equation determines relations between the wavenumber $\mathbf{k}$ and the frequency ω for the different waves. The solutions $k = f(\omega)$, called the eigenvalues of the matrix equation, provide the *dispersion relation* of these waves. The solutions for $\mathbf{E}$, called the eigenvector, determines the polarization characteristics of these waves.

3.1.2 Refractive index

From the previous derivation we know that the particular properties of plasmas affect the wave propagation through the conductivity $\boldsymbol{\sigma}$ or the permittivity $\boldsymbol{\varepsilon}$. To calculate the plasma permittivity, the kinetic treatment by the Boltzmann equation considers the distribution function of particles in phase-space and thus provides a comprehensive plasma information. Here, we use the fluid treatment which considers only the zeroth moment of the Boltzmann equation, i.e. the density. The simplified fluid approach is adequate in our case when the waves travel at phase velocities close to the speed of light in plasmas whose electron thermal velocity is much less than the speed of light ($v_{th} \ll c$). When neglecting the particle thermal motion, the treatment is called the *cold plasma* approximation.

The equation of motion of a single electron in a plasma is:

$$m_e\frac{\partial \mathbf{v}}{\partial t} = -e(\mathbf{E} + \mathbf{v} \times \mathbf{B_0}), \tag{3.9}$$

here, an unperturbed magnetic field $\mathbf{B_0}$ is considered but collisions are ignored. In the cold plasma approximation the electrons move together and the current density becomes:

$$\mathbf{j} = -en_e\mathbf{v} = \boldsymbol{\sigma} \cdot \mathbf{E}. \tag{3.10}$$

For simplicity and without loss of generality, taking $\mathbf{B_0}$ in the direction of the z axis, the

conductivity tensor is obtained from the three components of (3.9) and (3.10):

$$\boldsymbol{\sigma} = \frac{in_e e^2}{m_e \omega} \cdot \frac{1}{1-\omega_{ce}^2/\omega^2} \begin{bmatrix} 1 & -i\omega_{ce}/\omega & 0 \\ \omega_{ce}/\omega & 1 & 0 \\ 0 & 0 & 1-\omega_{ce}^2/\omega^2 \end{bmatrix}. \tag{3.11}$$

Here, e, n_e and m_e are the electron charge, density and mass, respectively, while $\omega_{ce} = eB_0/m_e$ is the electron cyclotron frequency. This is only the electron conductivity, whereas the total conductivity has contributions from both electrons and ions. The same derivation and results are valid for the ions, except that one should use the ion charge, density and mass (Ze, n_i, m_i) in (3.11). Because $m_i \ll m_e$, the ion conductivity is negligible when compared to the electron contribution, as long as the wave frequency is sufficiently high. According to the definition (3.7), the dielectric tensor can be written as:

$$\boldsymbol{\varepsilon} = \begin{bmatrix} 1-\frac{\omega_{pe}^2}{\omega^2-\omega_{ce}^2} & \frac{i\omega_{pe}^2\omega_{ce}}{\omega(\omega^2-\omega_{ce}^2)} & 0 \\ \frac{-i\omega_{pe}^2\omega_{ce}}{\omega(\omega^2-\omega_{ce}^2)} & 1-\frac{\omega_{pe}^2}{\omega^2-\omega_{ce}^2} & 0 \\ 0 & 0 & 1-\frac{\omega_{pe}^2}{\omega^2} \end{bmatrix}, \tag{3.12}$$

where $\omega_{pe} = (n_e e^2/\varepsilon_0 m_e)^{1/2}$ is the electron plasma frequency.

For convenience, the following dimensionless physical quantities are defined:

$$X = \frac{\omega_{pe}^2}{\omega}, Y = \frac{\omega_{ce}}{\omega}, N = \frac{kc}{\omega}. \tag{3.13}$$

Then, substituting $\boldsymbol{\varepsilon}$ from (3.12) into (3.8), the determinant equation becomes:

$$\begin{vmatrix} -N^2+1-\frac{X}{1-Y^2} & \frac{iXY}{1-Y^2} & 0 \\ -\frac{iXY}{1-Y^2} & -N^2\cos^2\theta+1-\frac{X}{1-Y^2} & N^2\cos\theta\sin\theta \\ 0 & N^2\cos\theta\sin\theta & -N^2\sin^2\theta+1-X \end{vmatrix} = 0. \tag{3.14}$$

Here, θ is the angle between the wavenumber $\mathbf{k}$ and the magnetic field $\mathbf{B_0}$. The solutions are of the following form:

$$N^2 = 1 - \frac{X(1-X)}{1-X-\frac{1}{2}Y^2\sin^2\theta \pm [(\frac{1}{2}Y^2\sin^2\theta)^2+(1-X)^2Y^2\cos^2\theta]^{1/2}}. \tag{3.15}$$

This is called the *Appleton-Hartree formula* for the refractive index N. Two main situations exist, depending on the angle between $\mathbf{k}$ and $\mathbf{B_0}$:

- $\mathbf{k} \parallel \mathbf{B_0}$ ($\theta = 0$): the waves propagate parallel to the magnetic field and the solutions are
$$N^2 = 1 - \frac{X}{1-Y^2} \pm \frac{XY}{1-Y^2}. \tag{3.16}$$
Here, the waves are circularly polarized and '+' and '-' correspond to left- and right-handed electric field rotation, respectively.

- $\mathbf{k} \perp \mathbf{B_0}$ ($\theta = \pi/2$): the waves propagate perpendicular to the magnetic field with solutions
$$N^2 = 1 - X \tag{3.17}$$
and
$$N^2 = 1 - \frac{X(1-X)}{1-X-Y^2}. \tag{3.18}$$

3.1.3 Cut-off positions for O-mode and X-mode

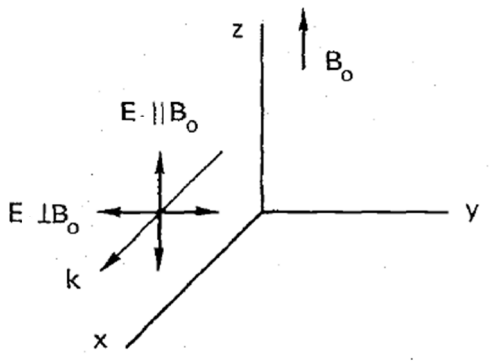

Figure 3.1: Polarization directions of O-mode ($\mathbf{E} \parallel \mathbf{B_0}$) and X-mode ($\mathbf{E} \perp \mathbf{B_0}$) propagation in the background magnetic field $\mathbf{B_0}$.

Considering the EM waves that propagate perpendicular to the toroidal magnetic field in tokamaks, this corresponds to the $\mathbf{k} \perp \mathbf{B_0}$ case with two polarization modes, as shown in figure 3.1:

- Ordinary mode (**O-mode**): the electric field of the waves is parallel to the background magnetic field $\mathbf{E} \parallel \mathbf{B_0}$. The dispersion relation can be rewritten from (3.17):
$$N_O^2 = \left(\frac{kc}{\omega}\right)^2 = 1 - \frac{\omega_{pe}^2}{\omega^2}, \tag{3.19}$$
indicating that the propagation of O-mode depends only on the electron density.

- Extraordinary mode (**X-mode**): the electric field of the waves is perpendicular to the background magnetic field $\mathbf{E} \perp \mathbf{B_0}$. The dispersion relation can be rewritten from (3.18):
$$N_X^2 = \left(\frac{kc}{\omega}\right)^2 = 1 - \frac{\omega_{pe}^2}{\omega^2}\frac{\omega^2 - \omega_{pe}^2}{\omega^2 - \omega_{pe}^2 - \omega_{ce}^2}, \tag{3.20}$$

indicating that the propagation of X-mode depends on both the electron density and the magnetic field.

From (3.19) and (3.20), the phenomenon called *cut-off* occurs when the refractive index becomes zero. At the cut-off position, the wave vector (wavenumber) k becomes zero with finite ω. The waves become evanescent behind the cut-off layer and are reflected backwards. The cut-off frequencies for O-mode and X-mode can be derived directly from setting (3.19) and (3.20) to zero.

From $N_O = 0$, the O-mode cut-off frequencies are obtained:

$$\omega_O = \omega_{pe}. \tag{3.21}$$

The cut-off density can be derived from (3.19):

$$n_c = \frac{\varepsilon_0 m_e (2\pi f)^2}{e^2}, \tag{3.22}$$

where ε_0 is the vacuum permittivity, e and m_e the electron charge and mass, and $f = \omega/2\pi$ is the frequency of the probing wave. The position corresponding to the density n_c is called the *cut-off layer*.

From $N_X = 0$, the X-mode cut-off frequencies include two branches:

$$\omega_U = \frac{1}{2}[\omega_{ce} + (\omega_{ce}^2 + 4\omega_{pe}^2)^{1/2}], \tag{3.23}$$

$$\omega_L = \frac{1}{2}[-\omega_{ce} + (\omega_{ce}^2 + 4\omega_{pe}^2)^{1/2}], \tag{3.24}$$

where ω_R and ω_L are called the upper and lower X-mode cut-offs.

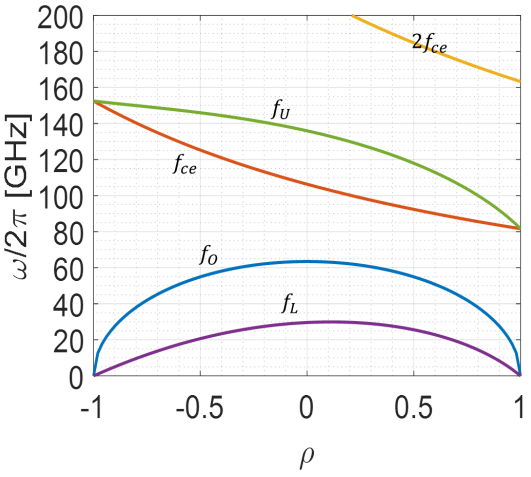

Figure 3.2: Characteristic plasma frequencies on the equatorial plane of Tore Supra plasmas. f_O, f_U and f_L represent the O-mode cut-off, upper X-mode and lower X-mode frequencies, respectively. f_{ce} is the electron cyclotron frequency. $\rho = rcos(\theta)/a$ is the normalized radial position in the poloidal cross-section, with a the plasma minor radius.

Figure 3.2 shows the radial profiles of O-mode, upper and lower X-mode cut-off frequencies in typical Tore Supra plasmas. The cut-off frequencies of the O-mode start from zero frequency in the edge and reaches the maximum value in the center, whereas the X-mode starts from finite frequency in the outer edge ($\rho = 1$) and its frequencies continuously increase towards the inner part of plasmas.

3.1.4 Resonance phenomenon

With the finite refractive index ($N > 0$), the electromagnetic waves can propagate through the plasmas. However, another important phenomenon called *resonance* could occur when the refractive index becomes infinite. For the case where $\mathbf{k} \perp \mathbf{B_0}$ (from (3.20)), a resonance occurs when satisfying:

$$\omega^2 = \omega_{pe}^2 + \omega_{ce}^2 = \omega_h^2, \tag{3.25}$$

where ω_h is called the upper hybrid frequency resonance condition. At a resonance, the wavelength goes to zero and the EM waves are generally absorbed by plasmas. In turn, the resonance has been used as a method to heat plasmas through transferring the energy of EM waves to plasmas, such as the application of ICRH, ECRH and LH heating scenarios. However, the resonance phenomenon should be avoided in applications relying on wave reflection.

3.2 Effects of fluctuations

After introducing the general principles of the propagation of EM waves in plasmas, this section focuses on the effects of fluctuations on the waves.

3.2.1 Bragg scattering

When fluctuations exist in the plasmas along the propagation path of the EM waves, the waves can be scattered by the fluctuations. The Bragg rule determines that the scattering process:

$$\mathbf{k_s} = \mathbf{k_i} + \mathbf{k_f}, \tag{3.26}$$

Here, $\mathbf{k_s}$ is the scattered wavenumber, $\mathbf{k_i}$ is the local wavenumber of the incident probing wave, and $\mathbf{k_f}$ is the wavenumber of the fluctuations, as shown in figure 3.3. The wavenumber of the density fluctuations is determined by the angle between $\mathbf{k_i}$ and $\mathbf{k_s}$: $k_f = 2k_i sin(\theta/2)$. Furthermore, since the scatter field E_s could be expressed as a spatial integral in terms of the density fluctuation level and Airy functions [Zou 1991, Fanack 1996], a finite value called the Airy wavenumber (k_A) determines the minimum fluctuation wavenumber that can be selected by the Bragg rule. Above the Airy wavenumber ($k_f > 2k_A$), the Bragg scattering dominates and the scattering could happen far from the Bragg resonant position. When $k_f < 2k_A$, the Bragg rule cannot be fulfilled and the

phase response is then localized in the cut-off layers and due to the fluctuation of the cut-off surfaces.

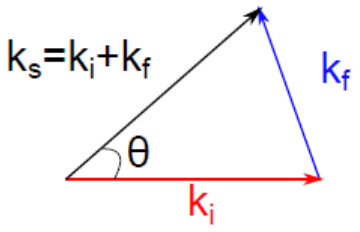

Figure 3.3: Illustration of the Bragg resonant rule in the scattering of EM waves due to the turbulent fluctuations.

3.2.2 Density fluctuation vs. phase shift

Although the Bragg rule gives the qualitative relations between the propagating EM waves, fluctuations and the scattered waves, The quantitative relation between the phase fluctuation of the EM waves and the fluctuation level is complicated. We consider the case of one-dimensional O-mode propagation. In the framework of the Born approximation, only the first order of fluctuations is considered. For a fluctuation wavenumber that is much smaller than the probing wavenumber $k_f \ll k_0$, the dominant effect is the cut-off oscillation when the fluctuations cross the cut-off layer. In other words, the phase response is localized at the cut-off, as shown in figure 3.4.

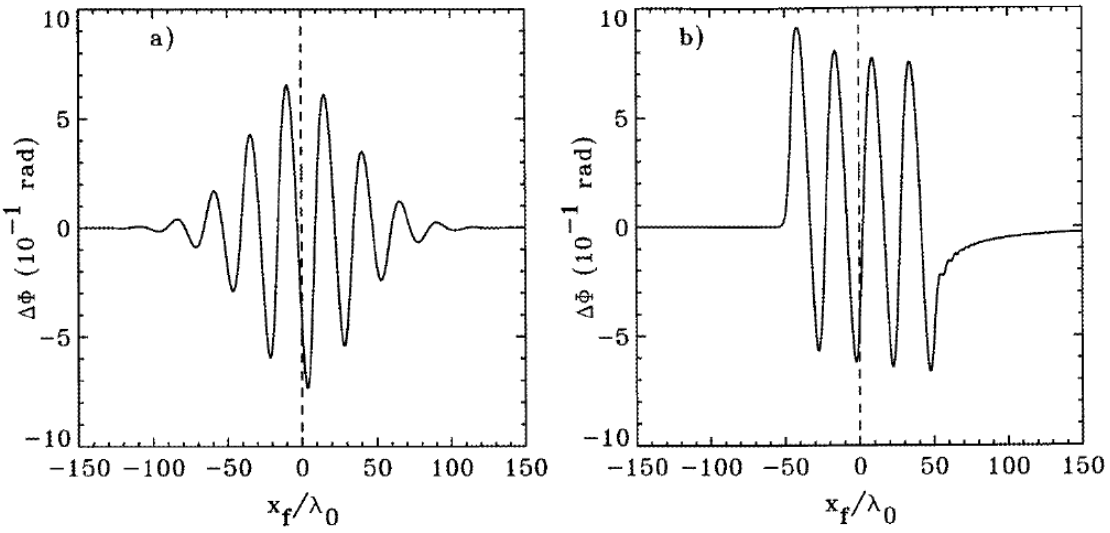

Figure 3.4: Phase response due to density fluctuations with (a) Gaussian and (b) square distribution shape. From [Fanack 1996].

In the edge region (far from the cut-off), the Bragg scattering is important and small-scale fluctuations dominate, whereas in the area near the cut-off, the reflection becomes

more important and large-scale fluctuations dominate. With the normal-incidence reflectometer, the motion of the cut-off is reflected by the phase fluctuations contained in the change of refraction index. Then, the density fluctuations can be linked with the phase fluctuation by [Mazzucato 1998]:

$$\frac{\delta n_e}{n_e} = \left(\frac{c^2}{4\pi^3}\frac{k_{\text{eff}}}{L_\varepsilon f^2}\right)^{1/2}\delta\phi. \tag{3.27}$$

Here, $L_\varepsilon = (\partial\varepsilon/\partial r)^{-1}$ is the scale length of the permittivity ε at the cutoff position, while f is the frequency of the probing wave. k_{eff} is the effective (or averaged) wavenumber. The situation for the X-mode is more complicated because of its dependence on the magnetic field. The details of the phas change for X-mode can be found in [Colin 2001]. A drastically simplified expression for X-mode is obtained be adding a factor 2 on the rhs of (3.27) [Mazzucato 1998, Colin 2001]. However, a phenomenon called 'phase runaway' is usually observed in the phase fluctuation signals, making it difficult to extract the phase fluctuation level and establish the link to the density fluctuation [Ejiri 1997]. In this case, the phase delay continuously increases with time in a way that can not represent a continuous motion of the cut-off positions with respect to the receiver.

3.2.3 Additional effects on wave propagations

Only the one-dimensional linear and ideal cases of reflectometry measurement have been presented. In real experiments, the situation is more complex due to nonlinear effects [Gusakov 2002] induced by high turbulence levels in the edge plasma and due to phase screening [Mazzucato 1991]. In a one-dimensinoal Born approximation, a slow decay of coherence with increasing frequency difference of the reflectometry signals is predicted, but a quick decay of coherence is observed in the experiments. Here, the small angle multi-scattering may be the main nonlinear effect. In the phase screen model, the entire propagation region in the plasma is compressed into a thin screen, such that the fluctuation of the cut-off positions can be related to the phase integral of geometric optics. However, fluctuations also occur in the poloidal direction in a two-dimensional view. This 2-D fluctuation picture has been applied in imaging reflectometry [Muscatello 2014, Wang 2017].

3.3 Reflectometry principles

Radar techniques have been used to measure electron densities in the ionospheric plasma. The position of the cut-off layers is determined from the time delay of the reflected pulse with respect to the transmitted part.

A similar technique has been use for Reflectometry which operates by launching electromagnetic waves with frequency f towards a plasmas whose density increases monotonically in the direction of the wave propagation. When the waves reach the cut-off layer ($n_e = n_c$), they are reflected back along the propagation direction. The plasma density

and density fluctuation information in the cut-off region can then be obtained through measurement of the reflected waves. By rapidly scanning the frequency of the wave, a range of radial positions can be probed.

3.3.1 Phase detection

Figure 3.5 shows the schematic principles of microwave reflectometry. The microwaves are launched towards the plasma using antennas beyond the plasma edge. The microwaves are reflected back at the cut-off layers and detected by antennas (same or different antennas can be used for emission and reception). The phase differences carry the information on the position of the cut-off layers. In contrast to a regular radar application, the phase differences depend not only on the spatial distance between the emitting and receiving antennas but also on the plasma refractive index along the propagation path.

Considering the WKB (geometrical optics) approximation, which assumes that the properties of the plasma vary slowly and thus locally the waves can be considered as propagating in an approximately uniform medium. The phase change of a microwave beam with frequency f in plasmas is given by the integral of the refractive index along the propagation path:

$$\phi = \int \frac{2\pi f}{c} N \mathrm{d}x, \tag{3.28}$$

with c the speed of light. In other words, the gradient of the refractive index is small compared to the wavelength ($|\nabla k|/k^2 \ll 1$).

Near the cut-off position, the WKB approximation may break down as k approaches zero. However, a more rigorous approach (full-wave treatment) shows that, when assuming a linear density increase near the cut-off position, for O-mode reflectometry, the phase change due to the plasmas is:

$$\phi(f) = \frac{4\pi f}{c} \int_{r_1}^{r_c} N(r) \mathrm{d}x - \frac{\pi}{2}. \tag{3.29}$$

Here, r_1 is the plasma edge and r_c is the cut-off position, while an additional $\pi/2$ phase change at reflection should be included.

3.3.2 Profile reconstruction

To reconstruct the density profile, one needs to be able to localise the position of the cut-off layer along the density profile. This can be achieved by directly measuring the time delay $\tau(f)$ at different frequency (f) or measuring the phase $\phi(f)$. The direct method has been realized by the so-called pulsed-radar reflectometry [Donné 1997], relying on the same principles as a conventional radar. The indirect method measures $\phi(f)$ when scanning the frequency f, and the time delay $\tau(f)$ can be obtained through the change rate of ϕ w.r.t. f:

$$\tau(f) = \frac{1}{2\pi} \frac{\mathrm{d}\phi(f)}{\mathrm{d}f}. \tag{3.30}$$

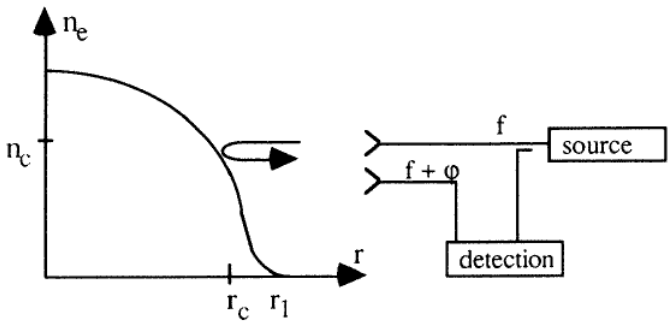

Figure 3.5: Schematic principles of microwave reflectometry. r_1 is the position of the plasma edge and r_c is the position of the cut-off layer for the corresponding frequency f. n_c is the corresponding cut-off density. Adapted from [Laviron 1996].

For the O-mode, the density profile can then be calculated by an Abel inversion integral:

$$r_c(f_c) = \frac{c}{\pi} \int_0^{f_c} \tau(f) \frac{\mathrm{d}f}{\sqrt{f_c^2 - f^2}}. \tag{3.31}$$

For the X-mode, the integral equation (3.29) must be inverted to give the density profile only if the profile of the magnetic field is know. In that case, the profile inversion should be performed by more complex numerical procedures [Bottollier-Curtet 1987, Morales 2018].

3.3.3 Fluctuation measurements

Except for the density profile, another measurement capability of reflectometry is the density fluctuations. Several different forms of reflectometry have been developed to acquire local turbulence properties at the cut-off positions. The fixed-frequency reflectometry is the standard diagnostic, where the density fluctuations are reflected by the oscillations of the cut-off layers. The density fluctuation can be induced from the measurements of phase difference. Instead of using a fixed frequency, one could scan the cut-off frequencies with a fast rate (GHz), and turbulence can be regarded as being 'frozen' during the fast scanning period [Clairet 2010]. By this technique, called the fast-sweeping reflectometer, the fluctuations in a large spatial range can be detected simultaneously. The fast-sweeping reflectometer can also measure the radial correlation length [Hornung 2013b]. Another technique using multiple receiving antennas in separate poloidal angles is called the poloidal correlation reflectometer (PCR), which can provide estimates of the turbulence correlation length and time by correlating the signals from different antennas [Krämer-Flecken 2010]. The Doppler backscattering (DBS) reflectometer detects the scattered wave rather than the reflected waves by tilting the probing beam so that the wave vector ($\mathbf{k}$) is no longer perpendicular to the reflection surface. The scattering position (and the wavenumber k) then depends on the tilting angle, making it possible to measure the k-spectra at various positions. In addition, DBS can also measure the perpendicular rotation.

3.3.4 Constraints of measurements

Many factors can affect accurate phase measurements and interpretation of the signals. First, the beam width of the reflected wave could becomes wider due to scattering in the plasma edge (higher fluctuation level) or misalignment of the optical path. Moreover, ECE emission affects the microwave signals in reflectometry, because when the microwave frequency is close to the electron cyclotron frequency ω_{ce} or one of its harmonics, radiation absorption can happen. If the wave passes through an absorption region before reaching the cut-off layer, measurement of the reflected wave becomes infeasible. ECE signals can also increase the noise of the reflectometry signals. Another factor increasing noise is related to suprathermal or runaway electrons [Sabot 2006a], which may be driven in LH plasmas.

3.4 Tore Supra core reflectometer set-up

The X-mode reflectometer on Tore Supra includes the core reflectometer (D-band, 105-150 GHz) [Sabot 2006b] and edge reflectometer (V-band, 50-75 GHz and W-band, 75-110 GHz) [Clairet 2010], covering the complete radial range in the equatorial plane. Both reflectometers can perform frequency sweeps to reconstruct a density profile. The core reflectometer also used a fixed-frequency mode, dedicated to diagnose core density fluctuations with high signal-to-noise ratio (SNR). For the systematic study in this thesis, we focus on the core reflectometer.

3.4.1 Experimental set-up

The core reflectometer operated from 2002 to 2011, located on the equatorial plane with bi-static antennas (separate antennas for emission and reception of the probing wave). Low-divergence (half power half width (HPHW) $\sim 1°$) antennas (bi-static setup) produced an almost parallel beam spot about 3.5 cm in radius [Sabot 2006b]. It was designed to probe the complete core region from mid-radius at the LFS to the HFS at high magnetic field (3.5 $\sim$ 3.8 T). At lower-magnetic fields (3 $\sim$ 3.5 T), measurements were strongly restricted in their radial positions, with limited accessibility to the LFS.

Figure 3.6 illustrates the simplified electronic circuit and optical systems of the core reflectometer. The microwave source includes a frequency synthesizer for fluctuation measurements and a VCO (Voltage Control Oscillator) for profile measurements. Frequency multipliers (8 or 9 order) increase the frequency to the D-band in both probing and reference arm. A single sideband modulator on the probing arm shifts the probing frequency for heterodyne detection [Sabot 2004]. With heterodyne I/Q detection, the acquisition sampling frequencies are 1 MHz and 100 MHz for the fluctuation and profile measurements, respectively.

For the profile measurements, 1000 density profiles were usually measured throughout the discharge outside the acquisition windows used for fixed-frequency fluctuation measurements. The profiles were measured in 40 – 100 μs. Burst profile measurements

(5 μs dwell time between consecutive sweeps) were also performed to follow fast density evolutions such as due to sawteeth [Sabot 2016].

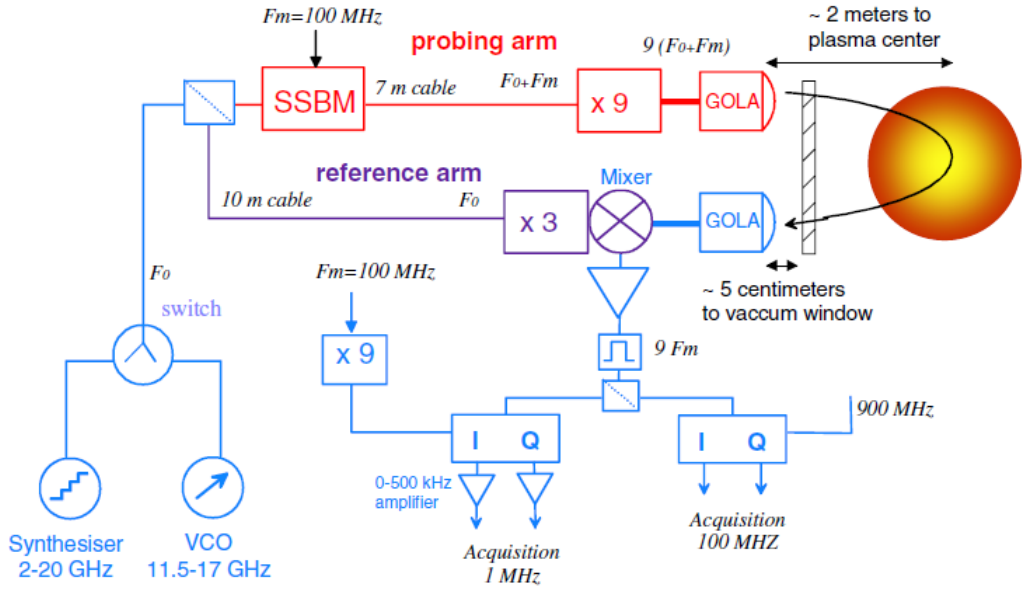

Figure 3.6: Set-up of the main channels of the core fluctuation reflectometer system on Tore Supra. Important components: single sideband modulator (SSBM), Gaussian optics lens antenna (GOLA), multiplier (x9), demodulation (I/Q). Adapted from [Sabot 2006b].

For the fluctuation measurements, a calibrated I/Q detection measures the two orthogonal homodyne signals $A\cos\phi$ and $A\sin\phi$, with A and ϕ the amplitude and phase of the fluctuation signals. Then, a complex signal is obtained:

$$s(t) = A\cos\phi + i\cdot\sin\phi = e^{i\phi}, \tag{3.32}$$

where $A = A(t)$ and $\phi = \phi(t)$. The reflectometer usually probes 20 fixed frequency steps of 10 milliseconds several times per shot. Figures 3.7 (a–d) show the evolution of different signals by one typical example of the acquisition during one step. Fluctuation measurements were performed in less than 300 ms, usually during a stable phase of the discharge. Longer acquisition (500 ms) at 1 up to 4 frequency steps could also be performed for MHD studies [Amador 2018]. In this study, only the data from the density fluctuation measurements are analyzed.

Thanks to the dual-source system [Sabot 2006b], this reflectometer can measure in the same plasma pulse the density fluctuations at fixed frequencies and the density profiles. However, the density profile and fluctuation could not be obtained at the same time.

3.4.2 Power spectra from fluctuation signals

Since the heterodyne complex contains both amplitude and phase information, we choose the complex signal to apply the FFT algorithm. In carrying out FFT, the number of frequency bins was set to 1024 in order to obtain good resolution at low frequency. The

Welch method [Welch 1967] was used to calculate the spectra with a Hamming window and 50% overlap to reduce sidelobes. Each frequency spectrum was then obtained by averaging over about 20 spectra. Figure 3.7 (e) is the corresponding power spectrum obtained through the FFT of the complex signal.

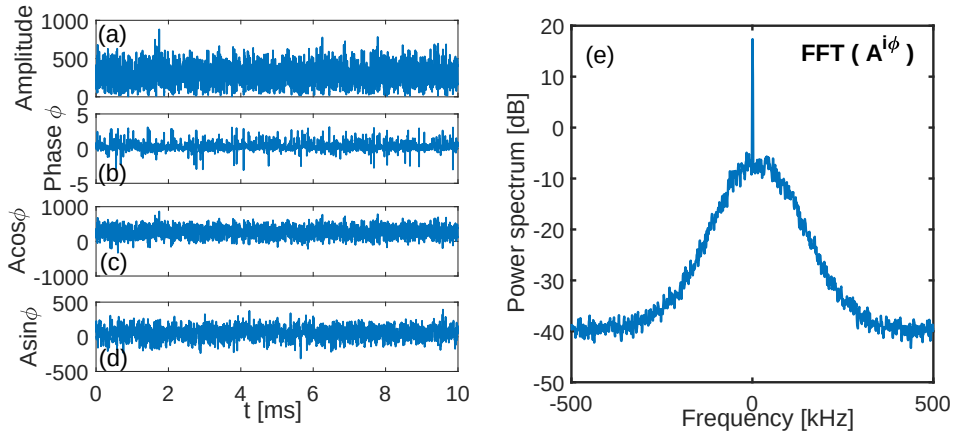

Figure 3.7: Raw fluctuation signals of (a) amplitude, (b) phase, (c) $Acos\phi$ and (d) $Asin\phi$ and (e) the corresponding power from the complex signal by the FFT algorithm, where the Welch method was used with Hamming window width 1024 and an overlap of 50%.

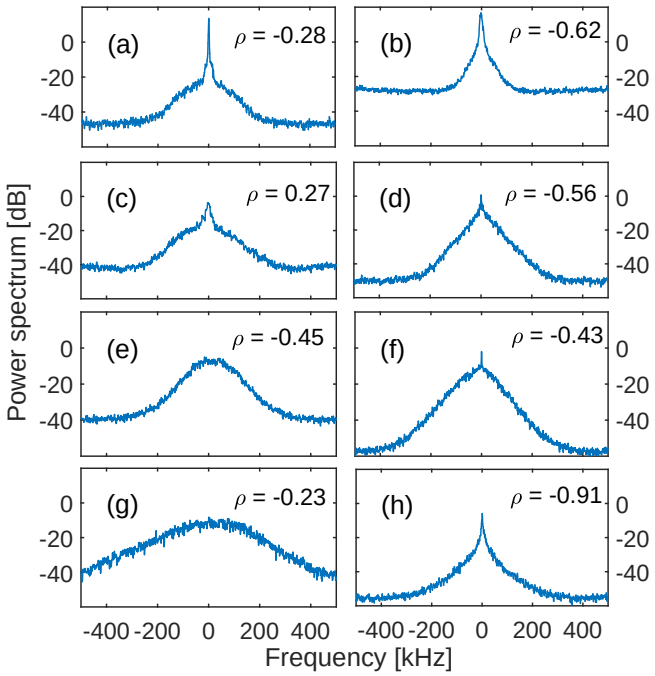

Figure 3.8: Some typical frequency spectra obtained from the core reflectometer database, with 1024 frequency bins. The normalized radial position (ρ) of the cutoff layer was calculated from a density profile obtained by the interferometry diagnostic. Negative ρ indicates HFS radial position.

Furthermore, figure 3.8 shows several other typical frequency spectra obtained from fluctuation measurements using this reflectometry setup, under different conditions and at varying radial positions. The spectra $S(f)$ (f is frequency) are plotted on a logarithmic scale ($10 \times log_{10}(S)$ in units of decibel (dB)). Although not all possible shapes of the complicated and varying frequency spectra in Tore Supra plasmas are shown, the examples in figure 3.8 do represent the typical spectral shape features encountered throughout the database. Positive and negative frequencies correspond to different directions of turbulence structure, respectively. The spectrum can be almost symmetrical, but sometimes the asymmetry is strong. This can be due to various reasons, like Doppler shift, small displacements of the plasma with respect to the equatorial plane, or asymmetries of the turbulent structures or in the wave propagation. As shown in figure 3.8, the fluctuation frequency spectra can be Gaussian-like (spectra (e) and (g)) or much more Lorentzian-like (spectrum (h)), i.e. strongly peaked with heavy tails. Other spectrum shapes are in between these typical spectra. The low-frequency component can be intense (spectra (a) and (b)), invisible (spectra (e) and (g)), or mixed with other parts of the spectrum (spectra (d) and (h)).

From reflectometry fluctuation power spectra, each spectrum has 1024 frequencies or parameters which is too much for a systematic study. Therefore, we follow a parametric approach to characterize the spectra by means of only a few parameters, i.e. a reduction from 10^3 to ca. 10 parameters. This is the basic motivation for the parametrization method discussed in the next chapter.

Chapter 4

Parametrization of fluctuation power spectra

Contents

A key ingredient of our systematic study of plasma turbulence properties from fixed-frequency reflectometry power spectra, is the spectrum parametrization method. The method was developed in the course of this work and is the subject of the present chapter. The motivation for parameter reduction is given in section 4.1. Section 4.2 discusses several aspects of the spectrum fitting method, viz. the spectrum normalization, the cost function and the parametric model. Section 4.3 provides the details of the fitting process, including boundary conditions for the parameters and global optimization. Some parametrization results and comparisons between different models are discussed in section 4.4. Finally, the parametrization method is applied to the Tore Supra database and a new turbulence database is built, as described in section 4.5.

4.1 Parameter reduction

Although manually investigating individual spectra by quantifying their properties (e.g. contribution, width and shape of different components) on a case-by-case basis is possible, systematic and standardized investigation of numerous spectra with complicated shapes requires automated methods. One of the key elements in this approach is a suitable representation of the spectra, which ideally should be interpretable in terms of the various components known to contribute to a reflectometer spectrum, in turn related to the underlying physics of plasma fluctuations. Considering the great variety of spectrum shapes (figure 3.8), acquired under widely varying plasma conditions, this is a rather ambitious goal. As described below, there are various criteria that a good spectrum representation should fulfill, but one of the most important is that it should be concise, i.e. using a limited set of parameters. Not only does this provide the best guarantee for maintaining physical interpretability, but it is also essential for the main goal of this work, i.e. to detect patterns in the spectra throughout a large database. Again with a view to physical interpretation, the best chance to detect important clusters or trends in the database is by relying on a succinct parametrization.

There are many ways to represent the frequency spectra (each spectrum has 1000 values) by fewer parameters. We decided on an approach wherein the spectrum is decomposed in several components, with every component characterized by only a few parameters. Although spectrum fitting techniques have been widely used in many research fields, such as chemical material analysis [Yamashita 2008], biology sample analysis [Lieber 2003], or spectroscopic applications in fusion plasmas [Nocente 2013], the situation in turbulence study is different. Indeed, while in regular spectrum fitting for routine applications the possible contributions to the spectrum are usually known beforehand, the composition of reflectometry spectra is much less clear. The occurrence of significant noise and unavoidable outliers further complicates the situation.

4.2 Spectrum fitting

4.2.1 Fitting criteria

While the total number of parameters describing the spectra, K should be limited for systematic studies and also to avoid overfitting, we still wish to cover all spectrum shapes observed in the database. Hence a moderate K should be aimed for. Further criteria for evaluating the fit quality are:

- *flexibility*: Flexibility refers to the ability of the model to represent many different spectral shapes, as seen in figure 3.8.
- *discrimination*: Discrimination is related to the distinguishing power of the model parameters w.r.t. the different spectral shapes, in the sense that the parameters should have moderate sensitivity to the spectral shape. Concretely, low sensitivity generates the same parameter results for all the cases, while high sensitivity leads to unstable parameters.

- *robustness*: Robustness means that the parameters should have minimal dependence on small model deviations that are of little interest to the analysis, such as noise.

4.2.2 Normalization and cost function

From figure 3.8 it is clear that the power of the reflected signal can vary significantly (several orders of magnitude) from one spectrum to another, which can be attributed to multiple reasons. Specifically, the launched microwave power and the wire conversion losses change with wave frequency and the reflected microwave power decreases with deeper penetration. However, the absolute value of each parametric spectrum component should be comparable across spectra to allow systematic investigations. Therefore, *normalization* of the power spectrum is required and here the spectrum $S(f)$ is normalized to the total integrated power of the spectrum:

$$\hat{S}(f) = \frac{S(f)}{\int_{f_{min}}^{f_{max}} S(f)\,\mathrm{d}f}. \tag{4.1}$$

Here, f_{min} and f_{max} denote the minimum and maximum frequency in the spectrum, which here we fix at $f_{min} = -500$ kHz and $f_{max} = 500$ kHz (because of the 1 MHz acquisition rate). As a result, the normalized spectrum integrates to unity, allowing spectra to be compared conveniently. For simplicity, in the remainder of this thesis, the normalized spectrum is also denoted by $S(f)$. All spectra used in this study were normalized in this way before parametrization as well as the subsequent detailed analysis.

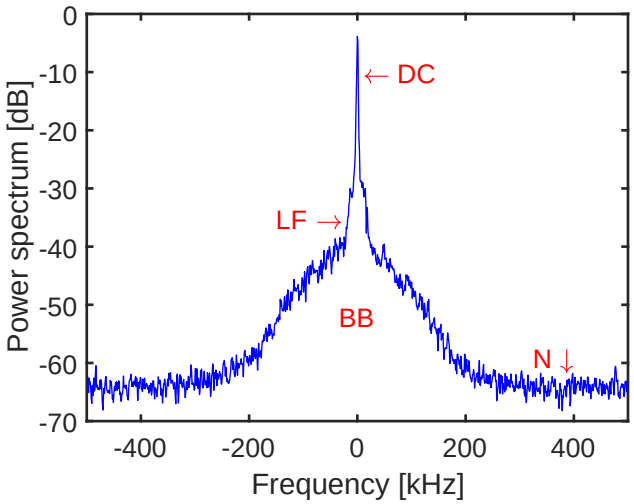

Figure 4.1: One typical normalized spectrum (figure 3.8 (a)) with the various components to be fitted. The spectrum has been normalized to its total power.

Figure 4.1 shows a typical normalized spectrum (corresponding to figure 3.8 (a)), with the various components indicated. When fitting a spectrum by minimization of the residual sum of squares (RSS), it is important to consider the scale at which to perform

the fit. Generally, the logarithmic scale gives more weight to low amplitudes while the linear scale gives more weight to high amplitudes. Specifically for the spectra analyzed here, low amplitudes are usually found at high frequencies and vice verse. For this reason a combination of fitting on both the logarithmic and linear scales is performed, by minimizing the following cost function:

$$F_{cost} = (1 - w) \times \frac{|\lg(S_{fit}) - \lg(S)|^2}{A_{lg}} + w \times |S_{fit} - S|^2. \tag{4.2}$$

Here, $S_{fit} = S_{fit}(f)$ and $S = S(f)$ denote the fitting model and the normalized frequency spectrum, respectively. In addition, $A_{lg} = \int_{Fmin}^{Fmax} (lg(S))^2 \, \mathrm{d}f$, where $lg = 10 \times log10$, is the integral of the spectrum on the logarithmic scale, ensuring normalization of the logarithmic part of the cost function. As a result, it is possible to weigh the two parts of the cost function using a weight factor w, allowing a more proper fit of both the high-frequency and low-frequency parts of $S(f)$.

In this study, we have chosen to give equal weight to the linear and logarithmic parts ($w = 0.5$) after comparing different values with some representative spectra. Experimentation with other values (0.25 and 0.75) has pointed out that the results are not very sensitive to the weight factor. This does not exclude a more optimal weight factor for different spectrum decompositions or different databases. In fact, the changeable weight of the cost function has the advantage of flexibility when comparing to some other methods to realize the optimisation like the Kullback - Leibler divergence.

4.2.3 Spectrum decomposition

In previous work [Krämer-Flecken 2004, Vershkov 2005, Shelukhin 2006, Vershkov 2011, Krämer-Flecken 2015], several components were distinguished in fluctuation spectra associated to specific physical phenomena: the direct current (DC) component [Krämer-Flecken 2015], the low-frequency (LF) fluctuations [Vershkov 2011], the broadband (BB) fluctuations and in some cases the quasi-coherent (QC) oscillations [Shelukhin 2006]. The BB fluctuations, which cover the whole frequency range, have a short correlation length [Krämer-Flecken 2015, Vershkov 2011] and have been attributed to turbulence, to be called BB turbulence [Vershkov 2005] hereafter. Both the LF and QC components are superimposed on the BB turbulence. The LF component represents the more intense fluctuations at low frequencies. Zonal flows and certain MHD modes like sawteeth and fishbones may contribute to this component. However, at this stage, it is still difficult the exact origination of the LF component. Due to the narrow bandwidth, it is also difficult to further discriminate the more refined different contributions. In addition, a very narrow central spike at zero frequency was identified as the reflectometer carrier wave, named the DC component in [Krämer-Flecken 2015]. The QC oscillations can be observed in the LFS and are linked to drift wave instabilities (TEM) [Arnichand 2014]. In addition, the noise (N) level should be considered as another component for completeness.

The central idea of this decomposition is that, under the condition that the decomposition provides a faithful representation of the various spectrum components, and assuming

that the main contribution to the density fluctuations originates from the vicinity of the cutoff layer, systematic studies of the underlying physical phenomena and their coupling should become feasible.

As mentioned before, to enable systematic studies of trends or evolution of turbulence properties, it is important to describe the spectrum components using a limited number of parameters. This is accomplished by modeling each component by a simple parameterized function, which is able to represent the shape of the component under different physical conditions. Thus, the objective is to fit the frequency spectrum by a model $S_{fit}(f)$, written as a sum of m components $C_i(f)$ $(i = 1, \ldots, m)$.

Apart from the components mentioned above, various low-frequency MHD modes (e.g. sawteeth [Chapman 2011], fishbones [Zonca 2007, Arnichand 2016], tearing modes [Buttery 2000]) and other high-frequency fluctuations (e.g. geodesic acoustic modes [Conway 2005, Zarzoso 2018], Alfvén eigenmodes [Heidbrink 2006, Fredrickson 2018, Crocker 2018]) could appear under certain conditions. Since the bandwidth of these fluctuations is relatively narrow the contribution to the total power can safely be neglected, even though their amplitudes can be large in some cases. Specifically, the bandwidth of these modes is only $10 \sim 100$ Hz (sawteeth) or a few or tens of kHz (fishbones, tearing modes, etc), which is usually some orders less than the bandwidth of the BB component (~ 100 kHz). The fitting results are therefore not expected to be substantially influenced in the presence of such modes. On the other hand, QC oscillations can attain significant bandwidths (tens of kHz). Low-frequency and high-frequency QC modes have been observed and examples can be found in [Krämer-Flecken 2004, Vershkov 2005, Shelukhin 2006, Vershkov 2011, Arnichand 2014]. However, we did not consider QC modes in the present stage, as their contribution to the power on the logarithmic scale is limited anyway.

In summary, every spectrum is decomposed into four basic components: the direct current (DC) component, the low-frequency (LF) fluctuations, the broadband (BB) turbulence and the noise (N) level, as shown in figure 4.1. Therefore the number of components m is 4 [Sun 2017]:

$$S_{fit} = C_{\mathrm{DC}} + C_{\mathrm{LF}} + C_{\mathrm{BB}} + C_{\mathrm{N}}. \tag{4.3}$$

4.2.4 Components of spectrum fit

We now go into more details for each of the main spectrum components.

4.2.4.1 The noise level

The level of noise, assumed to be frequency-independent white noise, can be described by a single constant, therefore

$$C_{\mathrm{N}} = \varepsilon_{\mathrm{N}}(f). \tag{4.4}$$

The noise level is also helpful to identify trivial spectra with low signal-to-noise ratio. In this study, the signal-to-noise ratio (SNR) is defined as the ratio between the maximum

value of the BB component and the noise level.

4.2.4.2 The low-frequency components

The low-frequency components of the spectrum include the DC and LF components. For each component, we need at least three parameters to describe the intensity, the central position and the spectral shape. Inspired by the normalization to unity of the total spectrum, we choose various probability density functions (PDFs) to model each of the components. The Gaussian (normal) PDF is the most straightforward choice, which has been used before as a model to describe the DC and LF components of coherence spectra [Krämer-Flecken 2015]. In this case, the fitting functions for the DC and the LF components are:

$$C_i = A_i \exp\left[-\frac{1}{2}\left(\frac{f-\mu_i}{\sigma_i}\right)^2\right], \tag{4.5}$$

where i denotes DC or LF. The amplitude A_i, the mean value μ_i and the standard deviation σ_i describe the intensity, central position and width of the components, respectively. For more accurate fitting of the DC component, the zero frequency is placed at the center of the spectrum by using 1025 rather than 1024 frequency bins.

4.2.4.3 The broadband (BB) turbulence

During initial attempts, the Gaussian function was also considered for the BB turbulence, but it was found insufficiently flexible to model all shapes. Indeed, the shape of the broadband can be distinctly non-Gaussian, more specifically Lorentzian (also known as Cauchy distribution) or Laplacian, with a strong peak and heavy tails, especially at the HFS. A combination of several Gaussian functions were tried as well, but that often caused the LF component to fit part of the BB and moreover the BB component could not reflect the real shape of the spectrum, as shown in figure 4.2. Therefore, a more flexible function was required and the following three options were explored: *the generalized Gaussian* (GG) *function*, *the Voigt function* and *the Taylor function*. The expressions of the three models are presented below and their detailed properties can be found in Appendix A.

The generalized Gaussian model The BB turbulence using the generalized Gaussian function becomes

$$C_{\mathrm{BB}}^{\mathbf{GG}} = A_{\mathrm{BB}} \exp\left[-\left(\frac{|f-\mu_{\mathrm{BB}}|}{\alpha_{\mathrm{BB}}}\right)^{\beta_{\mathrm{BB}}}\right], \tag{4.6}$$

where the fixed exponent in the Gaussian is replaced by a shape parameter β_{BB}, and the standard deviation $\sigma_{\mathrm{BB}} = \sqrt{\alpha_{\mathrm{BB}}^2 \Gamma(3/\beta_{\mathrm{BB}})/\Gamma(1/\beta_{\mathrm{BB}})}$, describing the spectral width. This function can fit multiple shapes, like Gaussian ($\beta_{\mathrm{BB}} = 2$) and Laplacian ($\beta_{\mathrm{BB}} = 1$).

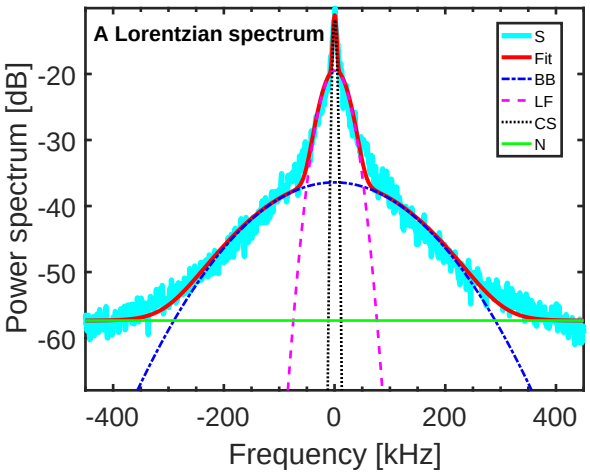

Figure 4.2: A typical Lorentzian spectrum in the database fitted by multiple Gaussian functions.

The Voigt model The Voigt function is a convolution of a Gaussian and a Lorentzian function:

$$C_{\mathrm{BB}}^{\mathbf{Voigt}} = A_{\mathrm{BB}} \int_{-\infty}^{+\infty} G(f;\sigma_{BBG}) L(\mu_{\mathrm{BB}} - f;\gamma_{BBL})\,\mathrm{d}f, \tag{4.7}$$

where $G(x;\sigma)$ and $L(x;\gamma)$ are the centered (zero-mean) Gaussian and Lorentzian function, respectively, while μ_{BB} encodes the central position of the BB component. The Voigt function has been widely used for fitting spectral lines [Thompson 1987, Ida 2000].

The Taylor model A third alternative model for the BB component is the Taylor function. It was used in [Hennequin 1999, Casati 2009] to express the correlation function of a turbulence signal in plasma physics:

$$F_{corr}(\Delta_{\mathrm{BB}}, \tau_{\mathrm{BB}}) = \exp\left[-\Delta_{\mathrm{BB}}(t - \tau_{\mathrm{BB}} + e^{-t/\tau_{\mathrm{BB}}})\right]. \tag{4.8}$$

Here, Δ_{BB} and τ_{BB} are related to the wavenumber, velocity and correlation time of the turbulence, while t is the sampling sequence, based on the theory of collective wave scattering by a non-uniform plasma [Grésillon 1992]. The corresponding fitting function is calculated through the Fourier transform of F_{corr}:

$$C_{\mathrm{BB}}^{\mathbf{Taylor}} = \mathrm{FFT}(F_{corr}). \tag{4.9}$$

The fitting function when considering the magnitude and the central shift can be found in Appendix A.

The number of parameters for the BB turbulence component is *four*, no matter which model is used. Together with the other three components, the complete fitting model S_{fit} has $K = 11$ parameters. Compared with the original 1024 (or 1025) frequency bins in the spectrum, the number of parameters has been reduced by two orders of magnitude.

This parameter reduction paves the way to systematic investigations of the spectrum properties, which would have been very difficult with a large number of parameters.

4.3 Fitting process

The spectrum fitting process is fundamentally a problem of nonlinear curve fitting or optimization. In the optimization approach, any constraints (boundary conditions) and the initial parameter values are two important factors affecting the fit.

4.3.1 Constraints on component parameters

In order to maintain correspondence between each of the functional forms presented before and the spectrum components that they are intended to fit, additional constraints on the component parameters are necessary. To force the DC component to fit the narrow carrier wave at zero frequency, we impose the constraints $|\mu_{\mathrm{DC}}| < 1$ kHz and $\sigma_{\mathrm{DC}} < 2.5$ kHz, as 1 kHz is the frequency resolution of the spectrum. For the LF fluctuations, which sometimes include high-amplitude, low-frequency MHD modes up to a few kHz, the constraints are $|\mu_{\mathrm{LF}}| < 10$ kHz and $\sigma_{\mathrm{LF}} < 20$ kHz. Furthermore, to avoid overlap between the DC and LF components, we require $\sigma_{\mathrm{LF}} > 1.5\,\sigma_{\mathrm{DC}}$ and $\sigma_{\mathrm{LF}} > 1$ kHz, where the factor 1.5 was determined empirically. To summarize, the constraints on the low-frequency part are:

$$\begin{aligned} &|\mu_{\mathrm{DC}}| < 1 \text{ kHz}, \quad |\mu_{\mathrm{LF}}| < 10 \text{ kHz}, \\ &\sigma_{\mathrm{DC}} < 2.5 \text{ kHz}, \quad 1 \text{ kHz} < \sigma_{\mathrm{LF}} < 20 \text{ kHz}, \\ &\sigma_{\mathrm{LF}} > 1.5\,\sigma_{CS}. \end{aligned} \tag{4.10}$$

Constraints on the amplitudes and noise are not necessary.

For the BB turbulence, the constraints depend on the fitting functions. With the generalized Gaussian model, to separate the BB and LF components the constraints $\sigma_{\mathrm{BB}} > 1.5\,\sigma_{\mathrm{LF}}$ and $\sigma_{\mathrm{BB}} > 10$ kHz are applied, where σ_{BB} is the standard deviation of the BB turbulence. In addition, to avoid an overly peaked BB fit, β_{BB} is assumed to be larger than 0.5, the generalized Gaussian function approximating a uniform distribution for large β_{BB} (in practice $\beta_{\mathrm{BB}} > 8$).

For the Voigt model, no limits have been put on the Lorentzian part. As for the Gaussian part, we use the same constraints as in the generalized Gaussian model for the standard deviation σ_{BB}.

The parameters of the Taylor model are more difficult to constrain, as the two parameters Δ_{BB} and τ_{BB} jointly affect the spectral shape. Here, we set $\Delta_{\mathrm{BB}} > 0.01$ and $\tau_{\mathrm{BB}} > 0.01$, to avoid unrealistically peaked shapes.

The constraints for the three models are summarized as follows:

- Generalized Gaussian model:
  $\sigma_{\mathrm{BB}} > 10$ kHz, $\sigma_{\mathrm{BB}} > 1.5\,\sigma_{\mathrm{LF}}$, $0.5 < \beta_{\mathrm{BB}} < 8$;

- Voigt model:
  $\sigma_{BBG} > 10$ kHz, $\sigma_{BBG} > 1.5\,\sigma_{\mathrm{LF}}$;
- Taylor model: $\Delta_{\mathrm{BB}} > 0.01$, $\tau_{\mathrm{BB}} > 0.01$.

4.3.2 Optimization of initial conditions

An interior-point algorithm was used for minimizing the cost function in (4.2). A more powerful global optimizer could be employed, but this turns out to be too time-consuming in practice for a database including 350,000 spectra. Therefore, multiple starting points were chosen based on various simple criteria, increasing the chance to converge to the global minimum by simply increasing the number of initial guesses N_{iv}, striking a balance between computational load and goodness-of-fit.

For the DC component, A_{DC}, μ_{DC}, and σ_{DC} were estimated by the maximum value of the spectrum, and its first and second central moments (standard deviation) in the frequency range $|f| < 3$ kHz, respectively. A similar approach was taken for the LF component, but within the frequency range 3 kHz $< |f| <$ 20 kHz to avoid influence by the strong DC component.

Likewise, for the BB component the parameters A_{BB} and μ_{BB} were estimated from the maximum and the first moment of the spectrum in the frequency range 20 kHz $< |f| <$ 300 kHz, to avoid influence of the low-frequency components. The initialization of the other parameters depends on the model.

The generalized Gaussian model For the generalized Gaussian function, σ_{BB} and β_{BB} were estimated from the second central moment (standard deviation) and standardized fourth moment (kurtosis), respectively. Multiple initial guesses were achieved by changing the starting β_{BB}.

The Voigt model When fitting the BB turbulence by the Voigt function, calculation of the error function is time-consuming. The pseudo-Voigt function provides an approximation of the Voigt by using a linear combination rather than a convolution of the Gaussian and Lorentzian functions (Appendix A). The same constraints as for the Voigt function were used. The second central moment of the spectrum gives the initial value of σ_{BBG} and multiple initial guesses of σ_{BBL} were obtained by varying η.

The Taylor model In the Taylor function, Δ_{BB} and τ_{BB} are slightly more difficult to estimate since they are not directly linked to the spectral shape. A tabulation of the standard deviation of $C_{\mathrm{BB}}^{\mathbf{Taylor}}$ in (4.8) in terms of Δ_{BB} was made for $\tau_{\mathrm{BB}} = 0.1$, allowing to derive initial estimates of Δ_{BB} from the second central moment of the spectrum. Multiple initial guesses were realized by varying τ_{BB}.

Furthermore, to determine the number of starting points N_{iv}, the generalized Gaussian model is taken as an example. The initial value of β_{BB} estimated from the kurtosis is denoted by β_{BB0} and was used as a first initial guess. Since $0.5 < \beta_{\mathrm{BB}} < 8$ and in

the database β_{BB} is typically between 1 and 2, the following initial values can cover the possible spectral shapes: $\beta_{BB0}/4$, $\beta_{BB0}/2$, $2\beta_{BB0}$, $4\beta_{BB0}$. For the second initial guess, the value of $\beta_{BB0}/4$ was used, because out of all other initial values it corresponds to the shape differing the most from the shape associated with the first guess β_{BB0} of β_{BB}. This principle was also used to choose the third, fourth and fifth initial guess, i.e. $4\beta_{BB0}$, $\beta_{BB0}/2$ and $2\beta_{BB0}$, respectively. The convergence performance was evaluated through the averaged relative error of the overall fit for 1000 random spectra from the database, for different N_{iv}. From figure 4.3, the relative error is near 10% for a single initial value and decreases rapidly when increasing N_{iv} before saturation at $N_{iv} = 3$. At this point the relative error drops to $\sim 1.8\%$, meaning that the results are very close to the global minimum.

For the Voigt model, $\eta = 0$ and $\eta = 1$ denote the Gaussian and Lorentzian shape, respectively. Therefore the first and second initial guesses were obtained by setting $\eta = 0$ and $\eta = 1$, followed by three more initial values in between these extremes: $\eta = 0.5$, 0.25, 0.75. The relative fitting error saturates at around 7% beyond $N_{iv} = 5$. As for the Taylor model, empirical evaluation revealed a typical value of $\tau_{\mathrm{BB}} = 0.1$. Therefore, we start from $\tau_{\mathrm{BB}} = 0.1$ and then alternately increase and decrease according to the sequence $\tau_{\mathrm{BB}} = 1$, 0.01, 0.5, 0.02. Again, the results remain almost the same for $N_{iv} > 5$, resulting in a fitting error of about 2%.

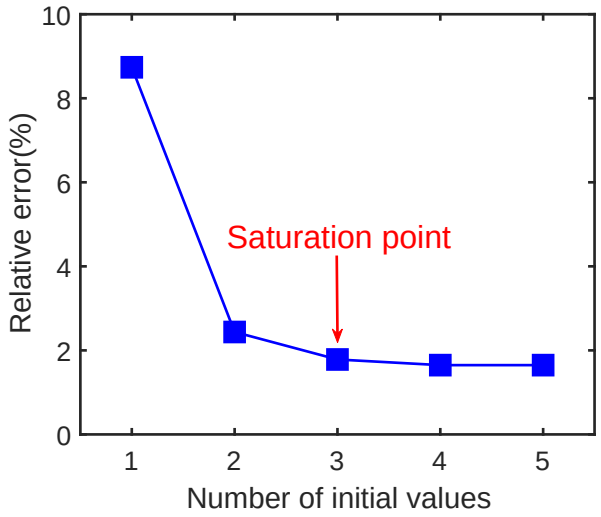

Figure 4.3: Relative error for the total fit, averaged over 1000 random spectra from the database, as a function of the number of initial values N_{iv} for β_{BB} in the GG model.

4.4 Parametrization results and discussion

4.4.1 Statistical comparison

To compare the fitting performance of the three models for the BB turbulence, the quality of the total fit was assessed for 10,000 spectra (about 3% of the full database). Here,

spectra with low SNR were not considered for the analysis even though the fitting results are good. The performance was evaluated by means of the minimal value of the cost function ($F_{cost,min}$) and the Bayesian information criterion (BIC). Assuming a Gaussian distribution of the measured spectrum around the fit, the BIC is given by [von der Linden 2014]:

$$BIC = 2n \times ln(s) + K \times ln(n). \tag{4.11}$$

Here, n is the number of data points, s is the standard deviation of the residuals, and K is the number of parameters of the overall model. The BIC includes a penalty term for overly complex models, hence avoiding a preference for models that overfit the data. Figure 4.4 shows the distribution of $F_{cost,min}$ and the BIC for all fits over the 10,000 spectra in the database. It can be seen that the generalized Gaussian and the Taylor model generally perform better than the Voigt (pseudo-Voigt) model. The generalized Gaussian model might still perform slightly better than the Taylor model.

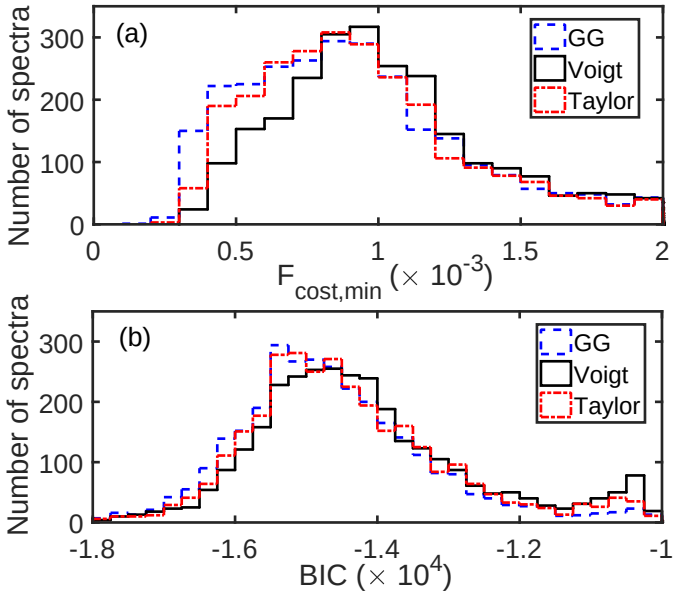

Figure 4.4: Comparison of (a) the minimal value of the cost function ($F_{cost,min}$) and (b) the Bayesian information criterion (BIC) for the generalized Gaussian (GG) function, the pseudo-Voigt function, and the Taylor function fitted to the BB turbulence component. The more a histogram contains low values of RSS and BIC, the better the performance of the corresponding model.

4.4.2 Representative spectral shapes

The statistical criteria studied above are only one aspect in assessing the fitted model. The fitting model should also conform to the criteria of flexibility, discrimination and robustness, and should be able to capture the salient physics reflected in the spectrum, especially the BB turbulence. In order to validate the superior performance of the generalized Gaussian and Taylor models, as suggested by the statistical analysis, some typical

examples were investigated in detail. When the BB component has a Gaussian-like shape, the three models all show an equivalent, excellent fitting performance. In contrast, in case of a more difficult to fit Lorentzian or Laplacian (i.e. double exponential, or triangular on the logarithmic scale), the fitting results can be very different between the three models. This is shown on both the linear and logarithmic scales in figures 4.5 and 4.6, which correspond to the approximate Lorentzian and Laplacian situation, respectively. On the linear scale, the fit is dominated by the low-frequency part ($f < 25$ kHz), while on the logarithmic scale validation of the fitting performance should concentrate on the larger frequencies (up to 450 kHz).

For the Lorentzian shape in figure 4.5, visual inspection reveals a good fit by all three models, although the fit including the pseudo-Voigt model underpredicts the spectrum between 5 and 10 kHz (figure 4.5 (c)) and around 100 kHz (figure 4.5 (d)). This is reflected by its slightly worse RSS and BIC compared to the other two models. Another shortcoming of the pseudo-Voigt model is that it tends to fit also the noise, as can be seen in figure 4.5 (d). Similar weaknesses of the pseudo-Voigt function can be seen in figure 4.6. For these reasons, we reject the Voigt function for fitting the BB turbulence.

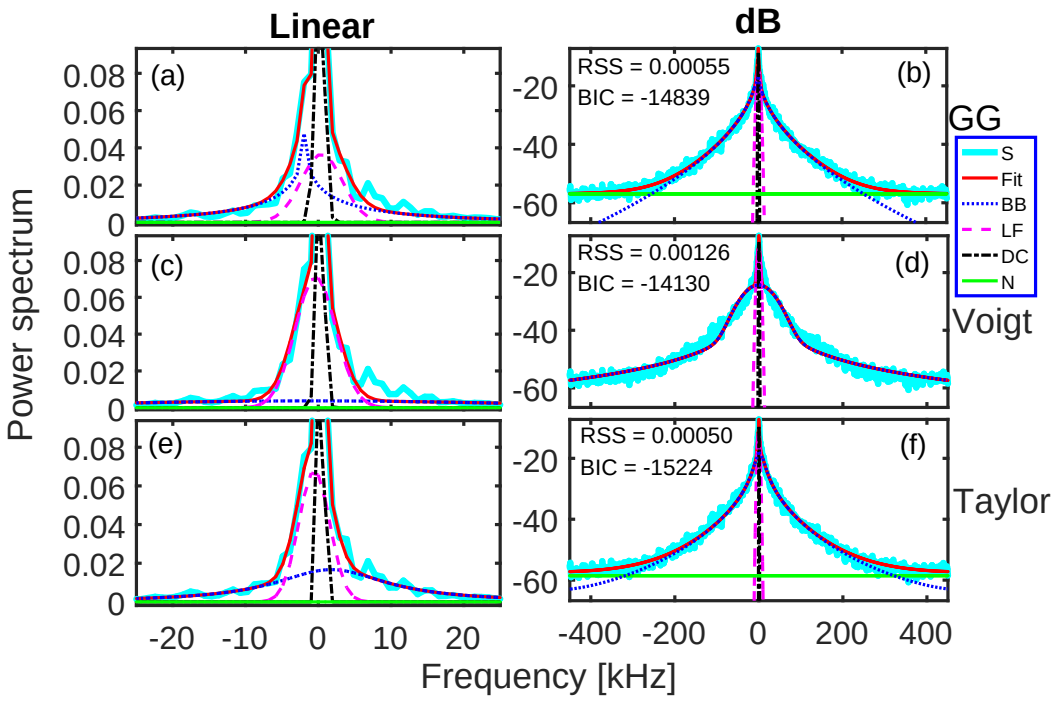

Figure 4.5: Fit of a Lorentzian spectrum (S), with the individual components also displayed. The BB component was fitted by a generalized Gaussian (GG) function ((a) and (b)), the pseudo-Voigt function ((c) and (d)), and the Taylor function ((e) and (f)). The results are shown on the linear scale ((a), (c), (e)) and logarithmic (dB) scale ((b), (d), (f)). The residual sum of squares (RSS) and the Bayesian information criterion (BIC) at the optimal solution by each model are also displayed.

When comparing the GG model with the Taylor model, it can be noted in figures 4.5 and 4.6 that the crucial difference is the peaked shape of the BB component in the GG

model, whereas the Taylor model has a much smoother shape. From poloidal correlation in [Krämer-Flecken 2015], the BB component disappears when the LF component remains the same, meaning that the BB component does not have an intense low-frequency part. Hence, the fitting results in terms of the BB and LF components can be very different. In figures 4.5 (a) and (e), the average frequencies w.r.t. the central frequency (0 KHz) for the BB and LF components have an opposite sign for the two models. Specifically, in figure 4.5 (a), the peaked shape of the GG seems to fit the knee in the spectrum around 3 kHz, whereas this shape is not expected for the BB turbulence. In the case of the Lorentzian or Laplacian spectra, we observe that the estimated GG shape parameter often saturates at the lower bound $\beta_{\mathrm{BB}} = 0.5$, causing a peaked shape that tries to fit small-scale features in the spectrum. In turn, this may lead to overestimation of the BB contribution and instability of the BB standard deviation. Therefore, due to both excellent quantitative and qualitative performance, we choose the Taylor model as the optimal fit to the spectra. Nevertheless, the generalized Gaussian model is still useful since it allows a more direct study of the shape of the BB component through a single shape parameter, whereas the two shape parameters of the Taylor model (Δ_{BB}, τ_{BB}) are more difficult to interpret.

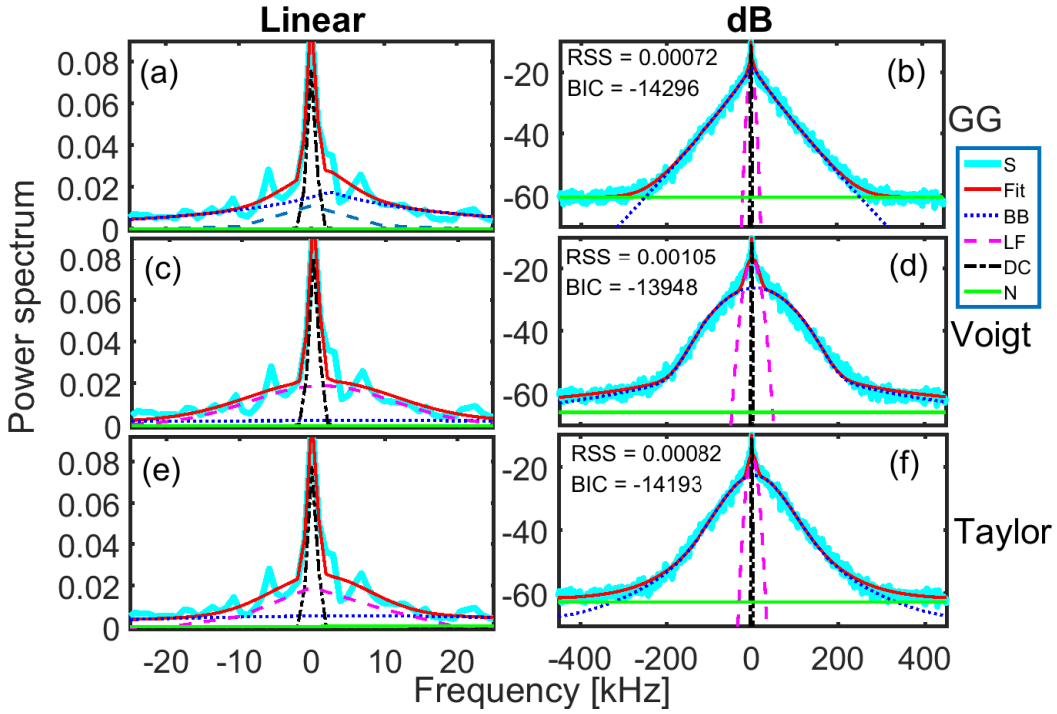

Figure 4.6: Same as figure 4.5 for a Laplacian shape.

The reliability of fitting different components of spectra relies on the number of data for the corresponding components, i.e., more data points give better fit. Although the number of FFT has been chosen as 1024 to guarantee an accurate estimation of the low frequency part, there is still relatively limited data points for the LF and DC components, while the BB component has sufficient points for the fit. Therefore, the fitting parameters/results should be more stable in the BB fit than the LF and DC components.

The parameters of the LF and DC components could become even less reliable when they saturate to the constrained maximum values. The situations occur especially when the integration or merging of the LF and BB component happens for some spectra shapes.

4.5 Turbulence database

The parametrization method was applied to core reflectometry measurements [Sabot 2006b] from 6,000 Tore Supra discharges carried out between 2002 and 2011, and a large-scale turbulence database was built including 350,000 reflectometer acquisitions. The 6,000 discharges contain a large number of Ohmically heated plasmas, as well as plasmas with auxiliary heating: ICRH, LH and a limited number with ECRH [Sun 2018].

4.5.1 Criteria of parameter filtering

An initial filtering of the database was deemed necessary, disregarding spectra with excessive noise or unwanted additional components, or in the presence of undesirable physical effects.

To quantify the noise level, the signal-to-noise ratio (SNR) is defined as the ratio between the amplitude of broadband component (A_{BB}) and the noise (ε_N): $\mathrm{SNR} = A_{\mathrm{BB}}/\varepsilon_N$. Spectra with too low SNR (< 25 dB) have been removed from the analysis. Such an example is shown in figure 4.7 (a). Moreover, spectra with large Doppler effect (central shift $\mu_{\mathrm{BB}} > 50$ kHz, e.g., figure 4.7 (b)) have also been excluded, since in these cases the physical process and the probed wavenumber are different from the standard reflectometry measurement signals. Specifically, the standard measurement signals come from the perpendicular reflection of the probing waves at the cutoff positions, and therefore reflect the local fluctuations with very low wavenumber. Large Doppler shift results from backscattering at finite wavenumber. This backscattering could appear when the magnetic axis is not on the equatorial plane, causing the reflectometer line-of-sight to be off-normal w.r.t. the cutoff layer surface, or when the turbulent structures are tilted with respect to the poloidal direction. Toward the edge, the tilting of the reflective surface in the toroidal direction due to the magnetic field ripple can also lead to strong Doppler shift. In addition, before further analysis, only measurements performed during steady-state conditions have been studied. For example, the reflectometer acquisitions during the current or power ramp-up or ramp-down phase have been filtered out to avoid additional complexity.

The present study considers the complete radial extent of the plasmas, except for the edge region at the LFS, where the density fluctuation level ($\delta n/n$) reaches $\sim 10\%$ and nonlinear effects may complicate the analysis [Sabot 2006a, Hornung 2013b]. Furthermore, spectra in the radial range at the LFS near the edge ($0.6 < \rho < 1$, with $\rho = r/a$ the normalized radius) are more prone to the large Doppler shift partly caused by the high ripple (6% at the plasma edge) of the magnetic field. Finally, this part of the plasma cannot be probed at low density due to the reflectometer frequency range. This condition occurs for low-density Ohmic discharges and most LH plasmas. For these reasons,

the number of valid measurements is significantly reduced beyond $\rho > 0.6$, rendering estimation of trends unreliable in that region. In practice, the radial range was set to $-1 < \rho < 0.6$. Here, $\rho = 0$ denotes the plasma center and negative ρ corresponds to the HFS.

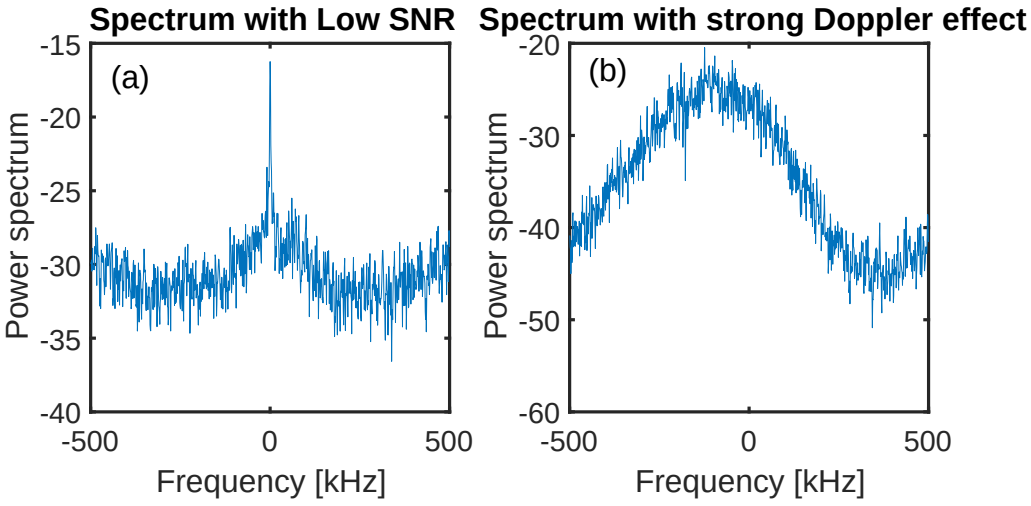

Figure 4.7: Representative spectrum with (a) low signal-to-noise ratio and (b) strong Doppler effect.

4.5.2 Parameters of the turbulence database

The database established in the framework of this PhD includes near 100 parameters that fall into four categories: the reflectometry diagnostic characteristics, the global operational parameters, the local plasma parameters and the spectrum characteristics.

The reflectometry diagnostic characteristics include acquisition parameters, as well as the probing frequencies ($100 \sim 155$ GHz) and the radius of the cutoff layer. The radius of the cutoff layer is recovered from the density profile obtained from an interferometry diagnostic [Gil 2009], as the density profile from the reflectometer is not available during fluctuation measurements. The normalized radius ρ of the cutoff layer ranges from -1 to 1, covering the entire plasma region.

Other global and local plasma parameters are obtained or calculated from various diagnostic data available in the Tore Supra database. The global operational parameters include the on-axis toroidal magnetic field $B_{t,0}$, plasma current I_p, line-integrated electron density n_l, major radius R, minor radius a, plasma heating power, elongation, edge safety factor (q_ψ) and the heating power for different scenarios (P_{Ohmic}, P_{ICRH}, P_{LH}, P_{ECRH}), etc. The local plasma parameters include the electron density $n_e(r)$ from interferometry measurements, the electron temperature $T_e(r)$ from ECE measurements, as well as the gradients of density, temperature and refractive index at the cutoff obtained from various density, temperature and magnetic diagnostics.

The spectrum characteristics initially include the 11 spectrum decomposition parameters. From these parameters, we derive the following additional quantities to systemat-

ically investigate general trends of the turbulence properties across the database. First, the BB contribution (E_{BB}) of the frequency spectrum in each spectrum is calculated by integrating the BB component, i.e. the broadband contribution in the spectrum divided by the total power of the spectrum:

$$E_{\mathrm{BB}} = \frac{\int_{f_{min}}^{f_{max}} C_{\mathrm{BB}}(f)\,\mathrm{d}f}{\text{Total spectrum power}}. \tag{4.12}$$

This is shown by the green shaded area in Figure 4.8 for three typical BB spectral shapes—(approximately) (a) Gaussian, (b) double exponential (Laplacian) and (c) Lorentzian (Cauchy) using the Taylor model. The contribution of the other components were obtained by a similar definition, so $E_{\mathrm{DC}} + E_{\mathrm{LF}} + E_{\mathrm{BB}} + E_{\mathrm{Noise}} \approx 1$ for a valid fitting after filtering. Furthermore, when the contribution of the noise is negligible ($E_{\mathrm{Noise}} \sim 0$), we should have $E_{\mathrm{BB}} \approx 1 - E_{\mathrm{DC+LF}}$, where $E_{\mathrm{DC+LF}} = E_{\mathrm{DC}} + E_{\mathrm{LF}}$ is the total energy contribution of the low-frequency parts in the spectra. From (4.12), E_{BB} ranges between 0 and 1. This means that all the energy of the spectrum is in the BB component when $E_{\mathrm{BB}} = 1$ and in the low-frequency parts when $E_{\mathrm{BB}} = 0$. In other words, E_{BB} reflects the relative intensity of the energy distribution between the BB component and the low-frequency parts. Since the fitting parameters are more stable for the BB component, E_{BB} has a more accurate estimation of the energy contribution than E_{LF}.

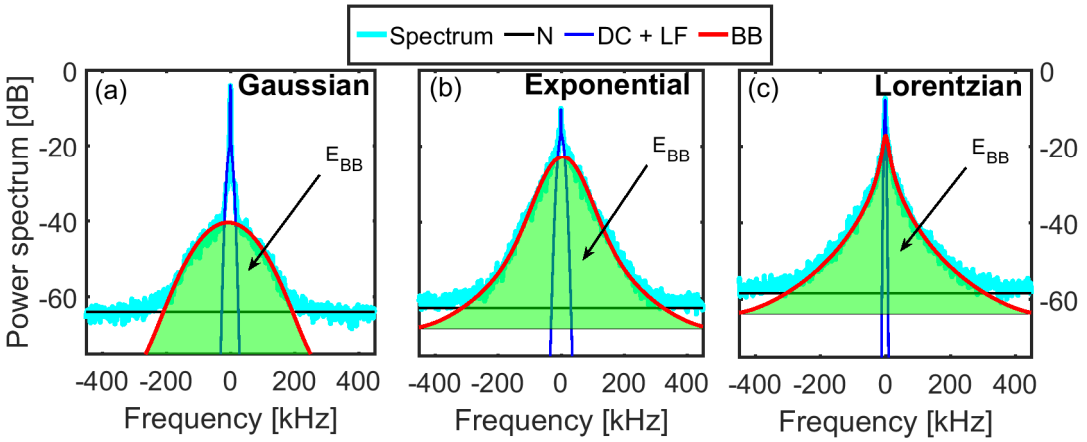

Figure 4.8: Components of typical reflectometry spectra with varying shapes: approximately (a) Gaussian, (b) double exponential (triangular on the logarithmic scale) and (c) Lorentzian. The DC and LF components were fitted by two Gaussian functions, the noise level (N) by a constant and the BB component by the FFT of the Taylor function. The green shaded area represents the integrated BB contribution, denoted by E_{BB}.

Additional fluctuation properties can be obtained from the parametrization, e.g. the standard deviation, i.e. the square root of the second central moment of the BB and LF component, which we refer to as the *BB width* (W_{BB}) and the LF width (W_{LF}). The parameters of spectral energy and width come from the Taylor model, due to its superior performance compared to the other models. In addition, the exponent (β_{BB}) in the generalized Gaussian function provides a convenient measure for the shape of the BB

component, which is strongly related to the kurtosis of the distribution.

The structure of the database is listed in table 4.1, by means of a number of commonly used entries or parameters. All the plasma parameters corresponding to each spectrum (each index in the table) are calculated as the average value during the acquisition time window of each reflectometry fluctuation measurement (typically 10 ms).

Index	ρ	$B_{t,0}$	I_p	q_ψ	n_e	T_e	E_{BB}	W_{BB}	β_{BB}	...
1	0.65	3.86	1.0	3.64	3.5	2	0.1	50	...	...
2	0.54	3.46	1.0	3.63	4.0	3	0.5	100	...	...
...	...	...	...	...	...	...	...	...	...	...

Table 4.1: Structure of the turbulence database built from the Tore Supra database. The index in the first column of the table indicates the serial number of the spectra. The units of $B_{t,0}$, I_p, n_e, T_e and W_{BB} are T, MA, $10^{19}m^{-3}$ and kHz, respectively.

Chapter 5

Systematic analysis on radial profiles of broadband contribution

Contents

In this chapter, a systematic study is carried out of the properties of the frequency spectra from fluctuation measurements using the turbulence database built at Tore Supra. Specifically, we focus on the radial profiles of the broadband contribution (E_{BB}) of the spectra. Section 5.1 presents a number of systematic trends of the database observations of E_{BB} in Ohmic plasmas, followed by a deeper discussion in the linear Ohmic confinement (LOC) regime and in the saturated Ohmic confinement (SOC) regime in section 5.2. Section 5.3 extends the study to the case of plasmas with auxiliary heating, either pure ICRH or LH. It should be noted that all results discussed in this thesis are restricted to the L-mode case, as H-mode was never obtained in Tore Supra discharges. In section 5.4, additional interpretation is given of E_{BB} and a link between E_{BB} and the turbulence level ($\delta n/n$) is established. Summary and discussion are given in section 5.5.

5.1 General trends of E_{BB} in Ohmic plasmas

We first investigate the spectrum properties in Ohmic plasmas. Recalling the discussion in section 4.5.1, only the frequency spectra with low noise level (SNR $>$ 25 dB), dominated by perpendicular reflection (Doppler shift $<$ 50 kHz) in stationary state (I_p = constant during the acquisition time) are considered in the statistical analysis. Our operational definition of an Ohmic plasma covers all cases where each source of auxiliary heating power is below 0.1 MW. For Tore Supra, this means that $P_{ICRH} < 0.1$ MW, $P_{LH} < 0.1$ MW and $P_{ECRH} < 0.1$ MW. This constraint results in a data set consisting of $\sim$ 180,000 spectra from nearly 3,000 discharges. The data set covers the entire radial range from the LFS to the HFS.

5.1.1 E_{BB} profiles at varying q_ψ

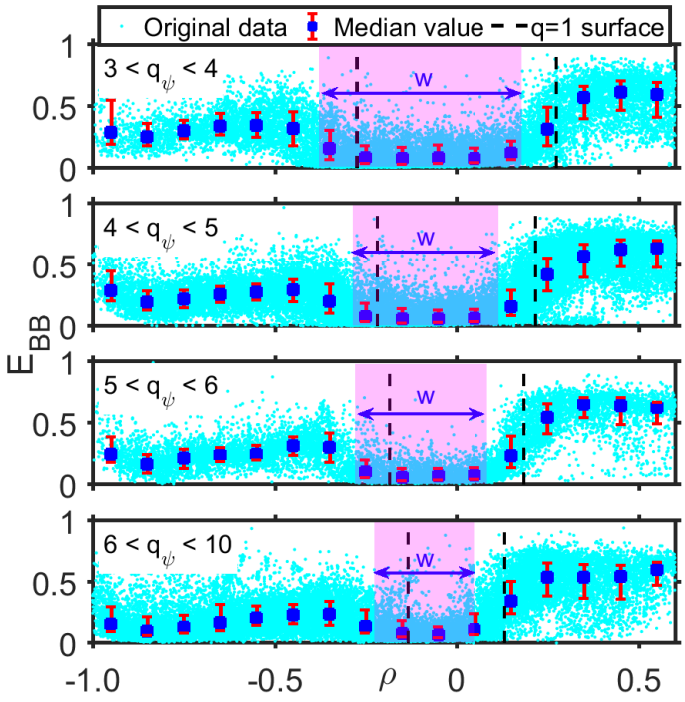

Figure 5.1: Radial profiles of E_{BB} for different q_ψ as a function of normalized radius $\rho = rcos(\theta)/a$, where a is the minor radius of the tokamak ($a \sim 0.72$ m for Tore Supra). Negative ($\theta = 2\pi$) and positive ($\theta = 0$) values refer to the HFS and LFS, respectively. The cyan points are obtained from the individual fitted spectra. The blue square points denote median values calculated within small radial intervals ($\delta\rho \sim 0.1$), with red error bars around the median given by the mean absolute deviation. The $q = 1$ positions are indicated by the black dashed lines.

We have investigated the relation between E_{BB} obtained from the parametrization and various dimensionless quantities determining the confinement performance. We consider radial profiles of E_{BB} for varying edge safety factor (q_ψ), as shown in figure 5.1. The most

remarkable feature is a clear reduction of E_{BB}, which we refer to as the *energy basin*, in the core region for all ranges of q_ψ. Furthermore, there is a clear asymmetry between the HFS and LFS: E_{BB} tends to slowly increase from the inner edge (Lorentzian spectra) towards the center up to the cliff (Gaussian spectra) before the energy basin on the HFS, whereas on the LFS E_{BB} is much higher and reaches saturation (wide Gaussian spectra) above $E_{BB} > 0.5$, indicating that the BB component prevails in the reflected spectra.

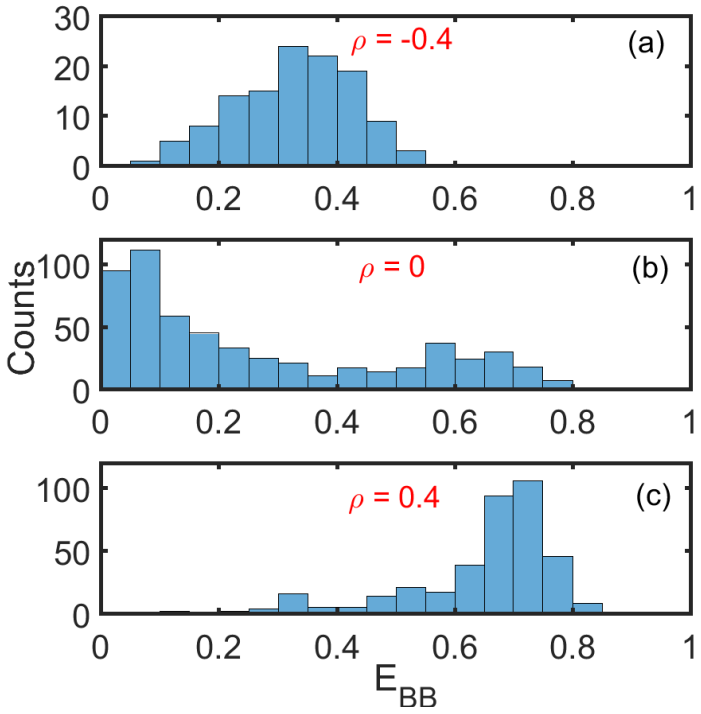

Figure 5.2: Different distributions of E_{BB} at fixed radial positions: (a) $\rho = -0.4$, (b) $\rho = 0$, (c) $\rho = 0.4$, under the condition $5 < q_\psi < 6$.

The considerable radial variation of E_{BB} is not possible caused by the finite beam width, which is expected to be larger than the BB turbulence wavelength. On the other hand, the wavelength of the LF component can be longer than the beam width at the edge, while approaching the beam width close to the center. Unfortunately, Doppler reflectometry, which can evaluate the poloidal correlation length, is not available for core and HFS measurements. However, if the beam size effects were predominant, one would neither observe a change of the position of the energy basin with varying edge q, nor the rise of the E_{BB} on the HFS from the edge up to the basin cliff.

Furthermore, figure 5.1 shows that, at fixed radial position, E_{BB} still varies considerably across the database, for all values of q_ψ. This can be attributed to fitting errors and varying global operational conditions. In Figure 5.2, the distributions of E_{BB} are shown at three radial positions ($\rho = -0.4, 0, 0.4$), in the range $5 < q_\psi < 6$, where the variance of E_{BB} is the lowest. Apart from the large scatter of E_{BB} at fixed radial position, differences in the mean and shape of the distributions are also apparent. Because of the non-zero skewness and outliers in the distributions, we use the median of the distribution rather

than the mean for systematic studies of the typical E_{BB}. When calculating this within small radial intervals of width ~ 0.1, we obtain the blue squares in figure 5.1. The red error bars are given by the mean absolute deviation around the median values within each interval. A similar analysis method relying on the median will be used to capture trends from the highly scattered data hereafter.

5.1.2 Relationship between the E_{BB} basin and the $q = 1$ surface

In figure 5.1, it can also be seen that, as q_ψ increases, the energy basis shrinks. This suggests a relation between the E_{BB} basin and the $q = 1$ surface. However, at Tore Supra, systematic derivation of the $q = 1$ surface from the routine equilibrium reconstruction is affected by considerable uncertainties. Another method to obtain the $q = 1$ position can be the analysis of sawteeth instability from ECE electron temperature measurements. Then, the position of the sawteeth inversion indicates the $q = 1$ position. However, the latter method is only feasible for limited discharges but turns out to be difficult for a large database. Therefore, the position was estimated through the approximate empirical relation $\rho_{q=1} = 1/q_\psi$, established earlier for TFTR and TFR [Arunasalam 1990]. To verify this relation for our database, we employed several typical discharges at different toroidal magnetic field B_0 (3.4 T and 3.86 T), as well as a pulse with an I_p scan, as shown in figure 5.3. Here, the $q = 1$ positions of some selected discharges were obtained from the ECE method. These results are consistent with the empirical relation at both low (3.4 T) and high (3.86 T) magnetic fields, only at very high magnetic fields (3.88 T) there exists some differences. Notice that the consistency between the two methods is better at low q when $\rho_{q=1}$ changes with q rapidly, whereas at high q the effects of the uncertainties are limited due to a slow change rate of $\rho_{q=1}$ with q. This confirms the validity of this empirical relation and providing a practical means to derive the position of the $q = 1$ surface. In each q_ψ range, the median value using $\rho = 1/q_\psi$ gives an approximation to the position of the $q = 1$ surface, shown as the two vertical dashed lines in figure 5.1.

For a quantitative definition of the width of the E_{BB} basin, we employ the criterion $E_{BB} < 0.1$ (value of the median). The radial region of the basin and its width (w) are indicated by the shaded area and the double arrow shown in figure 5.1. In addition, the half-width of the basin ($w/2$) is shown as a function of the normalized $q = 1$ position ($\rho_{q=1}$) in figure 5.4 (a). There is a clear one-to-one correspondence, supporting our hypothesis that the occurrence of the E_{BB} basin is related to the $q = 1$ surface. The error bars on the half-width originate from the limitation on the spatial resolution due to the finite number of points in each radial interval.

Furthermore, Figure 5.4 (b) shows the width of the E_{BB} basin at the HFS ($\rho < 0$) and LFS ($\rho > 0$) separately. Here, the sum of the basin width at the HFS (w_{HFS}) and LFS (w_{LFS}) is just the total basin width (w): $w_{HFS} + w_{LFS} = w$. From figure 5.4 (b), it can be seen that both w_{HFS} and w_{LFS} follow the same increasing trend with respect to $\rho_{q=1}$ as the total width w shown in figure 5.4 (a). However, w_{HFS} is systematically higher (2–3 times) than w_{LFS}, revealing a strong asymmetry of the basin structure at the HFS and LFS. In addition, w_{LFS} increases faster than w_{HFS} with respect to $\rho_{q=1}$. In other words, the absolute difference between w_{HFS} and w_{LFS} decreases with increasing $\rho_{q=1}$ (or

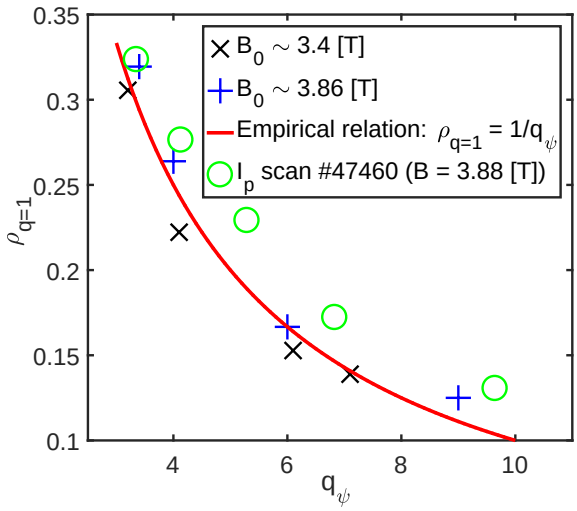

Figure 5.3: Verification of the empirical relation $\rho_{q=1} = 1/q_\psi$ by means of a number of typical discharges from the Tore Supra database.

decreasing q_ψ).

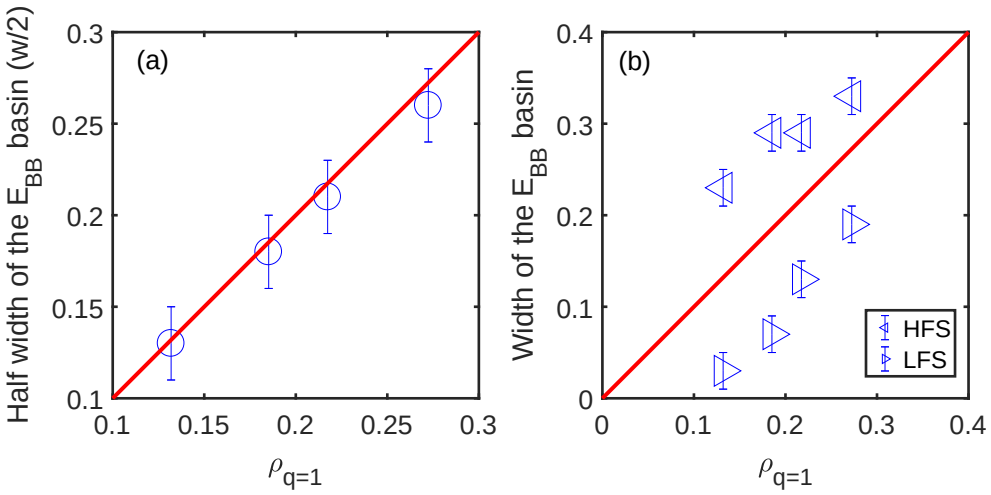

Figure 5.4: (a) Half-width of E_{BB} basin and (b) width of the E_{BB} basin at the HFS and LFS as a function of the $q = 1$ position, both values normalized to the minor radius.

5.1.3 Shift of the cutoff layer

The strong asymmetry of the E_{BB} basin ($w_{HFS} > w_{LFS}$) shown in figure 5.4 (b), can be viewed as a systematic shift towards the HFS of the radial positions. This shift is also observed in figure 5.1, where the actual position of the boundaries of the basin do not coincide with the location of the $q = 1$ surface, indicated by the shaded basin region.

In order to understand the origin of this shift, it is important to recall that the radial positions are the probing wave cutoff positions calculated using the density profile

from the interferometry diagnostic. Hence, the shift might be due to uncertainties on the density profiles from interferometry. To resolve the matter, we have investigated several tens of Ohmic discharges with available core reflectometry profiles. Usually, interferometry underestimates the core density compared to reflectometry. This can be due to the density plateau and the complicated profile structures near the magnetic axis [Sabot 2006a].

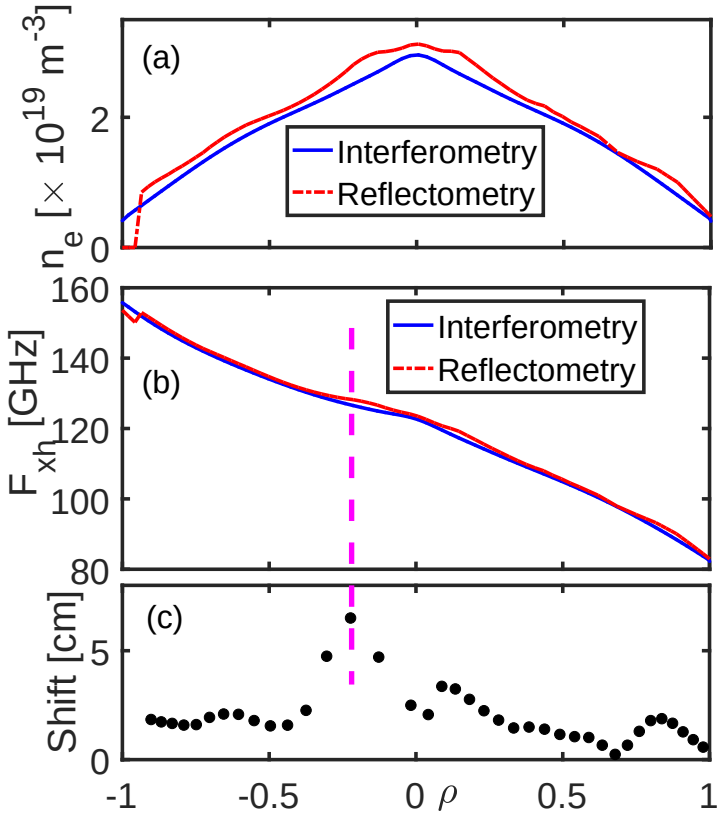

Figure 5.5: (a) Density profiles and (b) upper cutoff frequencies (F_{xh}) near the turbulence signal obtained by core reflectometry and interferometry. (c) Difference of the cutoff positions from interferometry with respect to reflectometry at different radial positions.

To illustrate the uncertainties from interferometry and the resulting cutoff shift, Figure 5.5 (a) shows the density profiles from core reflectometry and interferometry, acquired at the same time in one typical discharge. It can be seen that the core density from interferometry is lower than that from reflectometry. We next calculated the cutoff position using each of the two density profiles, confirming a shift towards the HFS of the cutoff layers from interferometry with respect to reflectometry, as plotted in figure 5.5 (c). There is a clear asymmetry, with a much larger shift in the region $-0.3 \lesssim \rho \lesssim -0.1$ compared to $0.1 \lesssim \rho \lesssim 0.3$, i.e. in the vicinity of the $q = 1$ surface. This is consistent with the observation in figure 5.1, where the $q = 1$ surface is outside the E_{BB} basin on the LFS, but inside the basin on the HFS, with an asymmetry due to the larger shift. The strong shift at the HFS region is caused by the slower increase of the cutoff frequencies (Figure 5.5 (b)) at the HFS than at the LFS [Mazzucato 1998]. The change of shift is

relatively large, even with only a small change of the probing frequency, since the evolution of X-mode upper cutoff frequency with ρ becomes flatter at the HFS, due to the fact that the magnetic field intensity continues to increase, while the density gradient changes sign across the magnetic axis. Thus, the peak of the shift in figure 5.5 (c) corresponds to the flattest part of the cutoff frequency profile deduced from the reflectometry density profile, as indicated by the vertical dashed line in figure 5.5 (b) and (c).

Although the correction of the cutoff shift is feasible for a limited number of selected cases, it is impossible to apply it to a large database with thousands of discharges, as reflectometry density profile measurements cannot be taken at the same time as density fluctuation measurements (as mentioned Section 3.4). Nevertheless, the systematic shift should not considerably affect both qualitative observations and quantitative analysis in this work, although it should be kept in mind. However, the systematic shift attributed to uncertainties of interferometry shows the detection limit of general trends using a database study. Put differently, any observed patterns in the data could be the result of database artifacts, and should be verified by a traditional shot-to-shot analysis. On the other hand, such patterns could be a useful indication of systematic errors in any of the involved diagnostic measurements.

5.2 Radial profiles of E_{BB} in LOC and SOC regimes

As mentioned in section 2.2.4, the Ohmic heating plasmas could be further divided into the LOC and SOC confinement regimes. In the LOC regime, the energy confinement time increases with the density at low density. After a density threshold, the confinement becomes the SOC regime where the confinement times does not change with the density. Since the confinement time is directly linked to the turbulence properties, in this section we investigate in what way the change of the confinement regime could affect the broadband contribution E_{BB}.

5.2.1 Separation of LOC and SOC regimes

In the first step, an effective separation of the LOC and SOC regimes for the Tore Supra database is required. The separation relies on the density threshold of the LOC-SOC transition, which can be approximated as [Shimomura 1985]:

$$n_{\mathrm{LOC-SOC}} \approx \frac{5 I_p \mu_0}{\pi a^2} \sqrt{\frac{A_i \kappa}{2}}. \tag{5.1}$$

Here, $n_{\mathrm{LOC-SOC}}$ is the central line-averaged density in 10^{19} m^{-3}, I_p (A) the plasma current, a (m) the minor radius, A_i the atomic mass number and κ the elongation. A previous study based on a number of dedicated Tore Supra discharges [Arnichand 2014] shows that (5.1) tends to overestimate the density threshold of the LOC-SOC transition. However, for Tore Supra, all prediction parameters in the scaling (5.1) except I_p are almost constant. Specifically, Tore Supra had a circular cross-section and operated with a bottom limiter at an almost constant vertical position, ensuring $\kappa \approx 1$ and $a \approx 0.72$

m. Both κ and a have uncertainties less than 5%. With deuterium operation the atomic mass number A_i is 2, while impurity concentrations were limited, usually less than 10%. Therefore, we have established a reduced empirical scaling law for $n_{\mathrm{LOC-SOC}}$ in terms of I_p from a large number of discharges.

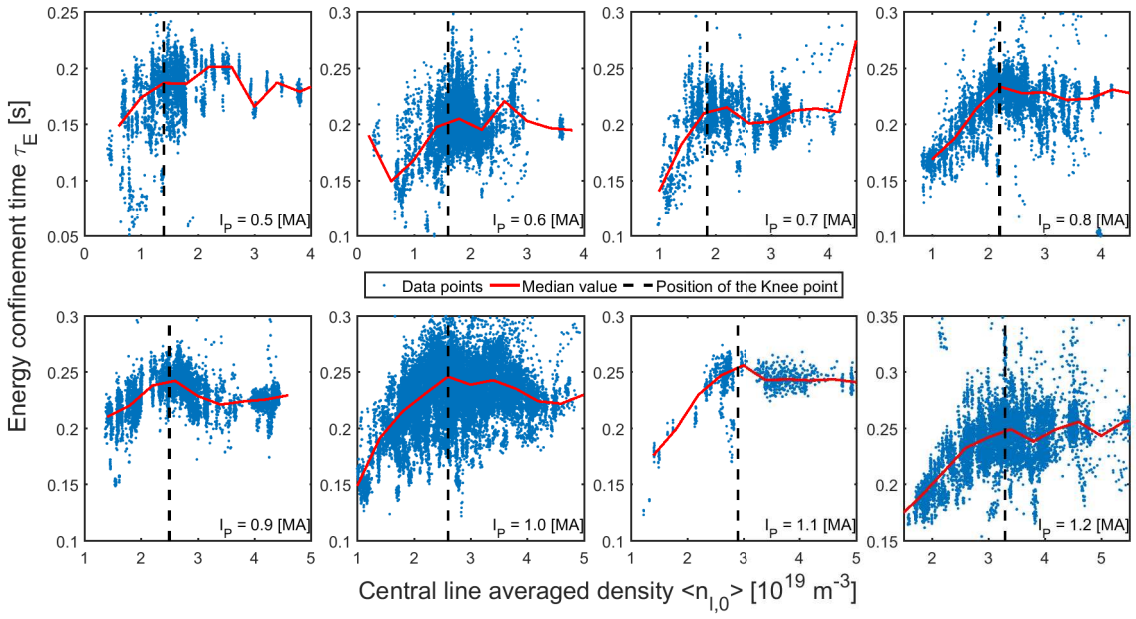

Figure 5.6: Evolution of the total energy confinement time with respect to the central line-averaged density at different plasma current.

Figures 5.6 and 5.7 describe the two steps to obtain the scaling of $n_{\mathrm{LOC-SOC}}$. First, at fixed I_p in Ohmic plasmas, the total energy confinement time (τ_E) increases with the central line-averaged density, passing a knee point at the approximate threshold density and then reaching saturation. Figure 5.6 shows such an evolution of τ_E with line-averaged density (n_l) in the database for different I_p. To compensate for the scatter of the data, the median confinement time is calculated in small density ranges. The knee point of the median curve then provides the estimate of the LOC-SOC transition density threshold. Next, Figure 5.7 shows the evolution of the density threshold at different I_p and the following scaling relation could be obtained by a linear fit:

$$n^{\mathrm{TS}}_{\mathrm{LOC-SOC}} \approx 2.6 \times I_p, \tag{5.2}$$

with $n_{\mathrm{LOC-SOC}}$ in 10^{19} m^{-3} and I_p in MA. The LOC-SOC transition densities obtained from two dedicated density scans at $I_p = 0.5$ MA and 1.2 MA [Arnichand 2014] conform with the scaling law obtained from the database.

Finally, the central line-averaged density $n_{l,0}$ from interferometry measurements [Gil 2009] is used to determine the confinement regime for each reflectometer acquisition, assuming a $\pm 10\%$ uncertainty on the threshold given by the scaling law:

- LOC: $n_{l,0} < 0.9 \times n^{\mathrm{TS}}_{\mathrm{LOC-SOC}}$;

- SOC: $n_{l,0} > 1.1 \times n^{\mathrm{TS}}_{\mathrm{LOC-SOC}}$.

In the remainder, we refer to the intermediate region around the density threshold as the *LOC-SOC transition regime*.

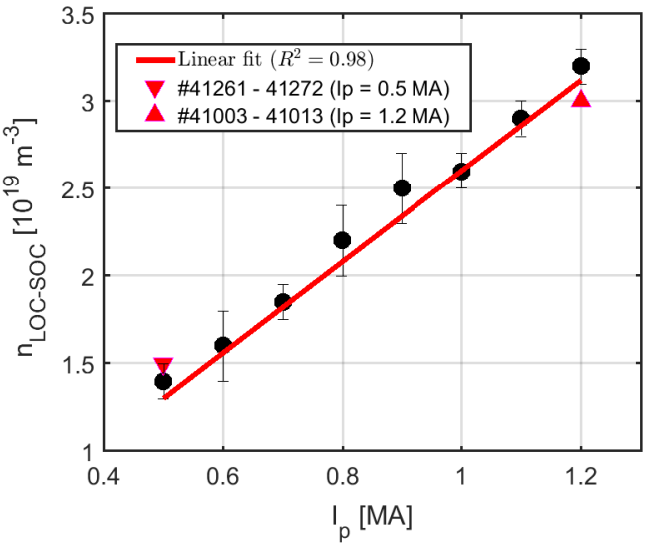

Figure 5.7: Empirical scaling law of the LOC-SOC transition density threshold ($n_{\mathrm{LOC-SOC}}$) in terms of plasma current (I_p).

5.2.2 Radial profiles of E_{BB}

Having discriminated between the LOC and SOC regimes, the radial profiles of E_{BB} can be studied separately in both regimes. Figure 5.8 shows the E_{BB} profiles at different range of q_ψ. Compared to the Ohmic cases in figure 5.1, the general evolution of E_{BB} across the radial extent of the plasma, as well as the E_{BB} basin in the central region, are recovered in both LOC and SOC regimes for all q_ψ ranges. The analysis also recovers the link between the basin (width, location) and the $q = 1$ surface. Far outside the $q = 1$ surface at the LFS, E_{BB} approaches 1 in both regimes, i.e. with most of the energy in the BB component, whereas at the HFS E_{BB} remains at a moderate level. In fact, the general trends become more clear after separating the Ohmic plasmas into the two confinement regimes, as the data in a fixed radial position are less scattered, especially for the LOC regime.

Furthermore, remarkable differences occur for the two regimes, i.e, the magnitude of E_{BB}. At the same range of q_ψ, E_{BB} in SOC is systematically higher than in LOC, which is valid for all q_ψ. Note that since the cutoff positions depend on density, the LFS for the LOC regime is less accessible at higher q_ψ ($5 < q_\psi < 6$ and $6 < q_\psi < 10$), whereas for the SOC regime only the HFS at the lowest q_ψ range is less accessible.

To achieve a better comparison of E_{BB} between the two regimes, the median values for each q_ψ range were calculated by the same method as in the Ohmic case (figure 5.1).

Figure 5.9 shows the radial profiles of the median values for the two regimes, while the original data points have been hidden in view of the strong overlap between the LOC and SOC regimes. The systematically higher E_{BB} in the SOC regime than in the LOC regime, throughout the plasma cross-section for all q_ψ, is clearly confirmed. Specifically, for the LOC regime inside the $q = 1$ surface, E_{BB} is very low, especially at low q_ψ. This means that for the LOC regime in the very core region ($\rho \sim 0$) only a minor part of the energy is in the BB component, or equivalently, most of the energy of the frequency spectra is in the LF component. In contrast, in the SOC regime E_{BB} can still reach levels of 20% at $\rho \sim 0$.

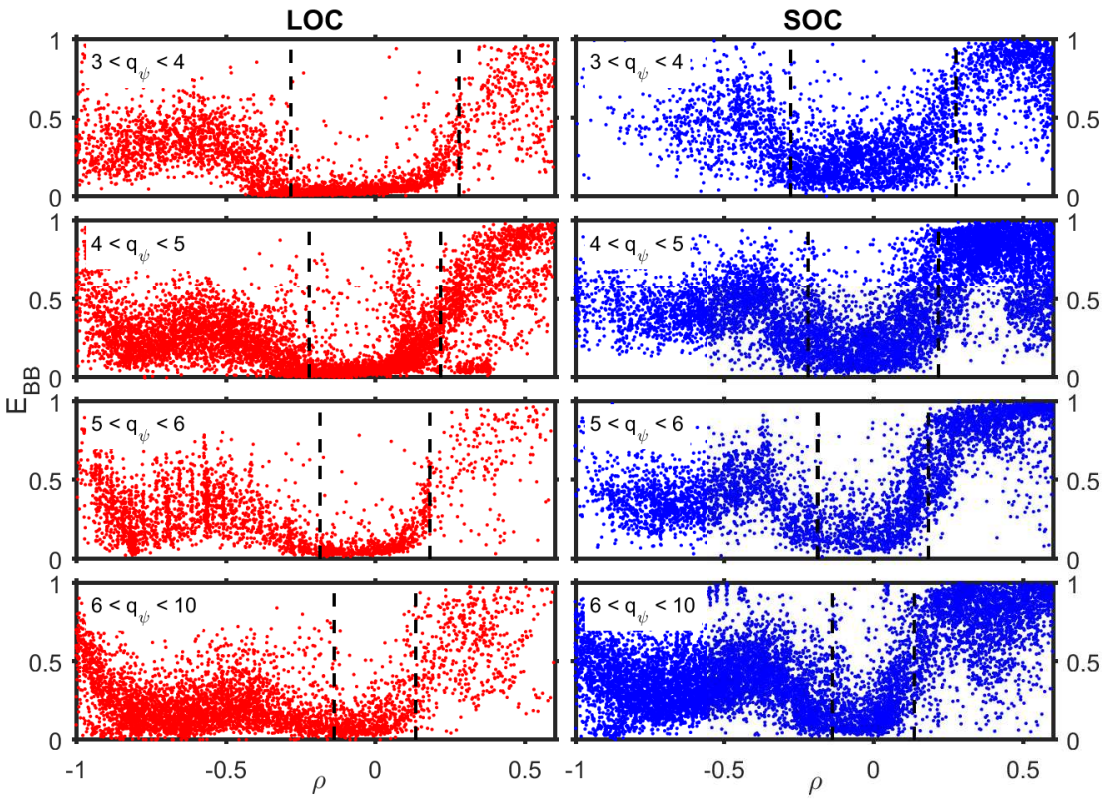

Figure 5.8: Radial profiles of E_{BB} at different q_ψ in the linear Ohmic confinement (LOC) and the saturated Ohmic confinement (SOC). The approximate $q = 1$ surface is shown by the black dashed line for each condition.

For a more quantitative study, the central E_{BB} basin is defined as the corresponding radial range where the median values are below 0.2. Then, E_{BB} inside the basin for both LOC and SOC is plotted as a function of q_ψ in figure 5.10. Remarkable is the higher E_{BB} inside the basin in the SOC regime, compared to the LOC regime, for all q_ψ. The difference between the two regimes disappears at highest q_ψ due to the different trends of E_{BB} with respect to q_ψ. Specifically, with increasing q_{psi}, $E_{\mathrm{BB}}^{\mathrm{LOC}}$ increases rapidly before saturation around $E_{\mathrm{BB}} \approx 0.2$ at high q_ψ, whereas $E_{\mathrm{BB}}^{\mathrm{SOC}}$ decreases slowly to 0.2 at high q_ψ.

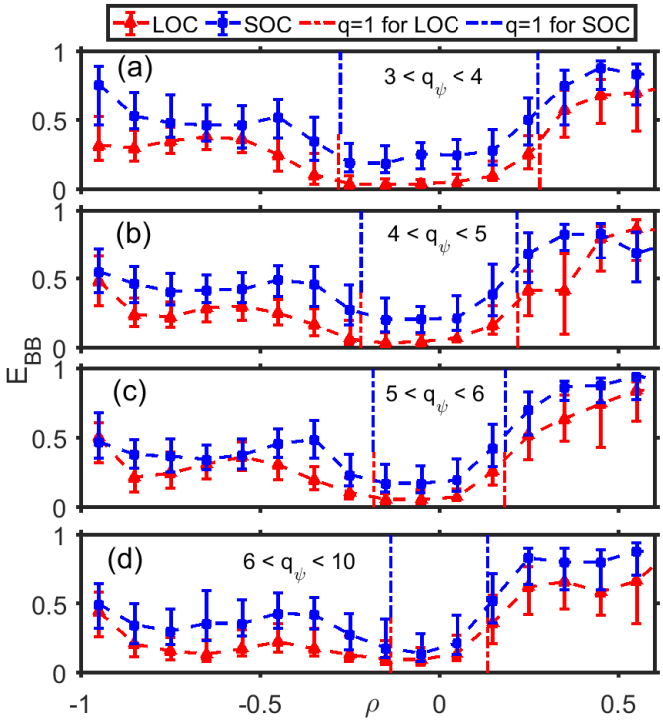

Figure 5.9: Median radial profiles of E_{BB} for different q_ψ in the LOC and SOC regimes. The approximations of the $q = 1$ positions were obtained separately for both regimes by the same method as in figure 5.1.

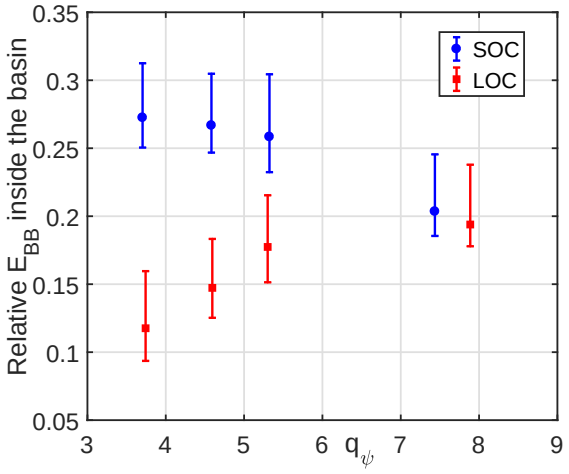

Figure 5.10: Evolution of E_{BB} inside the E_{BB} basin with respect to q_ψ in the LOC and SOC regimes.

5.3 Broadband contribution in terms of injected power

Having investigated Ohmic plasmas, we now turn to the case with auxiliary heating. In Tore Supra, ICRH and LH are the two most commonly applied methods for auxiliary heating or current drive. Note that most of the Tore Supra discharges with LH were

devoted to current drive, allowing the appearance of fast electrons and thus varying ratios of trapped electrons. For clarity, we focus on plasmas that are either pure ICRH or LH plasmas.

Radial profiles of the BB contribution at different ranges of the edge safety factor and heating power are shown in Figures 5.11 (ICRH) and 5.12 (LH). The E_{BB} profiles in Ohmic plasmas with the same range of q_ψ are shown for comparison.

5.3.1 Radial profiles of E_{BB} with ICRH

From figure 5.11, it is clear that E_{BB} is generally considerably higher with ICRH than in Ohmic plasmas, approaching the Ohmic E_{BB} only far outside the $q = 1$ surface. The global increase of E_{BB} should be related to a higher turbulence level with ICRH due to a larger temperature gradient. Specifically, towards the LFS, almost all of the energy is in the broadband component. At the HFS and inside the central basin, E_{BB} increases with increasing heating power. At fixed heating power, a slight rise of E_{BB} is also observed with increasing q_ψ. This rise corresponds to an increase of the fluctuation level due to the degradation of the confinement with increasing q_ψ (i.e. decreasing I_p). This rise has not been observed for the Ohmic cases, because I_p is used as a heating source in Ohmic plasmas and thus the situation is more complicated. Note that at the HFS near the edge, E_{BB} is clearly lower than in the core region. The higher E_{BB} in the core might be caused by fast particles, as the ICRH power deposition occurs mainly in the core at Tore Supra. Specifically, at the lowest ICRH heating powers (0.5 MW $< P_{\mathrm{ICRH}} <$ 1.5 MW), there is a clear E_{BB} basin in the core, but it becomes shallower with increasing P_{ICRH}, and almost disappears when $P_{\mathrm{ICRH}} >$ 2.5 MW. This trend is observed for all q_ψ ranges.

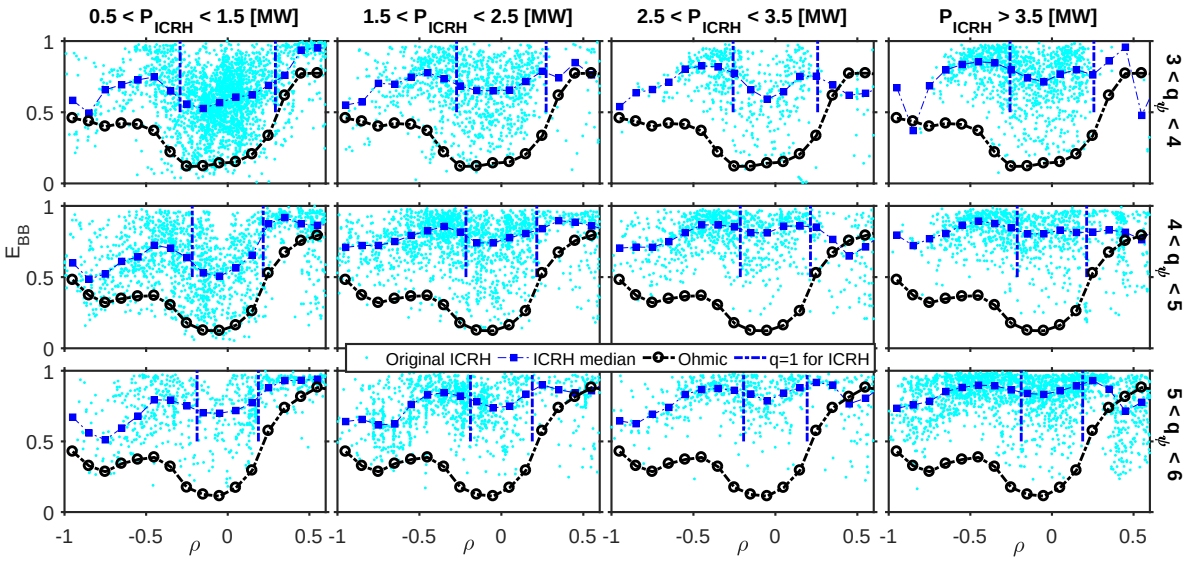

Figure 5.11: Radial profiles of E_{BB} in pure ICRH plasmas (blue) with various ranges of heating power and q_ψ. The $q = 1$ surface for the ICRH plasmas is indicated by the vertical dashed lines in each panel. E_{BB} profiles in Ohmic plasmas (black) are shown for comparison.

5.3.2 Radial profiles of E_{BB} with LH

For the LH plasmas shown in figure 5.12, the E_{BB} basin linked to the $q = 1$ surface remains visible even at very high power ($P_{LH} > 3$ MW). E_{BB} slightly increases along part of the radius with increasing P_{LH}. At fixed heating power, E_{BB} inside the $q = 1$ surface sightly increases with increasing q_ψ. The different behavior of the E_{BB} basin in LH and ICRH plasmas may be linked to differences in the temperature profile inside the $q = 1$ surface for ICRH vs. LH.

A large scatter of E_{BB} at fixed radial position can be noted for both ICRH and LH plasmas, although the scatter is weaker inside the $q = 1$ surface for LH plasmas. Since the $q = 1$ surface is linked with the sawtooth instability, the evolution of E_{BB} during the sawtooth period has been investigated. However, no clear change of the E_{BB} intensity has been observed, except at the time of the sawtooth crash.

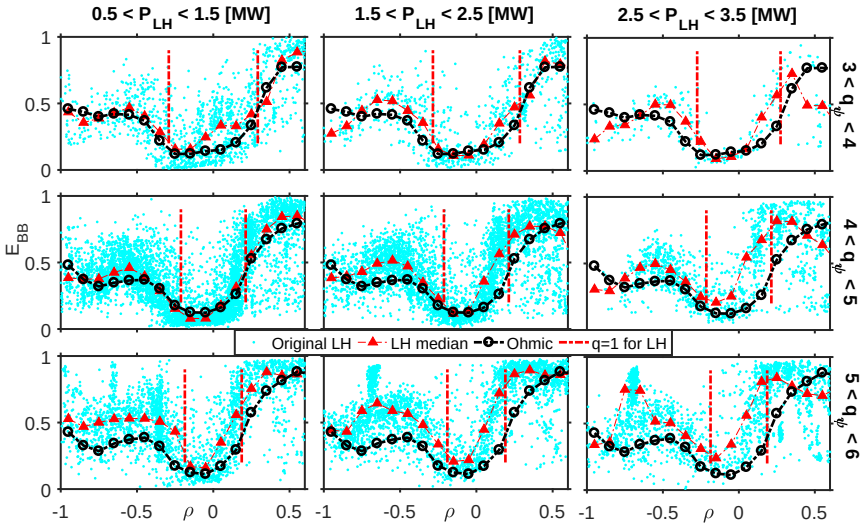

Figure 5.12: Same as in figure 5.11 in LH plasmas (the highest power range is not reached).

Most noticeably, in the central region and at the HFS, there are significant differences between the E_{BB} profiles in plasmas with ICRH vs. LH. In particular, in LH-heated plasmas, E_{BB} is limited, below < 0.5, at the HFS and central region, especially in the latter ($0.1 < E_{\mathrm{BB}} < 0.2$). In contrast, with ICRH, E_{BB} goes well above 0.5 for all radii, reaching levels of 0.7–0.8 in the central region and at the HFS, and even higher at the LFS.

5.4 E_{BB} in terms of fluctuation level

The radial profiles of E_{BB} in Ohmic plasmas identified in figure 5.1 from the database, can be compared to a previous study of the density fluctuation level ($\delta n/n$) in a dedicated discharge #35035 from [Sabot 2006a], as shown in figure 2.11 (a). Comparing the radial profiles of E_{BB} and $\delta n/n$, the basin structure inside the $q = 1$ surface and the strong

asymmetry between the HFS and LFS are similar. Even the slow increase of $\delta n/n$ from the edge towards the center at the HFS in figure 2.11 (a) has also been recovered systematically in figure 5.1. There is a difference between the radial profiles of E_{BB} and $\delta n/n$ at the LFS, where E_{BB} saturates, whereas $\delta n/n$ increases monotonically. In this section, we try to establish a link between E_{BB} and $\delta n/n$.

5.4.1 Confirmation of the general trends of E_{BB}

Note that when constructing the radial profiles of E_{BB}, the spectra were calculated originally from the complex signal and the normalized E_{BB} has been used so far. These factors might cause a distortion of the radial profiles of E_{BB} and are considered in the following to confirm the general trends.

5.4.1.1 Different acquisition methods

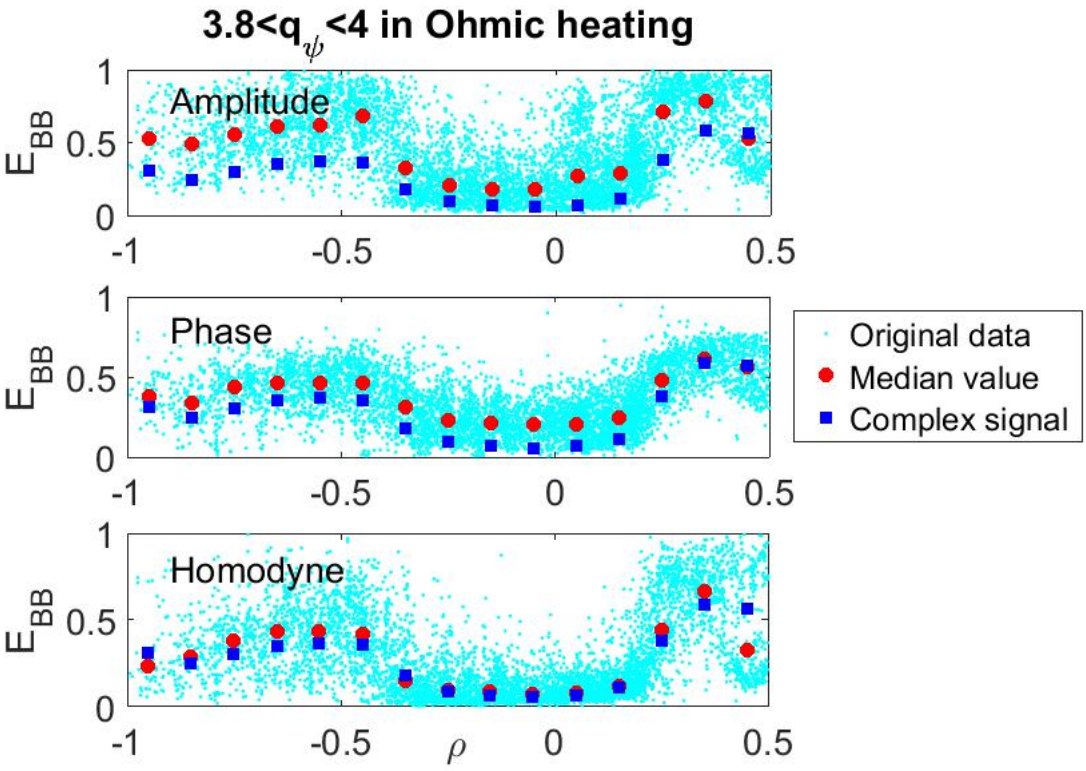

Figure 5.13: Radial profiles of E_{BB} by amplitude, phase and homodyne signals compared with the complex signals used in this study.

First, to confirm that the general trends of E_{BB} observed are independent of the acquisition technique (heterodyne vs. homodyne), we apply the parametrization method to the amplitude (A), the phase (ϕ) and the homodyne signal (Asin(ϕ) or Acos(ϕ)) [Blanco 2013, Fernández-Marina 2014] of the complex signal obtained in this study. Without loss of generality, part of the full database ($3.8 < q_\psi < 4$) has been used in

the comparison to reduce the computational requirements of the test. Figure 5.13 shows the radial profiles of E_{BB} using the three different acquisition techniques, along with the median values for each case. The results using the complex signals are also depicted for comparison. Although some differences among the various signals exist, the general trends of the radial profiles are consistent. Specifically, E_{BB} obtained from the amplitude or phase signals is systematically higher than the complex signal, and the result from the homodyne signal is consistent with the complex signal. The discrepancy near $\rho = 0.5$ at the LFS is expected since the data points are more scattered in this region and are thus less reliable.

5.4.1.2 Radial profiles of the unnormalized E_{BB}

Next, we consider the unnormalized E_{BB}, which is the original energy fraction of the BB component without normalizing to the total power of each spectrum. The unnormalized E_{BB} is referred to as $E_{\mathrm{BB}}^{\mathrm{unnorm}}$ for clarity. Due to the normalization, E_{BB} is also affected by the other components of the frequency spectra, especially the LF component, which could affect the radial profiles of the BB contribution. Moreover, the different behavior of E_{BB} and $\delta n/n$ at the LFS suggests that $E_{\mathrm{BB}}^{\mathrm{unnorm}}$ might also be affected in this region. However, the large variation of the original spectrum power even at a fixed frequency (up to 60 dB) would blur the any radial trends, hence our preference for the normalized E_{BB}. Taking this into account, we limit the reflected power range variation (a band of 9 dB around the maximum of the reflected spectra energy) and select a frequency range (115–140 GHz) in which the reflectometer detection efficiency is the most stable (limited variation of the multiplier output and mixer conversion loss).

Figure 5.14 (a) shows the radial profile of $E_{\mathrm{BB}}^{\mathrm{un-norm}}$ at $3 < q_\psi < 4$ at selected spectral powers and frequencies. Inside the $q = 1$ surface, $E_{\mathrm{BB}}^{\mathrm{un-norm}}$ remains small with low dispersion, whereas outside the $q = 1$ surface, $E_{\mathrm{BB}}^{\mathrm{un-norm}}$ is much higher with strong dispersion at both the HFS and LFS. Moreover, $E_{\mathrm{BB}}^{\mathrm{un-norm}}$ at the LFS is systematically higher than at the HFS. Due to the large difference of $E_{\mathrm{BB}}^{\mathrm{un-norm}}$ between the core and edge region, the radial profile is also shown on the logarithmic scale (Figure 5.14 (b)). From the V-shaped trend through the cross-section, we deduce that $E_{\mathrm{BB}}^{\mathrm{un-norm}}$ decreases almost exponentially from the edge to the core region. The observations from $E_{\mathrm{BB}}^{\mathrm{un-norm}}$ again confirm the general trends from figure 5.1.

Moreover, since $E_{\mathrm{BB}}^{\mathrm{un-norm}}$ should be more directly linked to the measurements of phase fluctuations ($\delta\phi$) by reflectometers, as opposed to density fluctuations ($\delta n/n$), the factor connecting $\delta n/n$ to $\delta\phi$ should be considered. From section 3.2.2, $\delta\phi$ is related to $\delta n/n$ as [Shelukhin 2006]:

$$\delta\phi \propto \sqrt{\frac{L_\varepsilon \Delta_r^{cor}}{\lambda_0}}\frac{\delta n}{n}, \tag{5.3}$$

where $L_\varepsilon = (\partial\varepsilon/\partial r)^{-1}$ is the scale length of the plasma permittivity ε at the cutoff position, λ_0 the wavelength of the probing wave and $\Delta_r^{cor} \approx 1/k_{\mathrm{eff}}$ the turbulence radial correlation length. Therefore, in order to recover the radial profiles of $\delta n/n$, a correction factor $\sqrt{\frac{L_\varepsilon \Delta_r^{cor}}{\lambda_0}}$ should be taken into account. The turbulence correlation length Δ_r^{cor} is

not available for the whole database and is assumed to be constant (~ 1 cm) across the radial cross-section. Figure 5.14 (c) and (d) show the radial profiles of $E_{\mathrm{BB}}^{\mathrm{un-norm}}$ considering the correction factor in the linear and logarithmic scale, respectively, exhibiting similar trends. The dispersion of the data is significantly reduced, indicating a better recovery of the trends after adding the correction factor.

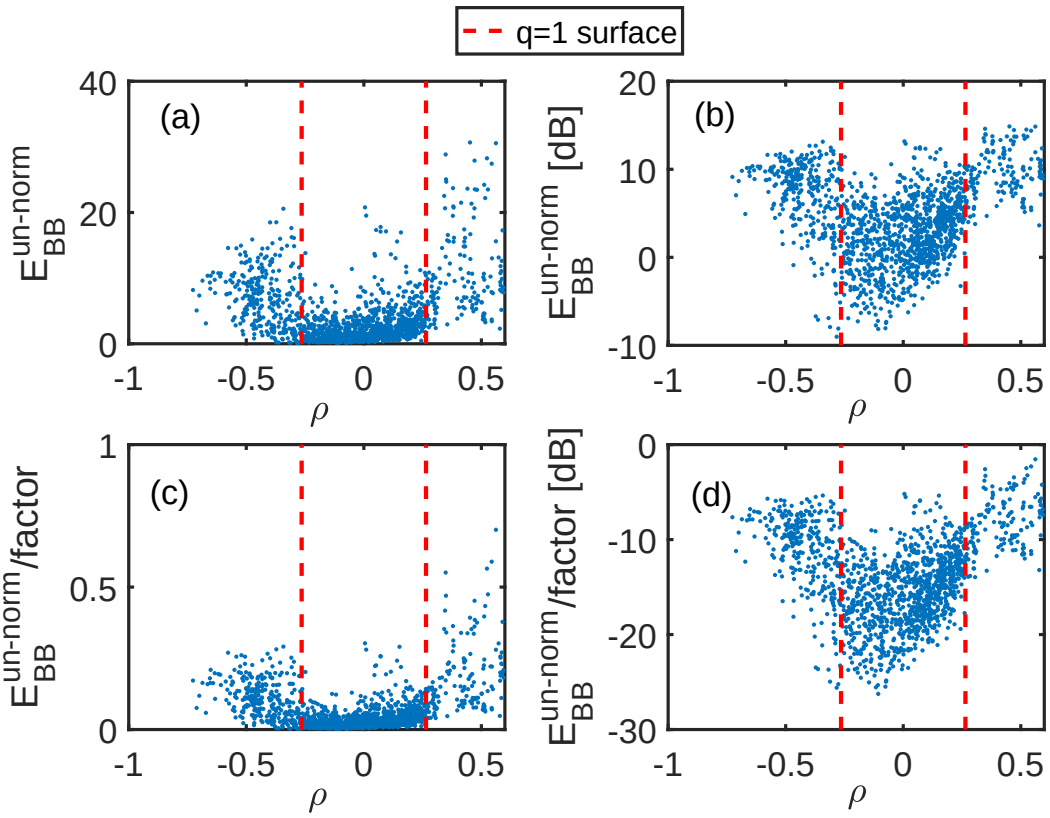

Figure 5.14: Radial profiles of the unnormalized E_{BB} ($E_{\mathrm{BB}}^{\mathrm{unnorm}}$) in the (a) linear and (b) logarithmic scale. Radial profiles of $E_{\mathrm{BB}}^{\mathrm{unnorm}}$ considering the correction factor in the (c) linear and (d) logarithmic scale. The edge safety factor is in the range $3 < q_\psi < 4$. The approximate $q = 1$ positions are indicated by the red vertical dashed line.

5.4.2 Radial profiles of the corrected E_{BB}

Although $E_{\mathrm{BB}}^{\mathrm{un-norm}}$ may be more directly linked to the turbulence level than E_{BB}, the application of $E_{\mathrm{BB}}^{\mathrm{un-norm}}$ to a large database requires strong constraints on power and frequency. Therefore, to conduct a systematic study without these limits, we focus on E_{BB}, which can be calculated for the entire database without limitations. The analysis of $E_{\mathrm{BB}}^{\mathrm{unnorm}}$ could be a complementary parameter when investigating dedicated discharges in a deeper study. On the other hand, the correction factor $\sqrt{\frac{L_\varepsilon \Delta_r^{cor}}{\lambda_0}}$ might help to strengthen the general trends (as shown in figure 5.14).

First, we consider the correction factor in the study of the radial profiles of E_{BB} in Ohmic plasmas, as shown in figure 5.15. As expected, the general trends of the corrected

E_{BB} (E_{BB}/factor) are consistent with the results from E_{BB} with reduced data dispersion at fixed radial positions. The only difference lies at the LFS near the plasma edge, where the corrected E_{BB} increases monotonically from the core towards the edge. This is consistent with the radial profiles of $\delta n/n$.

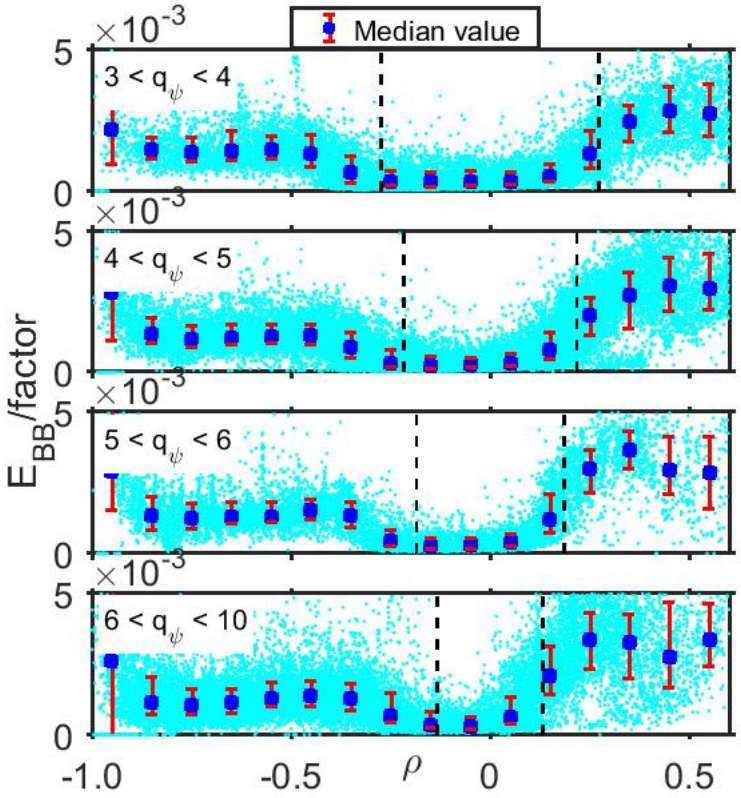

Figure 5.15: Same as figure 5.1, but considering the correction factor $\sqrt{\frac{L_\varepsilon \Delta_r^{cor}}{\lambda_0}}$.

Furthermore, we extend the analysis to L-mode plasmas with auxiliary power. In order to systematically compare the results of turbulence level (figure 2.12) from previous studies [Guirlet 2010], similar ranges of heating power of ICRH and LH have been selected. Figure 5.16 shows the radial profiles of the corrected E_{BB} in ICRH or LH plasmas. The radial profile in Ohmic plasmas at corresponding q_ψ is also shown for comparison. From figure 5.16, the radial profiles of the turbulence level from figure 2.12 has been systematically recovered for a much larger range of plasma conditions. Specifically, the dedicated LH-dominated discharge of figure 2.12 has a fraction (25%) of ICRH. However, in our database study, for the selected range of parameters (q_ψ and power), there are only a few discharges with similar LH and ICRH power. It was thus preferred to show the pure LH cases. This explains the small difference between shot #34931 of figure 2.12 and the LH cases in figure 5.16. Moreover, the results shown in figure 5.16 are only an example of the full parameter range, as shown by figures 5.11 and 5.12 (and also figure 5.1).

The remarkable difference between the BB contribution shown in figures 5.11, 5.12

and 5.16 for ICRH and LH plasmas with similar heating power lead us to investigate further. Figure 5.17 (a) shows the E_{BB} in the core for ICRH and LH plasmas at different heating power. E_{BB} in the core increases almost linearly with heating power for both ICRH and LH plasmas and E_{BB} with ICRH is systematically higher than with LH for all heating powers. The difference of E_{BB} between ICRH and LH is almost independent of the heating power. To understand the origins of the discrepancy, we have investigated the corresponding energy confinement time (τ_E) at different power for ICRH and LH plasmas, as shown in figure 5.17 (b). Here, a median value of the confinement time in the range of heating power has been used. The differences of τ_E among ICRH and LH plasmas are much smaller than the differences of E_{BB}. Importantly, this suggests that the huge difference of E_{BB} between ICRH and LH plasmas cannot be explained by a degradation of confinement, and therefore some other mechanism must be at work.

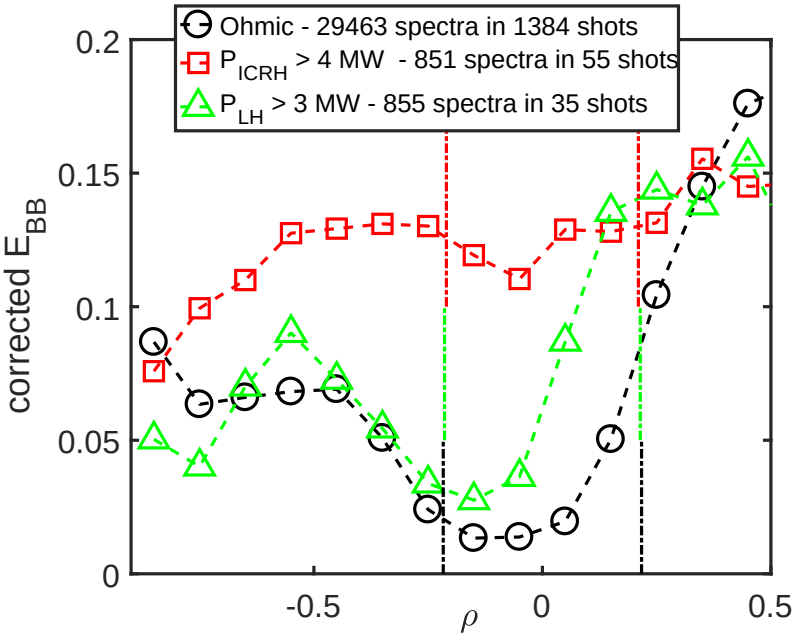

Figure 5.16: Radial profiles of E_{BB} in Ohmic, ICRH and LH plasmas under the condition $4 < q_\psi < 5$. The $q = 1$ positions are indicated by the vertical dashed lines with the corresponding color.

5.5 Summary and discussion

Radial profiles of the BB contribution in frequency spectra have been systematically studied for both Ohmic and L-mode plasmas with ICRH and LH heating. The general observed trends are summarized in the following:

- In Ohmic plasmas, a drastic reduction of the BB contribution, called the E_{BB} basin, is observed inside the core region. The position and width of the reduction are correlated with the $q = 1$ surface. A strong asymmetry of the BB contribution exists at the HFS and LFS.

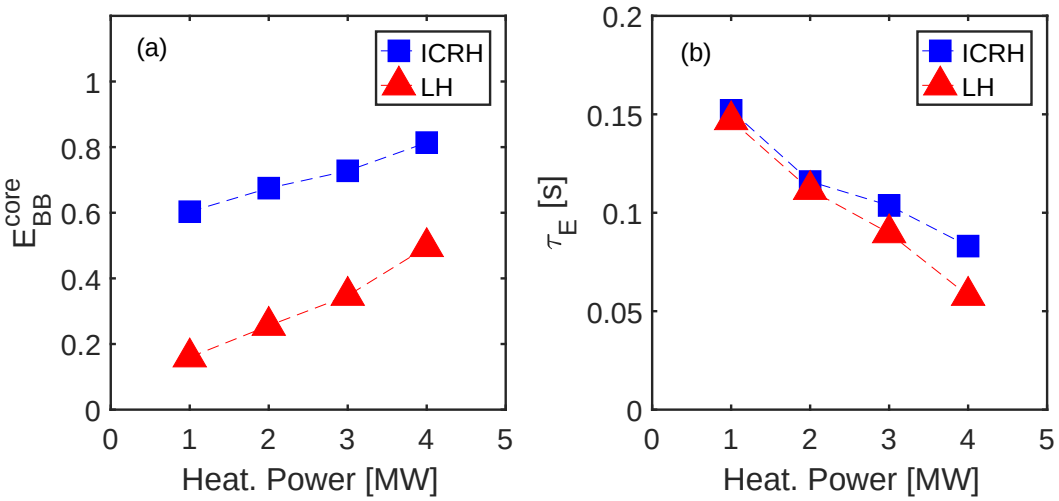

Figure 5.17: (a) E_{BB} inside the $q = 1$ surface and (b) the energy confinement time at different heating power for ICRH and LH plasmas for a large range of edge safety factor (q_ψ)).

- In the LOC and SOC regimes, the trends observed in Ohmic plasmas are strengthened. Moreover, the BB contribution in the SOC regime is systematically higher than in the LOC regime.
- For the auxiliary heating case, the E_{BB} basin is recovered in the pure LH plasmas, whereas for the pure ICRH plasmas, the basin disappears even at low heating power. In addition, with increasing heating power or edge safety factor, the BB contribution increases for both ICRH and LH plasmas.

The radial profiles of E_{BB} systematically recover the profiles of the turbulence level obtained in earlier dedicated studies. Hence, we have been able to systematically reconstruct the turbulence level in an automated way across a large data set. However, the turbulence correlation length is not available for across the entire database and is thus assumed to be the same at different radial positions. The validity of this assumption needs to be verified by radial correlation measurements [Kosolapova 2012].

The most remarkable observation from the database study is the clear difference of E_{BB} between the LOC and SOC regions, and furthermore the drastic disparity of E_{BB} between ICRH and LH plasmas at comparable heating power. In the next chapter, we propose a number of possible interpretations of these observations, after considering the dependence of several additional spectral parameters of both the BB and LF components on specific plasma conditions.

Chapter 6

Collisional effects on reflectometry fluctuation spectra

Contents

In the previous chapter, we have observed various differences of the broadband contribution E_{BB} between the LOC and SOC regimes, and between ICRH and LH plasmas. In this chapter, we turn to a possible explanation of these observations, by investigating the dependence of E_{BB} on collisionality.

At low density, we observed that E_{BB} increases slowly with density. However, further increasing the density, E_{BB} becomes strongly dispersed at fixed density, making it difficult to identify a clear trend. On the other hand, since the density affects the plasma collisionality, which in turn is known to affect the growth rate of instabilities, we decided to investigate the dependence of E_{BB} on collisionality, as this might given an indication whether the type of dominating instability is related to the observations of E_{BB}.

The link between dominating instability and reflectometry frequency spectra has been extensively studied in terms of the quasi-coherent (QC) components in the spectra [Arnichand 2014]. Specifically, the disappearance of the QC modes has been proved to be a marker of the stabilization of the TEM instability [Arnichand 2015, Zhong 2016, Lee 2018]. We here wish to verify the possibility that a transition in the dominant instability may affect also the other components of the frequency spectra, i.e. the broadband (BB) and low-frequency (LF) components. This could be a suitable explanation for the observed trends of E_{BB} with different confinement regimes and heating methods.

However, linking the frequency spectra to the dominating instability by calculating the growth rates at different collisionality for the whole database would be impossible from the computational point of view. Therefore, in this chapter, we focus on linking changes in the BB and LF components with changes in the collisionality, by studying the dependence of the spectral properties (energy, width, shape) of the BB and LF components on collisionality. Section 6.1 first investigates the dependence of the BB component on collisionality in Ohmic plasmas and then discusses the possible interpretation in terms of a transition of dominant instability. This is based on the results of earlier gyrokinetic simulations and is supported by additional analysis of the density peaking and the LF component. Then, the study is extended to L-mode plasmas with ICRH and LH heating and possible interpretations are given. Additional discussion and perspectives are provided in section 6.3.

6.1 Dependence of frequency spectrum on collisionality in Ohmic plasmas

As mentioned in section 2.3.4, the LOC regime and SOC regime in Ohmic plasmas have been connected with the microinstability of TEM and ITG, respectively, and collisions has a crucial impact on the determination of the LOC-SOC transition. Therefore, to understand the difference of E_{BB} in the LOC and SOC egimes, this section studies the dependence of the spectral characteristics on effective collisionality. The effective collisionality ν_{eff} has been calculated by means of (2.17). Since the local Z_{eff} is unavailable for the Tore Supra database, the integrated (tangential) Z_{eff} value has been used in calculating ν_{eff}. Although some systematic uncertainty of ν_{eff} might occur when a constant Z_{eff} is used, global trends at fixed radial positions are not noticeably affected, especially in the core region.

6.1.1 Dependence of density peaking on collisionality

As mentioned in section 2.3.4, the occurrence of density peaking has been used as an indicator of the dominant instability [Angioni 2005]. In this study, the density peaking is defined as the ratio between the central electron density (n_{e0}) and the averaged electron density ($\langle n_e \rangle$), as measured by interferometry: density peaking $= n_{e0}/\langle n_e \rangle$. Since a large variation of plasma conditions is represented in our database, to confirm the link between the LOC-SOC transition and the transition between dominating instability, we have also investigated the dependence of density peaking on collisionality.

Figure 6.1 shows the evolution of the density peaking with respect to the effective collisionality ν_{eff} for a broad range of edge safety factor ($3 < q_\psi < 6$) in the central region ($-0.1 < \rho < 0.1$). The central density and temperature have been used in calculating ν_{eff}. Since a strong dispersion of data occurs at fixed ν_{eff}, the smoothed median values at different ν_{eff} are shown. The median values have been calculated from a small fixed interval (0.01) of ν_{eff} on the logarithmic scale.

As expected, the LOC and SOC regimes correspond to low and high ranges of ν_{eff}, respectively. In the LOC regime, density peaking increases with ν_{eff}, whereas in the SOC regime, density peaking decreases. These opposite trends result in a maximal density peaking factor within the transition regime, at about $\nu_{\text{eff}} \sim 0.2$. At high ν_{eff}, the decrease of density peaking with ν_{eff} has been widely studied at ASDEX Upgrade [Angioni 2003, Angioni 2005]. At low ν_{eff}, the increase of density peaking might be explained by the impact of the plasma resistivity on the neoclassical Ware pinch, resulting from the trapped particles. Since the plasma resistivity ($\propto T_e^{-3/2}$) increases with effective collisionality ($\propto T_e^{-2}$), the increase of effective collisionality (ν_{eff}) leads to an increase of the toroidal electric field (E_ϕ). Furthermore, this increase of E_ϕ induces an increase of the (inward) Ware pinch, resulting in a higher density peaking. With a further increase of ν_{eff}, leading to transition from the banana to the plateau collisional regime, one could expect a saturation or even an attenuation of the Ware pinch, due to detrapping of the trapped particles. The fact that the density peaking reaches its maximum at the transition between the LOC and SOC regimes, could be a signature of the transition from TEM to ITG dominated turbulence [Sun 2019].

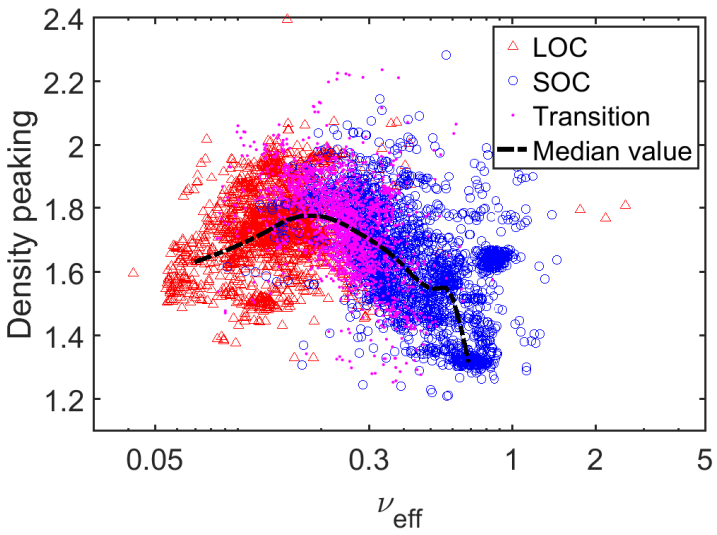

Figure 6.1: Plot of the density peaking factor with respect to effective collisionality for Ohmic plasmas with $3 < q_\psi < 6$.

6.1.2 Dependence of BB component on collisionality

Having characterized the trend of density peaking in terms of collisionality, linked with a possible change of dominating instability across the LOC-SOC transition, we now proceed to a study of changes in the BB component resulting from the transition. This is based on the BB contribution (E_{BB}), the BB width (W_{BB}) and the BB shape (β_{BB}).

6.1.2.1 BB contribution

Figure 6.2 shows the dependence of E_{BB} on ν_{eff} in the LOC, SOC and transition regimes at the HFS ($\rho = -0.4$), the plasma center ($\rho = 0$) and the LFS ($\rho = 0.4$). The HFS and LFS radial positions ($\rho = \pm 0.4$) have been chosen to be neither in the region with large radial changes of E_{BB} ($0.2 < |\rho| < 0.3$), nor in the saturation region ($\rho > 0.6$) (see figure 5.9). At each ρ, the data include all the q_ψ ranges shown in figure 5.9. Note that ν_{eff} was estimated from the local values of n_{e} and T_{e}. For Z_{eff}, again the estimate from a tangential line-of-sight was used to calculate ν_{eff}. It is strongly weighted by the plasma core, so even if Z_{eff} would increase toward the edge, all data points at the LFS and HFS would merely shift slightly toward higher ν_{eff} (under the assumption that the shape of the Z_{eff} profile does not change drastically with increasing ν_{eff}).

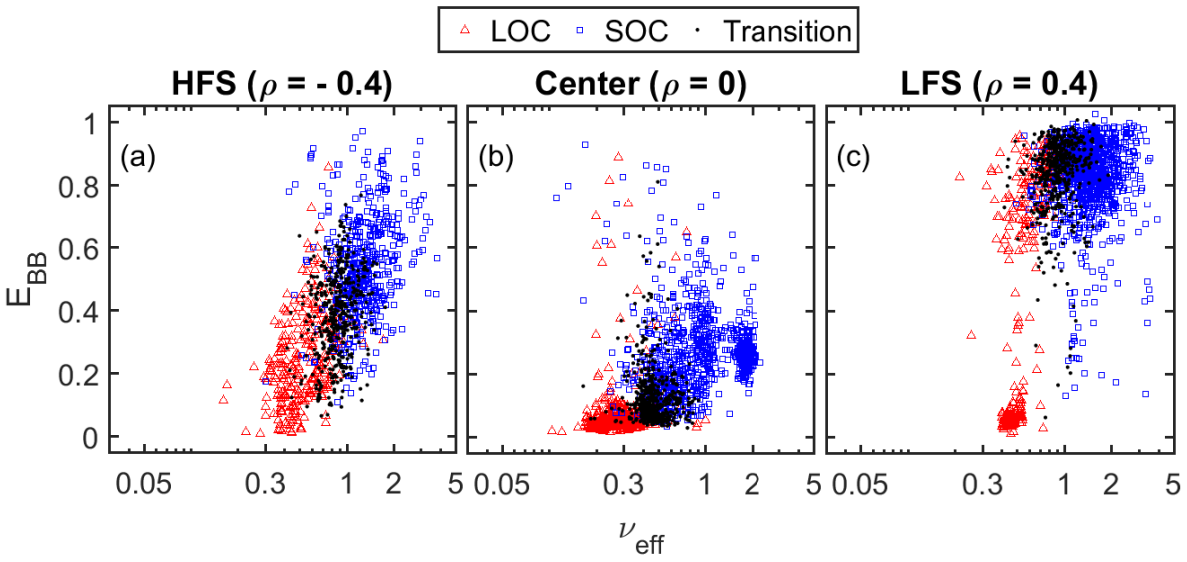

Figure 6.2: Broadband contribution (E_{BB}) vs. effective collisionality (ν_{eff}) in the LOC, SOC and transition regimes at (a) the HFS ($\rho = -0.4$), (b) the plasma center inside the basin ($\rho = 0$) and (c) the LFS ($\rho = 0.4$). Note the logarithmic scale for ν_{eff}.

Despite the significant scatter of E_{BB} in the plots, the following observations can be made. Inside the central E_{BB} basin (figure 6.2 (b)), in the LOC regime, E_{BB} remains low (~ 0.1) for ν_{eff} ranging from below 0.1 to around 0.3. Above $\nu_{\mathrm{eff}} = 0.3$, E_{BB} generally increases rapidly as the plasma transits from the LOC to the SOC regime. Outside the basin (figure 6.2 (a) and (c)), ν_{eff} (calculated from local n_{e} and T_{e}) is generally higher than in the center, due to the stronger dependence of ν_{eff} on T_{e} than on n_{e} (from (6.1): $\nu_{\mathrm{eff}} \propto T_{\mathrm{e}}^{-2}$ and $\nu_{\mathrm{eff}} \propto n_{\mathrm{e}}$), while generally a T_{e} profile is steeper than an n_{e} profile. At the HFS (figure 6.2 (a)), E_{BB} increases almost linearly when ν_{eff} changes from 0.3 to 3 on a logarithmic scale. At the LFS (figure 6.2 (c)), E_{BB} also increases with ν_{eff}, but it quickly reaches values close to saturation when $\nu_{\mathrm{eff}} > 0.5$. Note that a cluster of spectra accumulates at $\nu_{\mathrm{eff}} \sim 0.5$ when $E_{\mathrm{BB}} < 0.2$. This remarkable cluster corresponds to the cluster in figure 5.8 (LOC case with $4 < q_\psi < 5$). A preliminary investigation has pointed out that the spectra making up this cluster correspond to a number of contiguous

Tore Supra discharges (#40481 – #40490). These measurements come from the same acquisition channel and have the same probing frequency (120 GHz), indicating a possible technical problem of this channel for this series of discharges.

Although here the results at only three radial positions are presented, similar trends have been observed at other radial positions, except close to the plasma edge, where saturation occurs. The saturation could be due to an increase of the fluctuation level close to the plasma edge in combination with stronger nonlinear effects. In summary, an increasing trend of E_{BB} with ν_{eff} is consistently observed throughout the entire plasma cross-section. Inside the E_{BB} basin, at low ν_{eff} the increase is relatively weak, becoming steeper above $\nu_{\mathrm{eff}} = 0.3$.

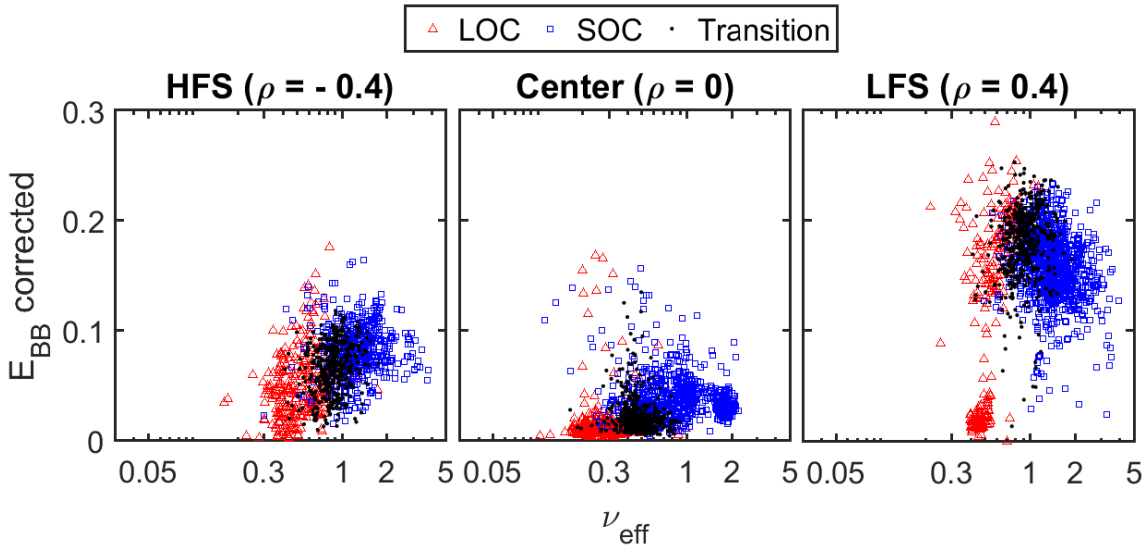

Figure 6.3: Corrected E_{BB} vs. ν_{eff} in the LOC, SOC and transition regimes at (a) the HFS ($\rho = -0.4$), (b) the plasma center inside the basin ($\rho = 0$) and (c) the LFS ($\rho = 0.4$). Note the logarithmic scale for ν_{eff}.

Furthermore, after considering the scale length of the refraction index (L_ε) and the frequency of the probing wave (λ_0), the dependence of the corrected E_{BB} on ν_{eff} at different positions is shown in figure 6.3. Generally, similar trends of E_{BB} are recovered, as is clear from figure 6.2. The only difference comes from the high ν_{eff} at the LFS (figure 6.3 (c)), where a decrease of the corrected E_{BB} with ν_{eff} is observed.

6.1.2.2 BB width and shape

In addition to studying the broadband contribution through E_{BB}, we have also investigated in a similar way the width (W_{BB}) and shape (β_{BB}) of the BB component. As mentioned in section 4.5.2, W_{BB} is obtained from the Taylor model due to its more stable behavior, while β_{BB} from the generalized Gaussian provides the most direct interpretation of the spectral shape. Specifically, $\beta_{\mathrm{BB}} = 2$ and $\beta_{\mathrm{BB}} = 1$ correspond to the standard Gaussian and double exponential shape, respectively, while the Lorentzian shape occurs for $\beta_{\mathrm{BB}} \lesssim 1$.

Figure 6.4 (a–c) shows the evolution of the BB width W_{BB} with ν_{eff} at different ρ. Inside the central basin (figure 6.4 (b)), unlike E_{BB}, W_{BB} does not change much with ν_{eff} and remains around 50 kHz. At the HFS (figure 6.4 (a)), W_{BB} increases and decreases with ν_{eff} in LOC and SOC regime, respectively, resulting in a maximum W_{BB} value at the transition. However, at the LFS (figure 6.4 (c)) where E_{BB} is close to saturation (figure 6.2 (c)), the pattern is more complicated. One may distinguish two main clusters: one with $W_{\mathrm{BB}} > 100$ kHz, roughly increasing with ν_{eff}, and the other with W_{BB} remaining approximately at ~ 50 kHz, even at high ν_{eff}. Another interesting observation is that W_{BB} tends to be scattered the most in the transition regions, where different types of instabilities might co-exist.

Figure 6.4 (d–f) shows the evolution of the BB shape β_{BB} with ν_{eff} at different ρ. No clear trends can be discerned, but a few observations can be made. First, in the plasma center, the dispersion of β_{BB} is clearly larger in the LOC regime than in the SOC regime. Second, at high ν_{eff}, the β_{BB} values tend to cluster around 1, corresponding to a double exponential shape.

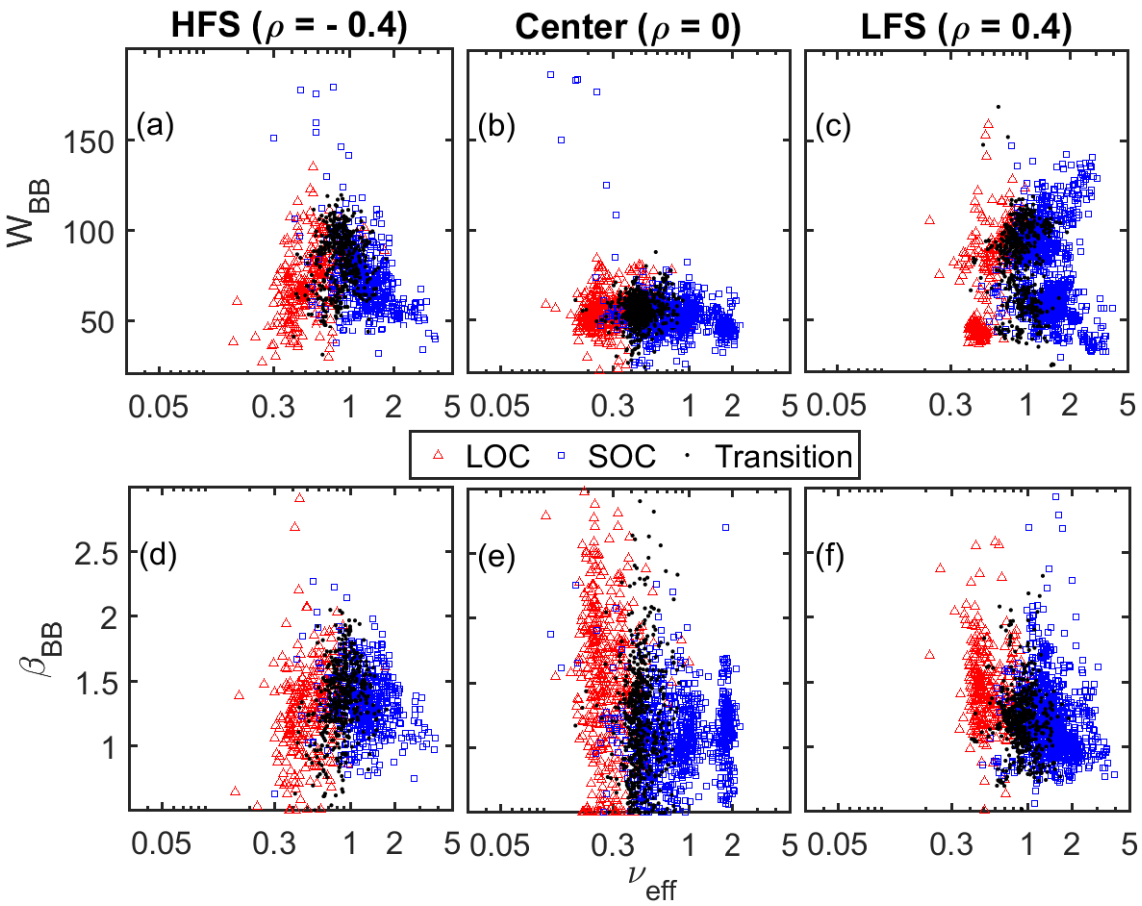

Figure 6.4: Similar to figure 6.2 for the evolution of the broadband width W_{BB} and shape β_{BB}.

6.1.3 Interpretation of spectrum dependencies on confinement regime

We propose a possible interpretation of the observed trends of the BB component in terms of ν_{eff} by a change of the dominant instability from TEM to ITG, when crossing from the LOC to the SOC regime. This interpretation is suggested by the dependence of density peaking on collisionality in figure 6.1. Furthermore, it is lent by an earlier, dedicated study of the effect of the dominant instability on the density fluctuation spectra by gyrokinetic simulations in the Ohmic Tore Supra discharge #48102 [Arnichand 2016, Citrin 2017]. The simulations were performed at $\rho = 0.37$, which is close to the position in the database study ($\rho = 0.4$) at the LFS. Figure 6.5 shows that, in the LOC regime when TEM dominates, the BB component is separated from a narrow LF component, whereas in the SOC regime when ITG dominates, a much wider BB component exists and the LF component merges into the BB component.

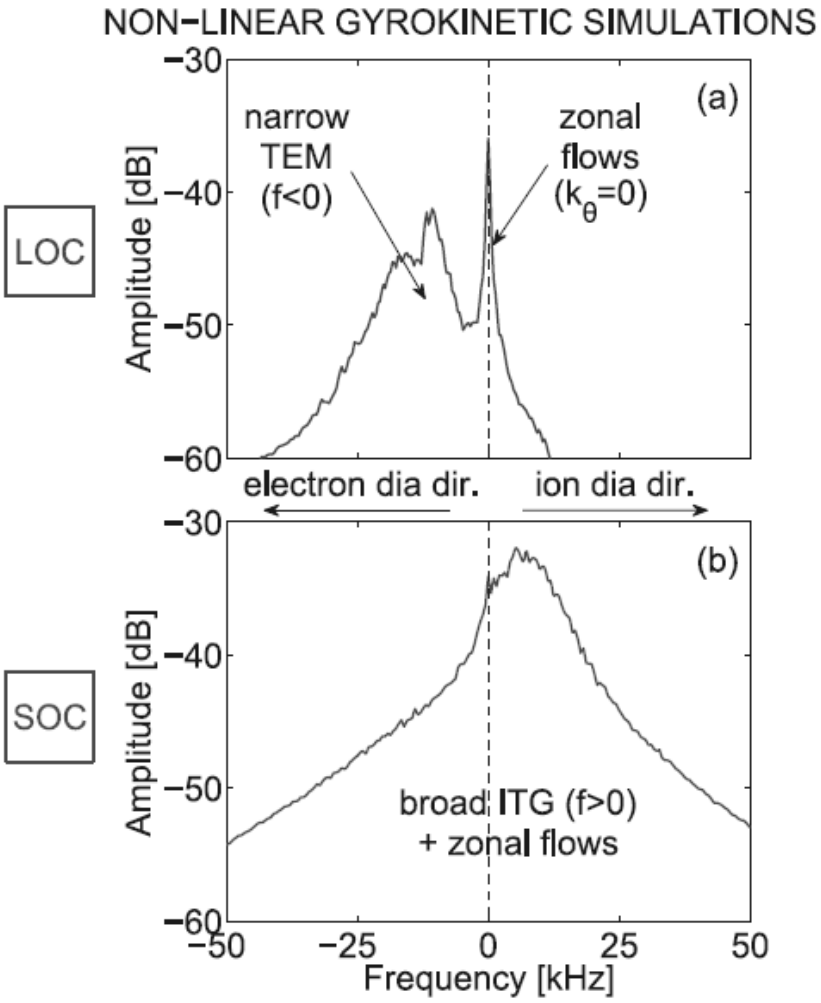

Figure 6.5: Density fluctuation spectra by gyrokinetic simulations in Tore Supra discharge #48102 at $\rho = 0.37$ for (a) the LOC and (b) the SOC regime. Reprinted from Refs [Arnichand 2016], copyright owned by IOP Publishing.

To support this interpretation, we have studied the radial profiles of the LF width (W_{LF}) in the LOC and SOC regimes, as shown in figure 6.6. It is clear that W_{LF} in the SOC regime is systematically higher than in the LOC regime at all radial positions. Specifically, at the center inside the $q = 1$ surface, the LF width in the SOC regime ($\sim$ 8 kHz) is approximately two times the width in the LOC regime ($\sim$ 4 kHz). However, the estimate of W_{LF} from our parametrization technique might be less reliable when the BB contribution is high. From figure 5.9, outside the central basin, i.e. outside the $q = 1$ surface, E_{BB} may reach a value of 0.5 (HFS) or close to 1 (LFS). Accordingly, when E_{BB} is close to 1, most of the energy is in the BB component and the LF component disappears or merges with the BB component, rendering the fit of the LF component, and thus W_{LF}, unstable. Therefore, we focus only on the HFS and the core region, where E_{BB} is not close to 1 (saturation) and thus W_{LF} is more reliable.

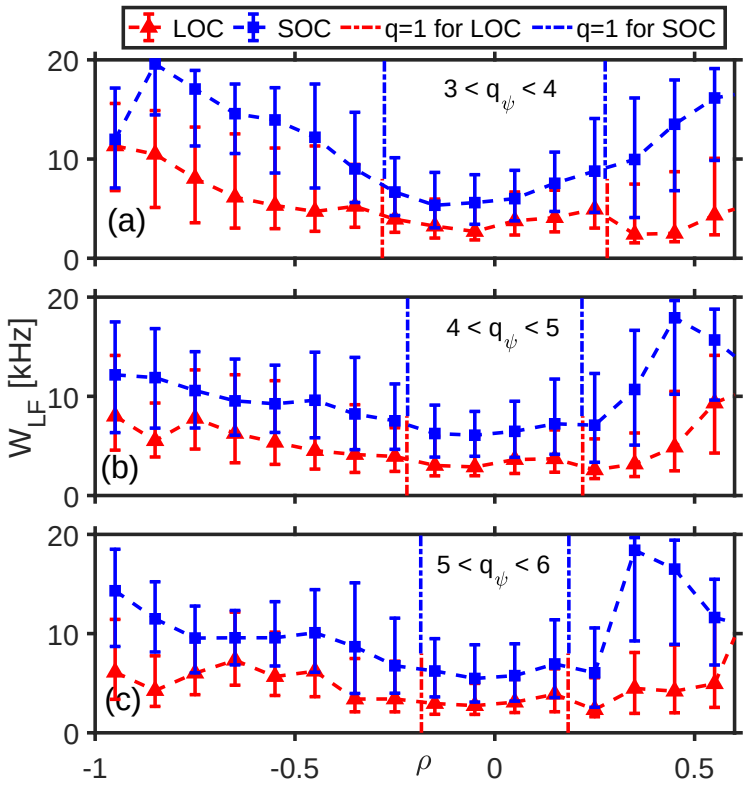

Figure 6.6: Median radial profiles of the LF width W_{LF} at different ranges of the edge safety factor (q_ψ) in the LOC and SOC regimes.

Figures 6.7 (a) and (b) show the dependence of the LF width (W_{LF}) on ν_{eff} at the HFS ($\rho = -0.4$) and at the center ($\rho = 0$), respectively. At the center (figure 6.7 (b)), W_{LF} increases slowly with ν_{eff} in both LOC and SOC regime, with the weakest slope in SOC. As far as the LF magnitude is concerned, most of W_{LF} in the LOC regime is around or below 5 kHz, whereas W_{LF} in the SOC regime could be near 10 kHz, which is consistent with the systematic observations near the core region in figure 6.6. However, note that the trends are difficult to extract due to the strong dispersion of the data points, especially during the transition regime. This strong data dispersion is also observed at

the HFS (figure 6.7 (a)), where a much faster increase of W_{LF} with ν_{eff} seems to exist.

The generally observed increasing trends of the LF width, as the confinement regime changes from LOC to SOC in figures 6.6 and 6.7, are consistent with the GENE simulations in figure 6.5. This supports the interpretation that the observed changes of the BB component in the frequency spectra can be induced by a change of dominating instability from TEM to ITG.

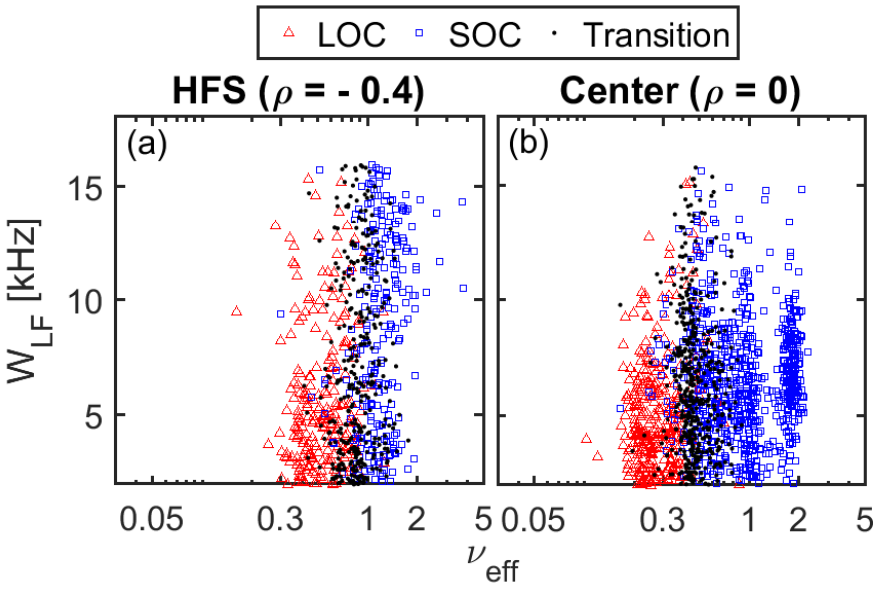

Figure 6.7: LF width (W_{LF}) vs. effective collisionality (ν_{eff}) in the LOC, SOC and transition regimes at (a) the HFS ($\rho = -0.4$), (b) the plasma center inside the basin ($\rho = 0$).

6.2 Frequency spectrum in plasmas with auxiliary power

After studying the change of spectral characteristics with collisions in Ohmic plasmas, the nest step is to study the spectral characteristics with additional heating power.

6.2.1 Dependence of BB component on collisionality

To better understand the different levels of E_{BB} in L-mode with ICRH or LH heating, the dependence of E_{BB} on effective collisionality has been analyzed as well. Calculations of ν_{eff} are more complicated in L-mode, because measurements of Z_{eff} from bremsstrahlung spectroscopy can be less reliable in Tore Supra LH discharges, reaching very large values ($\gtrsim 6$). It was previously reported that hot spots on the inner wall, supra-thermal electrons and influence of reflections may cause overestimation of Z_{eff} in Tore Supra LH plasmas. [Schunke 2005] Therefore, a robust multi-machine scaling law [Matthews 1997] has been

used to obtain Z_{eff} in LH plasmas:

$$Z_{\text{eff}} = 1 + 7\frac{P_{\text{rad}}}{Sn_l^2}, \tag{6.1}$$

Here, P_{rad} is the total radiated power in MW, $S = 4\pi^2 Ra$ the plasma surface area in m^2 and n_{l} the line-averaged density in 10^{-20} m^{-3}, all available in the database. In ICRH plasmas the problem is less severe, but the scaling law has also been used in this case to maintain consistency with the LH case.

6.2.1.1 BB contribution

Figure 6.8 shows a plot of E_{BB} on ν_{eff} at different ρ. The value of ν_{eff} is systematically lower here than in Ohmic plasmas, due to the higher T_{e} with additional heating. Inside the central basin (figure 6.8 (b)), the LH plasmas dominate in the low ν_{eff} ranges. In this region, most of E_{BB} in LH plasmas remains at a low level (~ 0.2) for $\nu_{\text{eff}} < 0.3$, when Ohmic plasmas are in LOC regime (figure 6.2 (b)). The ICRH plasmas dominate in the higher ν_{eff} ranges and most of E_{BB} in ICRH is above 0.5 with strong dispersion. Regardless of the heating method, the general increasing trend of E_{BB} with ν_{eff} observed in Ohmic plasmas is recovered, not only inside but also outside the basin. Furthermore, at the LFS (figure 6.8 (c)), E_{BB} in LH, and probably also ICRH, is close to saturation at large ν_{eff}, while at the HFS (figure 6.8 (a)) saturation of E_{BB} only occurs with ICRH. It should be noted that relatively few plasmas are available in the database with ICRH at the LFS (figure 6.8 (c)), somewhat degrading the reliability of the results under these conditions. This is due to a lack of valid spectra caused by a strong Doppler effect, which often affects the spectra towards the LFS.

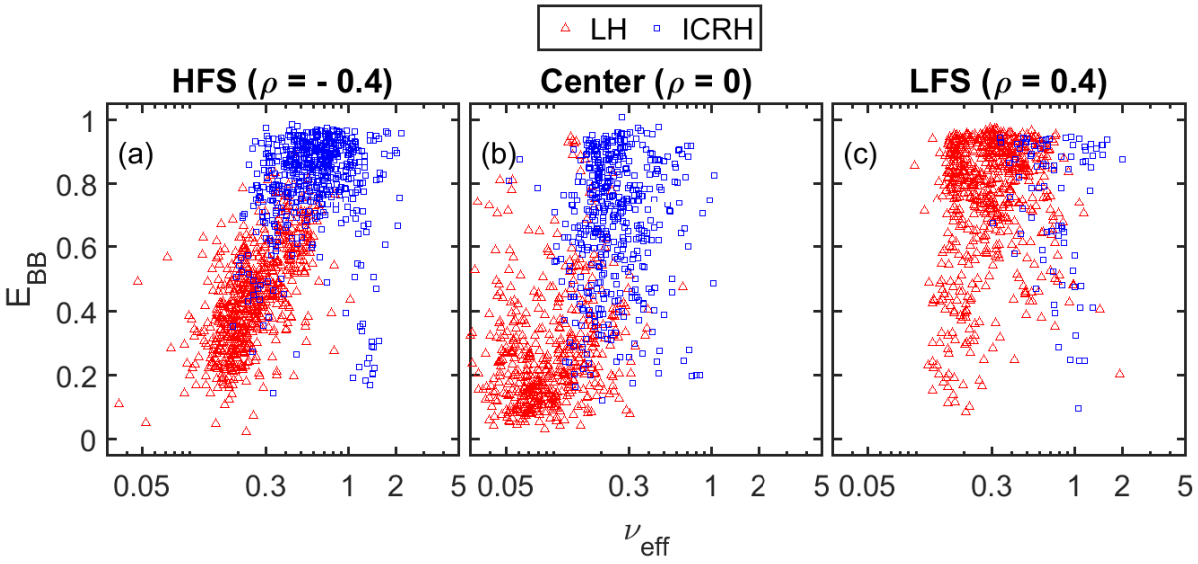

Figure 6.8: Broadband contribution (E_{BB}) vs. effective collisionality (ν_{eff}) in L-mode with pure ICRH or LH at different positions. Only plasmas with moderate heating power (1 MW $< P_{\text{heat}} <$ 3 MW) are shown.

Following the discussion in the Ohmic cases, the trend of the corrected E_{BB} with ν_{eff} has also been studied, shown in figure 6.9. Similar trends as in figure 6.8 are observed at different positions. However, the systematically higher magnitude of the BB contribution at the LFS, compared to the HFS, can be deduced from the corrected E_{BB} but not from E_{BB}. Most notably, the possible decreasing trend at high ν_{eff} at the LFS (figure 6.9 (c)) is more clear compared with figure 6.3 (c), although this needs to be investigated in more detail.

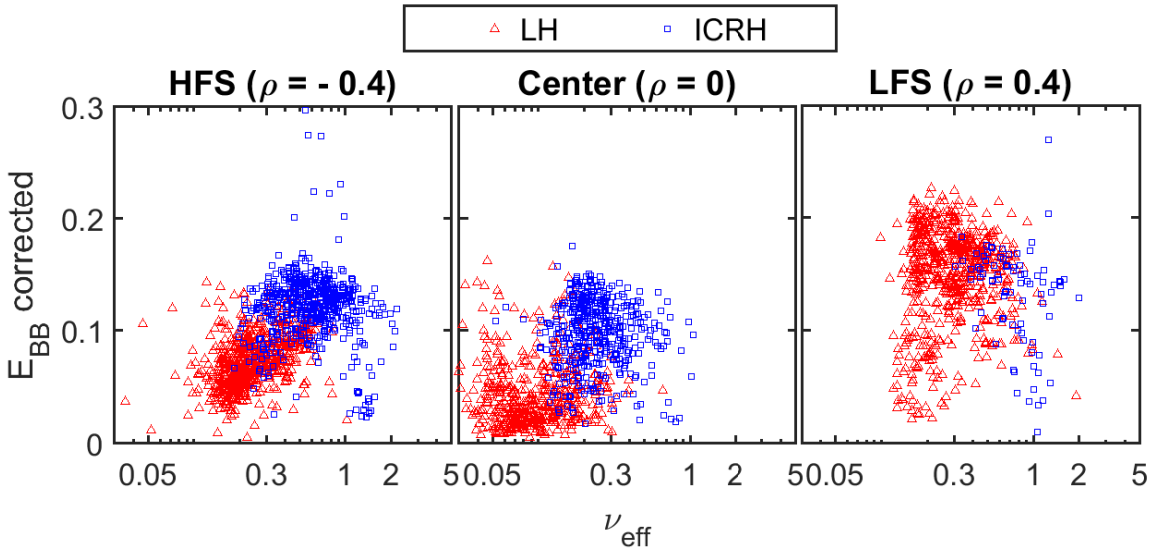

Figure 6.9: Corrected E_{BB} vs. effective collisionality (ν_{eff}) in L-mode with pure ICRH or LH at different positions. Only plasmas with moderate heating power (1.5 MW $<$ P_{heat} $<$ 2.5 MW) are shown.

6.2.1.2 BB width and shape

We next study the dependence of the broadband width W_{BB} and shape β_{BB} on collisionality with ICRH and LH. Figure 6.10 (a–c) shows the dependence of W_{BB} on ν_{eff} at different ρ. In contrast to the Ohmic case, a relatively clear increasing trend of W_{BB} can be observed with ν_{eff} in LH plasmas. For the ICRH plasmas, operating at higher ν_{eff}, no clear trends of W_{BB} with ν_{eff} can be observed at the HFS. Moreover, in absolute terms, the scatter of W_{BB} appears to be lower with LH than ICRH. Another noticeable feature of W_{BB} lies in a systematic increase from inside the basin towards the HFS or LFS. This feature is the most pronounced with ICRH, where W_{BB} increases from around 100 kHz to 150 kHz and above.

Likewise, figure 6.10 (d–f) shows the evolution of β_{BB} from the generalized Gaussian model with ν_{eff}, with ICRH or LH at different ρ. Similar to the Ohmic case, in the plasma center at lower collisionalities, corresponding to LH heating, the dispersion of β_{BB} is larger than with ICRH heating. Indeed, at higher ν_{eff}, the β_{BB} values cluster around $\sim$ 1 (double exponential). In addition, like the width, the shape parameter in ICRH plasmas tends to be higher outside the basin than inside.

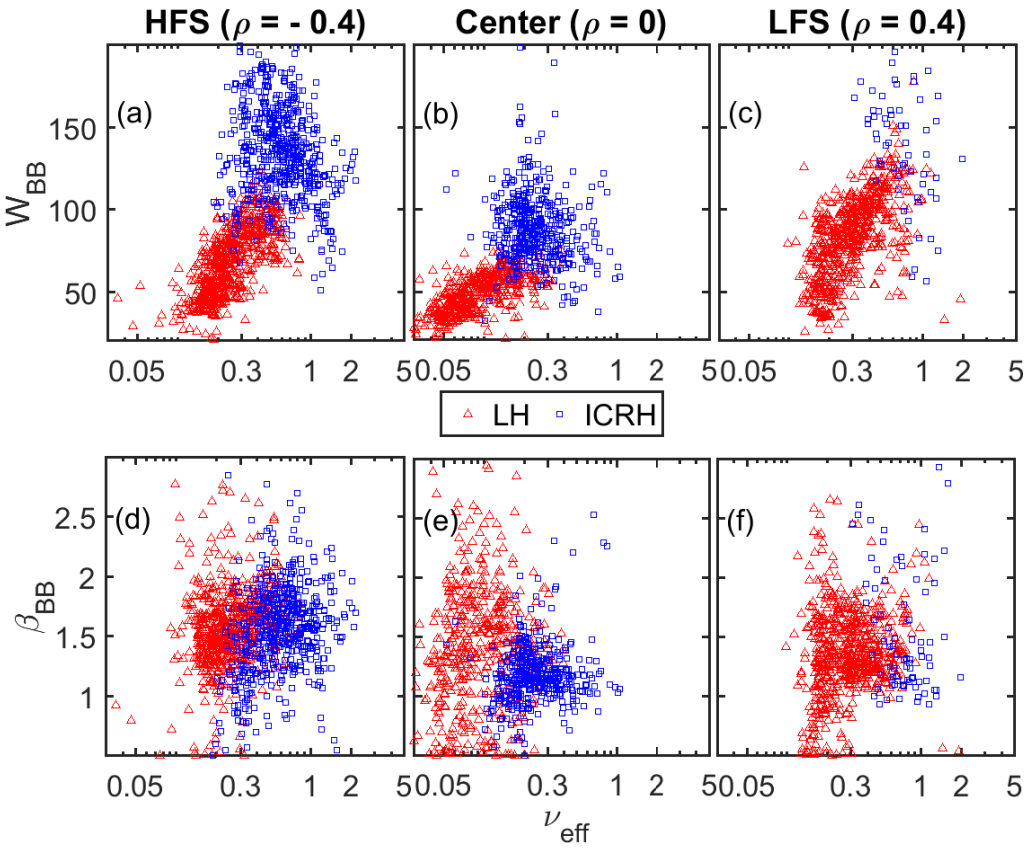

Figure 6.10: Same as figure 6.8 for the trend of the broadband width W_{BB} (a–c) and shape β_{BB} (d–f).

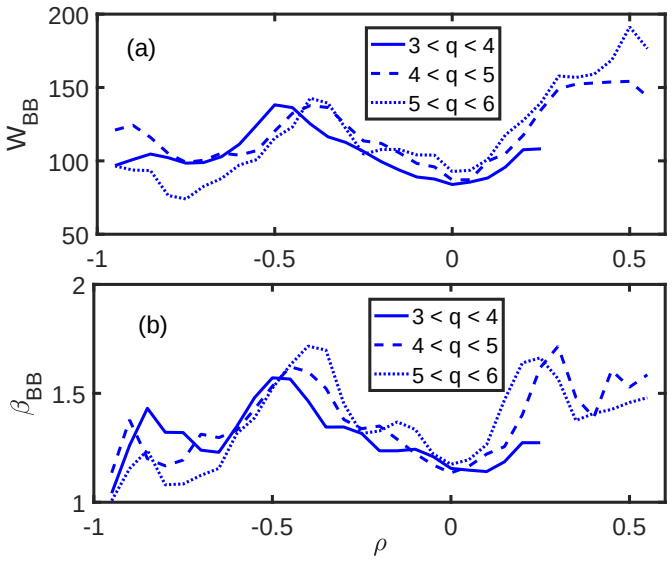

Figure 6.11: Radial profiles of (a) BB width (W_{BB}) and (b) shape (β_{BB}) with ICRH. Here, median values are plotted based on small radial intervals ($\delta\rho = \pm 0.05$), leaving out intervals with insufficient points.

To further investigate the observed radial trends of W_{BB} and β_{BB} in L-mode, especially the systematic change with ICRH when inside or outside the basin, the radial profiles of W_{BB} and β_{BB} in ICRH plasmas at different q_ψ are shown in figure 6.11 (a) and (b), respectively. These are median profiles calculated from all relevant plasmas in the database. In figure 6.11 (a), W_{BB} exhibits a local minimum inside the central basin. At the HFS around $\rho \sim -0.3$ to -0.6, W_{BB} shows a bump structure, which is shifted towards the plasma center with increasing q_ψ ranges, whereas saturation occurs at the LFS. This corresponds to the observations in figure 6.10 (d–f). Since W_{BB} is related to the plasma rotation, the bump structure could be linked to a change of rotation velocity shear at the HFS, although this needs further investigation. A similar bump structure and its relation to q_ψ ranges occurs for the radial profiles of β_{BB}, as shown in figure 6.11 (b).

6.2.2 Trends for the LF component

We have also investigated the radial profiles of the LF width (W_{LF}) with ICRH and LH at different ranges of q_ψ, as shown in figure 6.12. It is clear that W_{LF} with ICRH is systematically higher than with LH at almost all radial positions. Specifically, W_{LF} with LH is usually around 5 kHz, whereas W_{LF} with ICRH is close to 20 kHz (saturation) for most of the situations. Note that the saturation of W_{LF} is an artifact of the fitting procedure, reaching the upper constraint of 20 kHz on W_{LF}. This constraint cannot be relaxed, however, to allow distinguishing between the BB and LF components.

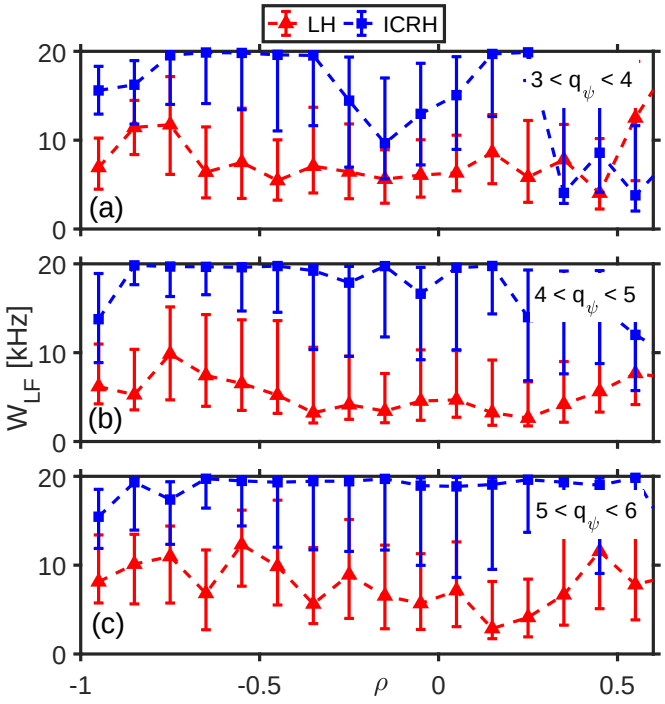

Figure 6.12: Median radial profiles of the LF width (W_{LF}) at different range of the edge safety factor (q_ψ) with ICRH and LH.

However, as mentioned before, when B_{LF} is close to 1 or when W_{LF} is close to 20 kHz, the LF component may disappear or merge with the BB component. This degrades the reliability of the observed W_{LF} and therefore these circumstances should be avoided. So, when studying the dependence of W_{LF} on ν_{eff}, these less reliable results are removed by setting $W_{LF} < 0.6$ and $W_{LF} < 16$ kHz. Moreover, we have only focused on the HFS and the core region to avoid the strong saturation occurring at the LFS, as shown in figure 6.13. At the HFS (figure 6.13 (a)), an increasing trend can be observed, although strong scattering of the data points at fixed ν_{eff} occurs. The data is even more scattered in the center (figure 6.13 (a)), possibly with a very weak increasing trend of W_{LF} with ν_{eff}. However, some low W_{LF} data exist at high ν_{eff} in ICRH plasmas, which clearly deviate form the main trend. We have not been able to explain these exceptions, and a deeper shot-to-shot analysis will be required.

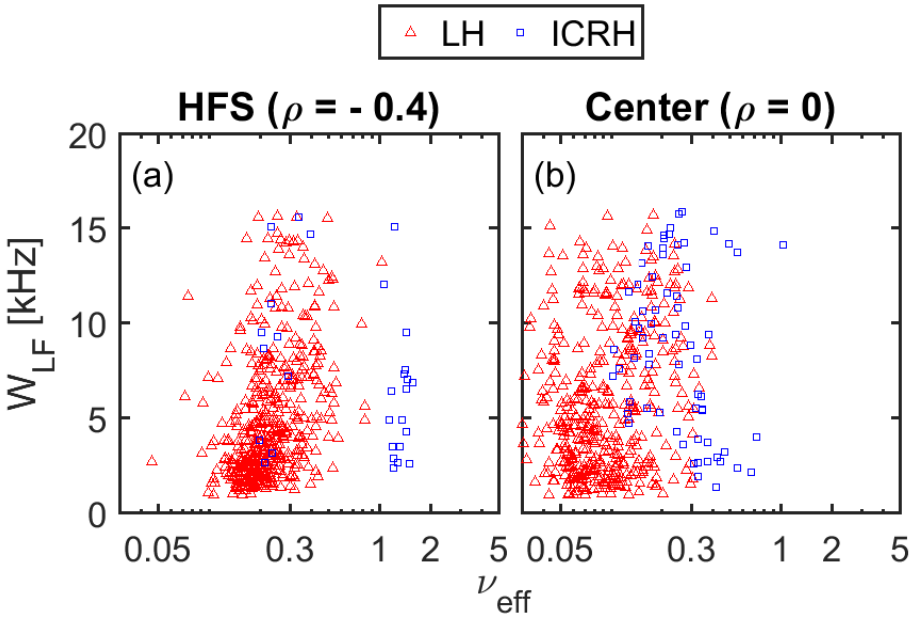

Figure 6.13: LF width (W_{LF}) vs. effective collisionality (ν_{eff}) in L-mode with pure ICRH or LH at (a) the HFS and (b) the plasma center. Only plasmas with moderate heating power (1.5 MW $< P_{heat} <$ 2.5 MW) are shown.

6.2.3 Density peaking

Figure 6.14 shows the density peaking with respect to the effective collisionality. The density peaking increases slowly with ν_{eff} at lower ν_{eff}, corresponding almost exclusively to LH-heated discharges, reaching a maximum value at about $\nu_{eff} \sim 0.1$. At higher ν_{eff} (> 0.1), the density peaking decreases rapidly with ν_{eff}, corresponding mostly to ICRH discharges. The dependence of density peaking on ν_{eff} is thus very similar to the trends observed in the Ohmic case (figure 6.1), expect that the slope at low ν_{eff} is much flatter in LH discharges than in the LOC regime.

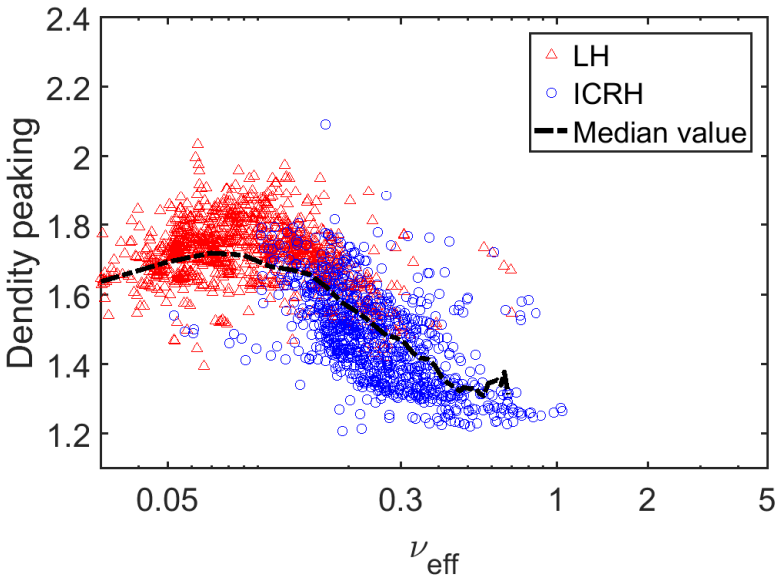

Figure 6.14: Density peaking factor vs. effective collisionality in L-mode.

6.2.4 Interpretation

Given the similarity of the observed trends of E_{BB} in terms of ν_{eff} with ICRH or LH, compared to the Ohmic case, one possible explanation is again offered by the stabilization of the TEM instabilities with increasing collisionality. At high collisionality, this would result in discharges where the turbulence would be driven mostly or exclusively by ITG instabilities. The decrease of the density peaking (figure 6.14) with ν_{eff} above 0.1 supports this interpretation. Below this threshold, the density peaking increases with ν_{eff}, but the slope is weaker than in the Ohmic case (figure 6.1). This might be explained by the current driven by LH waves, reducing the toroidal electric field E_ϕ. Another explanation could be that the turbulence is due to a mix of TEM and ITG instabilities at low ν_{eff} below the threshold. The decrease of the density peaking with ν_{eff} for ITG turbulence would reduce the slope at low ν_{eff} as observed in the LOC regime (figure 6.1).

As for the BB width (W_{BB}), attempts have been made in the past to connect the width and shape of frequency spectra to the underlying instability, both from the theoretical and experimental viewpoints. [Romanelli 1989, Mattor 1992, Watts 1996]. With the extensive spectrum database, we have identified an increasing trend of the BB width in terms of collisionality in L-mode plasmas with ICRH or LH heating, although no such general trends has been observed in the Ohmic case. The BB width could be linked to both turbulence properties and toroidal intrinsic rotation. In terms of the latter mechanism, one might expect a decrease of W_{BB} with increasing collisionality, as the main location where the power is deposited moves outward. The fact that, on the contrary, an increasing trend is observed for the LH plasmas in this database study (figure 6.10), could indicate an unknown link between the BB width and the underlying instabilities. The net effect could be the result of a competition between multiple mechanisms. Therefore, the link between the spectral width of the fluctuation measurements and the turbulence properties

or instabilities remains an open question. Note that also the broadband shape could be an important factor in a systematic study, due to its connection with the BB width. Although only weak trends have been observed for the BB shape for both Ohmic and L-mode plasmas (not shown here), other or additional plasma parameters might be used to simultaneously explain the BB width and shape in future work.

6.3 Discussion and perspectives

In this chapter, we have studied trends of the BB component with collisionality in both Ohmic and L-mode plasmas with ICRH or LH. We have proposed a possible transition of the dominating instability to explain the observations, supported by earlier gyrokinetic simulations and a study of the density peaking and the LF component.

To put the proposed interpretation on firmer ground, one would need to identify a number of discharges in the database that are sufficiently diagnosed to enable transport analysis with a view to validated profiles of density, temperature, current and impurity concentrations. Then, quasi-linear gyrokinetic simulations with the QuaLiKiz code [Bourdelle 2007] or with gyrokinetic codes such as GENE could be performed to compute the growth rates of the different instabilities and deduce the dominant ones. In a next step, ones would perform nonlinear gyrokinetic simulations to obtain density fluctuation maps. Full-wave reflectometry simulations could then be run to obtain frequency fluctuation spectra that could be compared to the experimental measurements.

The trends that have been observed through the present database study, in combination with an efficient spectrum parametrization, must be confirmed through simulations and dedicated experiments, taking into account that some circumstances have changed with the upgrade from Tore Supra to the WEST tokamak. Furthermore, there are many ways in which the present study could be improved. The strong dispersion of the data suggests that dependencies on additional plasma parameters may need to be taken into account to characterize trends of the fluctuation spectra. On the other hand, while the individual parameters used to characterize each spectrum may be interpreted from the physical point of view, each of them only quantifies a certain aspect of the spectrum. The parametrization method could be augmented with modern techniques from data science, enabling a more integrated quantification of shapes and distributions [Shabbir 2016]. Combined with advanced regression analysis, this could contribute to systematic studies of the characteristics of micro-instabilities in terms of varying plasma conditions. Equipped with a similarity measure between frequency spectra, classification techniques could help discriminating between turbulent regimes based on the shape of their spectra.

Chapter 7

Conclusions and perspectives

7.1 Conclusions and discussion

In this PhD thesis, a robust reflectometry spectrum parametrization method has been developed for systematic studies of turbulence properties in fusion plasmas. Equipped with a routinely applicable spectrum parametrization technique, we have been able to study trends of several spectrum characteristics that occur robustly throughout significant parts of the database. Some of these patterns were only revealed with the availability of large data sets spanning a wide range of plasma conditions. In turn, a physical interpretation for the observed patterns has been proposed in terms of a transition between the dominant instability driving the turbulence. This interpretation may be compatible with earlier simulations and experiments performed on a limited set of discharges. Our work has allowed, for the first time in fusion science, to systematically characterize trends of fluctuation properties over a large database. This large-scale approach is complementary to the traditional analysis methods on the basis of a limited number of key discharges. Our work is intended to open the way to a new, standardized method for studying plasma density fluctuations (δn) from a systematic viewpoint.

The spectrum parametrization method has been developed using a large database with 350,000 frequency spectra obtained from Tore Supra plasmas. The method is also useful for quantifying the power spectrum in individual discharges, and can be easily adapted to other fusion devices or other research domains relying on quantitative comparison of spectra. The main contribution of the technique is that it allows quantification of spectra in a standardized way, enabling comparison across experimental conditions and devices. In fitting the spectra with a reduced model, the generalized Gaussian, Voigt, and Taylor distributions have been used to parameterize the various components of the fluctuation power spectra. Both the generalized Gaussian and the Taylor models yield excellent performance in terms of goodness-of-fit, while meeting the requirements of flexibility, discrimination, and robustness. The Taylor model is a more convenient model with a view to physical interpretation. In implementing the fitting routine, the cost function, the constraints and the initial guesses have been identified as critical points. The cost function consists of equally weighted components on the linear and logarithmic scale, imposing several constraints on the parameters in order to separate the different spectrum components.

Full radial profiles of the broadband (BB) contribution (E_{BB}) of the frequency spectra have been studied for different edge safety factors (q_ψ). In Ohmic plasmas, an remarkable drop of E_{BB}, called the E_{BB} basin, was systematically observed inside the $q = 1$ surface. The basin width is clearly linked to the position of the $q = 1$ magnetic surface. Outside

the $q = 1$ surface at both the high-field-side (HFS) and low-field-side (LFS), E_{BB} reaches a high magnitude ($E_{\mathrm{BB}} > 0.5$) but a strong asymmetry occurs of the E_{BB} trend with radius at the HFS vs. the LFS. In addition, a systematic shift of the cutoff layers to the HFS is probably caused by underestimation of the electron density in the core region by the interferometry diagnostic. Furthermore, similar trends were recovered when discriminating between the linear confinement regime (LOC) and the saturated confinement regime (SOC). However, E_{BB} was observed to be systematically higher in the SOC regime, compared to the LOC regime. In L-mode plasmas, with auxiliary ICRH or LH heating, E_{BB} with pure LH heating remains at almost the same level as in Ohmic plasmas, and only a small increase of E_{BB} could be observed with increasing power. In contrast, with ICRH heating, E_{BB} was significantly higher than in the Ohmic case, even at low heating power, saturating at high heating power. The E_{BB} basin in the core region is very shallow or even non-existent with ICRH heating. Moreover, increasing q_ψ generally causes a small increase of E_{BB} for both ICRH and LH plasmas.

The global trends of the E_{BB} profiles observed in both the Ohmic and L-mode plasmas agree with results from the literature regarding the behavior of density fluctuations in various confinement regimes. Our work has extended the validity of these results to a much wider range of plasma conditions. Indeed, E_{BB} is possibly proportional to the density fluctuation level when it is small ($E_{\mathrm{BB}} < 0.5$), whereas this linear relation becomes invalid at larger E_{BB}. A correction of E_{BB} considering the density gradient length and the frequency of the probing waves may provide a more accurate estimate for the density fluctuation level, but doing this for the whole database is infeasible.

The effective collisionality (ν_{eff}) has been found to have a crucial impact on the various components of the frequency spectra. For the BB component, a general increasing trend of E_{BB} with respect to ν_{eff} has been observed at different radial positions for both Ohmic and L-mode plasmas. The general trends of the BB width (W_{BB}) and shape (β_{BB}) are usually more difficult to extract, except for W_{BB} in L-mode plasmas, where an increase of W_{BB} with ν_{eff} was observed systematically across the radius. The pattern of β_{BB} is similar for Ohmic and L-mode plasmas. Usually, the dispersion of the data becomes strongest at a moderate ν_{eff} and β_{BB} tends to converge to the value of 1 (heavy-tailed Laplacian) at high ν_{eff}. Regarding the low-frequency (LF) component, a weakly increasing trend of the LF width (W_{LF}) was observed at the HFS and at the center for both Ohmic and L-mode plasmas.

The observed dependence of E_{BB} on ν_{eff} indicates a possible link between the spectrum and the underlying instability driving the turbulence. This assumption was supported by earlier GENE simulations, showing much wider BB and LF components in the SOC regime, with a reduced TEM instability. The systematic trend in W_{LF} supports this interpretation, together with our analysis of the density peaking. For both Ohmic and L-mode plasmas, density peaking increases with ν_{eff} at low ν_{eff} and decreases at high ν_{eff}. Thus, the observed trends seem to be compatible with a transition of the dominating instability from TEM to ITG.

A useful byproduct of our database approach is the ability to detect faults in diagnostics, possibly indicated by off-normal clusters or trends, or outliers in the database.

Other unusual patterns might be due to specific experimental conditions, but may also point at interesting physics, to be explored in a more detailed analysis on a limited data set.

Concluding, the systematic trends observed in this PhD work confirm the relevance of the database approach. Ongoing developments in artificial intelligence are rapidly impacting a broad variety of scientific domains. Likewise, in fusion science, such developments may well lead researchers to new discoveries and a deeper understanding of the fusion plasma.

7.2 Perspectives

Since this thesis is the first systematic analysis of complicated turbulence measurements in fusion study, it has opened windows for many research directions. We now discuss perspectives to future work, following the achievements described in the present thesis.

Extension of this thesis

Tore Supra operated until 2011, when the transition to the new WEST tokamak was started. In WEST, the poloidal cross-section of the plasma was changed to the more modern D-shape, as shown in figure 7.1. Equipped with a new divertor and with auxiliary ICRH and LH heating, realisation of the H-mode is anticipated. The new plasma shape and parameters make it possible to carry out a systematic comparison of turbulence properties between Tore Supra and WEST. Because in WEST the magnetic ripple in the edge has been reduced to much lower levels compared to Tore Supra, it may become possible to extend the spectral analysis to the edge region. Furthermore, it is possible to extend the study to Doppler reflectometer, other diagnostic systems, or even other devices with proper adaption. In addition, influence of the instrumental configuration like the radiation pattern of antennas can also be investigated.

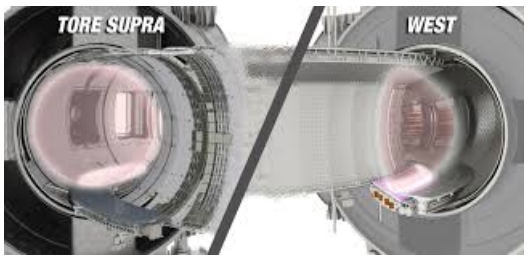

Figure 7.1: From the circular cross-section limiter Tore Supra to the D-shape cross-section divertor WEST (Tungsten (W) Environment in Steady-state Tokamak).

Data analysis capabilities

There are also many ways in which the data analysis techniques applied in the present study could be improved. The strong dispersion of the data suggest that additional

plasma parameters may have to be employed to better order the data and characterize trends of the fluctuation spectra. On the other hand, while the individual parameters used to characterize each spectrum may be interpreted from a physical point of view, each of them only quantifies a certain aspect of the spectrum. Modern data science has developed techniques for quantifying distributions and shapes in a more integrated way [Shabbir 2016]. Combined with specialized similarity measures between shapes or distributions, a more faithful comparison between spectra would become feasible. In turn, this could also contribute to more significant patterns in the data.

Additional spectrum components

As mentioned in Chapter 4, to focus on the most important characteristics of the frequency spectra, only the most common components (DC, LF, BB and N) have been considered in the parametrization. Neglecting other components with narrow bandwidth does not affect the reported general trends of the identified components. However, it might be envisaged to add more parameters to enable capturing also other components, notably the QC modes. This might help to strengthen the link between the spectra and the dominating micro-instabilities, and to explore additional physical properties of the turbulent fluctuations. Specifically, the QC modes could be fitted by another Gaussian functions, with different amplitude for the negative and positive QC modes. Combined with the GG or Taylor model developed in Chapter 4, the improved model would include 15 parameters to characterize the spectra with QC modes, as shown in figure 7.2.

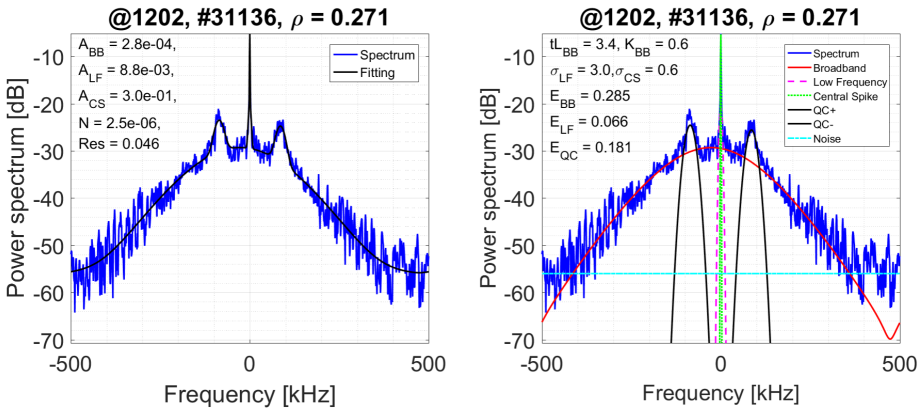

Figure 7.2: Include another 4 parameters to fit the quasi-coherent (QC) mode in spectra.

With the increased number of parameters, the problem of misfit or overfit might become more severe, especially when the amplitude of the QC modes is weak compared to the BB component and thus are difficult to be detected. Therefore, a robust fitting algorithm would need to include appropriate constraints on the fit parameters. Another approach could be to dynamically adapt the number of parameters (or functions) according to the spectral characteristics. Here as well, machine learning techniques could make a valuable contribution by clustering the spectra with QC modes into different categorise according to the intensity of the QC modes.

Application to coherence spectra

In this thesis only the parametrization of the power spectra has been discussed. The coherence spectra from radial or poloidal correlation measurements could provide more spatial and temporal characteristics of turbulent eddies, which cannot be obtained from the power spectra. The features and components of coherence spectra could in general be different from those of power spectra. In tokamak plasmas, the uncorrelated BB component could disappear in coherence spectra. In addition, the LF component could also disappear in long-range correlation analysis [Krämer-Flecken 2015]. Therefore, when fitting the different components of the coherence spectra with parameterized functions, the number of functions should be adapted depending on experimental conditions.

Bibliography

[Abas 2015] N. Abas, A. Kalair and N. Khan. *Review of fossil fuels and future energy technologies.* Futures, vol. 69, pages 31 – 49, 2015.

[Acheson 1990] D. J. Acheson. *Elementary Fluid Dynamics.* Oxford University Press, 1990.

[Agbossou 2004] K. Agbossou, M. Kolhe, J. Hamelin and T. K. Bose. *Performance of a stand-alone renewable energy system based on energy storage as hydrogen.* IEEE Transactions on Energy Conversion, vol. 19, no. 3, pages 633–640, 2004.

[Akella 2009] A.K. Akella, R.P. Saini and M.P. Sharma. *Social, economical and environmental impacts of renewable energy systems.* Renewable Energy, vol. 34, no. 2, pages 390 – 396, 2009. Renewable Energy for Sustainable Development in the Asia Pacific Region.

[Amador 2018] C.H.S. Amador, R. Sabot, X. Garbet, Z.O. Guimar aes Filho and J.-H. Ahn. *Determination of q during sawtooth from inverse evolution of BAEs in Tore Supra.* Nuclear Fusion, vol. 58, no. 1, page 016010, 2018.

[Angioni 2003] C. Angioni, A. G. Peeters, G. V. Pereverzev, F. Ryter and G. Tardini. *Theory-based modeling of particle transport in ASDEX Upgrade H-mode plasmas, density peaking, anomalous pinch and collisionality.* Physics of Plasmas, vol. 10, no. 8, pages 3225–3239, 2003.

[Angioni 2005] C. Angioni, A. G. Peeters, F. Ryter, F. Jenko, G. D. Conway, T. Dannert, H. U. Fahrbach, M. Reich, W. Suttrop and L. Fattorini. *Relationship between density peaking, particle thermodiffusion, Ohmic confinement, and microinstabilities in ASDEX Upgrade L-mode plasmas.* Physics of Plasmas, vol. 12, page 040701, 2005.

[Angioni 2009] C Angioni, E Fable, M Greenwald, M Maslov, A G Peeters, H Takenaga and H Weisen. *Particle transport in tokamak plasmas, theory and experiment.* Plasma Physics and Controlled Fusion, vol. 51, page 124017, 2009.

[Arnichand 2014] H. Arnichand, R. Sabot, S. Hacquin, A. Krämer-Flecken, X. Garbet, J. Citrin, C. Bourdelle, G. Hornung, J. Bernardo, C. Bottereau, F. Clairet, G. Falchetto and J.C. Giacalone. *Quasi-coherent modes and electron-driven turbulence.* Nuclear Fusion, vol. 54, no. 12, page 123017, 2014.

[Arnichand 2015] Hugo Arnichand. *Identification of Trapped Electron Modes in Frequency Fluctuation Spectra of fusion plasmas.* Ph.D. dissertation, Aix-Marseille University, 2015.

[Arnichand 2016] H Arnichand, J Citrin, S Hacquin, R Sabot, A Krämer-Flecken, X Garbet, C Bourdelle, C Bottereau, F Clairet, J C Giacalone, Z O Guimar aes Filho, R Guirlet, G Hornung, A Lebschy, P Lotte, P Maget, A Medvedeva, D Molina, V Nikolaeva, D Prisiazhniuk, the Tore Supra and the ASDEX Upgrade teams. *Identification of trapped electron modes in frequency fluctuation spectra.* Plasma Physics and Controlled Fusion, vol. 58, no. 1, page 014037, 2016.

[Artsimovich 1972] L.A. Artsimovich. *Tokamak devices.* Nuclear Fusion, vol. 12, no. 2, page 215, 1972.

[Arunasalam 1990] V. Arunasalam, N.L. Bretz, P.C. Efthimion, R.J. Goldston, B. Grek, D.W. Johnson, M. Murakami, K.M. McGuire, D.A. Rasmussen, F.J. Stauffer and J.B. Wilgen. *Self-consistency of the principle of profile consistency results for sawtoothing tokamak discharges.* Nuclear Fusion, vol. 30, no. 10, page 2111, 1990.

[Bibet 2001] Ph Bibet, A Ekedahl, Ph Froissard, F Kazarian, E Bertrand, S Dutheil and L Tanaskovic. *Coupling and power handling of the new Tore Supra LHCD launcher.* Fusion Engineering and Design, vol. 56-57, pages 679 – 684, 2001.

[Bittencourt 2004] J.A. Bittencourt. *Fundamentals of Plasma Physics*, 3rd edition. Springer, 2004.

[Blanco 2013] E Blanco and T Estrada. *Two-dimensional full-wave simulations of radial correlation Doppler reflectometry in linear and non-linear regimes.* Plasma Physics and Controlled Fusion, vol. 55, no. 12, page 125006, nov 2013.

[Bolsunovsky 2011] A. Bolsunovsky and D. Dementyev. *Evidence of the radioactive fallout in the center of Asia (Russia) following the Fukushima Nuclear Accident.* Journal of Environmental Radioactivity, vol. 102, no. 11, pages 1062 – 1064, 2011.

[Bottollier-Curtet 1987] H. Bottollier-Curtet and G. Ichtchenko. *Microwave reflectometry with the extraordinary mode on tokamaks: Determination of the electron density profile of Petula-B.* Review of Scientific Instruments, vol. 58, page 539, 1987.

[Bourdelle 2005] C Bourdelle. *Turbulent particle transport in magnetized fusion plasma.* Plasma Physics and Controlled Fusion, vol. 47, page A317, 2005.

[Bourdelle 2007] C. Bourdelle, X. Garbet, F. Imbeaux, A. Casati, N. Dubuit, R. Guirlet and T. Parisot. *A new gyrokinetic quasilinear transport model applied to particle transport in tokamak plasmas.* Physics of Plasmas, vol. 14, page 112501, 2007.

[BP 2017] BP. *Statistical Review of World Energy.* BP p.l.c., 2017.

[Bretz 1997] N. Bretz. *Diagnostic instrumentation for microturbulence in tokamaks.* Review of Scientific Instruments, vol. 68, no. 8, pages 2927–2964, 1997.

[Buttery 2000] R J Buttery, S Günter, G Giruzzi, T C Hender, D Howell, G Huysmans, R J La Haye, M Maraschek, H Reimerdes, O Sauter, C D Warrick, H R Wilson and H Zohm. *Neoclassical tearing modes.* Plasma Physics and Controlled Fusion, vol. 42, no. 12B, page B61, 2000.

[Casati 2009] A. Casati. *A quasi-linear gyrokinetic transport model for tokamak plasmas.* PhD thesis, University of Provence, 2009.

[Chapman 2011] I T Chapman. *Controlling sawtooth oscillations in tokamak plasmas.* Plasma Physics and Controlled Fusion, vol. 53, no. 1, page 013001, 2011.

[Chen 2006] Francis F. Chen. *Introduction to Plasma Physics and Controlled Fusion, Volume* 1*: Plasma Physics*, 2nd edition. Springer, 2006.

[Christiansen 1993] J.P. Christiansen, P.M. Stubberfield, J.G. Cordey, C. Gormezano, C.W. Gowers, J. O'Rourke, D. Stork, A. Taroni and C.D. Challis. *The scaling of transport with normalized Larmor radius in JET.* Nuclear Fusion, vol. 33, no. 6, page 863, 1993.

[Chu 1993] Douglas C. Chu and George Em Karniadakis. *A direct numerical simulation of laminar and turbulent flow over riblet-mounted surfaces.* Journal of Fluid Mechanics, vol. 250, pages 1–42, 1993.

[Citrin 2017] J Citrin, H Arnichand, J Bernardo, C Bourdelle, X Garbet, F Jenko, S Hacquin, M J Pueschel and R Sabot. *Comparison between measured and predicted turbulence frequency spectra in ITG and TEM regimes.* Plasma Physics and Controlled Fusion, vol. 59, no. 6, page 064010, 2017.

[Clairet 2010] F. Clairet, S. Heuraux, C. Bottereau, D. Molina, L. Ducobu, F. Leroux and A. Barbuti. *Fast sweeping reflectometry upgrade on Tore Supra.* Review of Scientific Instruments, vol. 81, no. 10, page 10D903, 2010.

[Colas 2006] L. Colas, V. Basiuk, B. Beaumont, A. Bécoulet, G. Bosia, S. Brémond, M. Chantant, F. Clairet, A. Ekedahl, E. Faudot, A. Géraud, M. Goniche, S. Heuraux, G.T. Hoang, G. Lombard, L. Millon, R. Mitteau, P. Mollard, K. Vulliez and the Tore Supra team. *Key results of long pulse ICRH operation in Tore Supra.* Nuclear Fusion, vol. 46, no. 7, page S500, 2006.

[Colin 2001] Muriel Colin. *Modelisations d'un reflectometre mode X en vue de caracteriser les fluctuations de densite et de champ magnetique: applications aux signaux de Tore Supra.* PhD thesis, University of Nanvy I, 2001.

[Connor 1998] J W Connor. *Edge-localized modes - physics and theory.* Plasma Physics and Controlled Fusion, vol. 40, no. 5, page 531, 1998.

[Connor 2000] J W Connor and H R Wilson. *A review of theories of the L-H transition.* Plasma Physics and Controlled Fusion, vol. 42, no. 1, page R1, 2000.

[Conway 2005] G D Conway, B Scott, J Schirmer, M Reich, A Kendl and the ASDEX Upgrade Team. *Direct measurement of zonal flows and geodesic acoustic mode oscillations in ASDEX Upgrade using Doppler reflectometry.* Plasma Physics and Controlled Fusion, vol. 47, no. 8, page 1165, 2005.

[Conway 2006] G.D. Conway, C. Angioni, R. Dux, F. Ryter, A.G. Peeters, J. Schirmer, C. Troester, CFN Reflectometry Group and the ASDEX Upgrade team. *Observations on core turbulence transitions in ASDEX Upgrade using Doppler reflectometry.* Nuclear Fusion, vol. 46, page S799, 2006.

[Craxton 2015] R. S. Craxton, K. S. Anderson, T. R. Boehly, V. N. Goncharov, D. R. Harding, J. P. Knauer, R. L. McCrory, P. W. McKenty, D. D. Meyerhofer, J. F. Myatt, A. J. Schmitt, J. D. Sethian, R. W. Short, S. Skupsky, W. Theobald, W. L. Kruer, K. Tanaka, R. Betti, T. J. B. Collins, J. A. Delettrez, S. X. Hu, J. A. Marozas, A. V. Maximov, D. T. Michel, P. B. Radha, S. P. Regan, T. C. Sangster, W. Seka, A. A. Solodov, J. M. Soures, C. Stoeckl and J. D. Zuegel. *Direct-drive inertial confinement fusion: A review.* Physics of Plasmas, vol. 22, no. 11, page 110501, 2015.

[Creely 2017] A. J. Creely, N. T. Howard, P. Rodriguez-Fernandez, N. Cao, A. E. Hubbard, J. W. Hughes, J. E. Rice, A. E. White, J. Candy, G. M. Staebler, G. D. Conway, S. J. Freethy and C. Sung. *Validation of nonlinear gyrokinetic simulations of L- and I-mode plasmas on Alcator C-Mod.* Physics of Plasmas, vol. 24, no. 5, page 056104, 2017.

[Crocker 2018] N.A. Crocker, S. Kubota, W.A. Peebles, T.L. Rhodes, E.D. Fredrickson, E. Belova, A. Diallo, B.P. LeBlanc and S.A. Sabbagh. *Density perturbation mode structure of high frequency compressional and global Alfvén eigenmodes in the National Spherical Torus Experiment using a novel reflectometer analysis technique.* Nuclear Fusion, vol. 58, no. 1, page 016051, 2018.

[Diamond 2005] P H Diamond, S-I Itoh, K Itoh and T S Hahm. *Zonal flows in plasma–a review.* Plasma Physics and Controlled Fusion, vol. 47, 2005.

[Dittmar 2013] Michael Dittmar. *The end of cheap uranium.* Science of The Total Environment, vol. 461-462, pages 792 – 798, 2013.

[Donné 1997] A.J.H Donné, S.H Heijnen and C.A.J Hugenholtz. *Pulsed radar reflectometry and prospects for fluctuation measurements.* Fusion Engineering and Design, vol. 34-35, pages 73 – 80, 1997. Fusion Plasma Diagnostics.

[Ejiri 1997] A Ejiri, K Shinohara and K Kawahata. *An algorithm to remove fringe jumps and its application to microwave reflectometry.* Plasma Physics and Controlled Fusion, vol. 39, no. 12, page 1963, 1997.

[Erofeev 2017] I. Erofeev, E. Fable, C. Angioni, R.M. McDermott and The ASDEX Upgrade Team. *Theory-based modeling of LOC-SOC transitions in ASDEX Upgrade.* Nuclear Fusion, vol. 57, no. 12, page 126067, 2017.

[Fanack 1996] C Fanack, I Boucher, F Clairet, S Heuraux, G Leclert and X L Zou. *Ordinary-mode reflectometry: modification of the scattering and cut-off responses due to the shape of localized density fluctuations.* Plasma Physics and Controlled Fusion, vol. 38, no. 11, pages 1915–1930, nov 1996.

[Fernández-Marina 2014] F. Fernández-Marina, T. Estrada and E. Blanco. *Turbulence radial correlation length measurements using Doppler reflectometry in TJ-II.* Nuclear Fusion, vol. 54, no. 7, page 072001, apr 2014.

[Fredrickson 2018] E.D. Fredrickson, E.V. Belova, N.N. Gorelenkov, M. Podestà, R.E. Bell, N.A. Crocker, A. Diallo, B.P. LeBlanc and the NSTX-U team. *Global Alfvén eigenmode scaling and suppression: experiment and theory.* Nuclear Fusion, vol. 58, no. 8, page 082022, 2018.

[Freidberg 2007] Jeffrey Freidberg. *Plasma Physics and Fusion Energy.* Cambridge University Press, 2007.

[Fridleifsson 2001] Ingvar B Fridleifsson. *Geothermal energy for the benefit of the people.* Renewable and Sustainable Energy Reviews, vol. 5, no. 3, pages 299 – 312, 2001.

[Frish 1995] U. Frish. Turbulence: The legacy of a. n. kolmogorov. Cambridge University Press, 1995.

[Garbet 1992] X. Garbet, J. Payan, C. Laviron, P. Devynck, S.K. Saha, H. Capes, X.P. Chen, J.P. Coulon, C. Gil, G.R. Harris, T. Hutter, A.-L. Pecquet, A. Truc, P. Hennequin, F. Gervais and A. Quemeneur. *Turbulence and energy confinement in TORE SUPRA Ohmic discharges.* Nuclear Fusion, vol. 32, no. 12, page 2147, 1992.

[Garbet 2001] X Garbet. *Turbulence in fusion plasmas: key issues and impact on transport modelling.* Plasma Physics and Controlled Fusion, vol. 43, no. 01, page A251, 2001.

[Garbet 2004] X Garbet, P Mantica, C Angioni, E Asp, Y Baranov, C Bourdelle, R Budny, F Crisanti, G Cordey, L Garzotti, N Kirneva, D Hogeweij, T Hoang, F Imbeaux, E Joffrin, X Litaudon, A Manini, C McDonald, H Nordman, V Parail, A Peeters, F Ryter, C Sozzi, M Valovic, T Tala, A Thyagaraja, I Voitsekhovitch, J Weiland, H Weisen and A Zabolotsky. *Physics of transport in tokamaks.* Plasma Physics and Controlled Fusion, vol. 46, page B557, 2004.

[Garbet 2010] X. Garbet, Y. Idomura, L. Villard and T.H. Watanabe. *Gyrokinetic simulations of turbulent transport.* Nuclear Fusion, vol. 50, page 043002, 2010.

[Gil 2009] C. Gil, C. De Michelis, D. Elbeze, C. Fenzi, J. P. Gunn, F. Imbeaux, Ph. Lotte, D. Mazon, O. Meyer, M. Missirlian, Ph. Moreau, R. Reichle, R. Sabot, F. Saint-Laurent, J.-L. Segui, A. Simonin, J.-M. Travere, J.-C. Vallet and Tore Supra Team. *Diagnostic Systems on Tore Supra.* Fusion Science and Technology, vol. 56, no. 3, pages 1219–1252, 2009.

[Goldston 1995] R J Goldston and P H Rutherford. *Introduction to Plasma Physics.* Institute of Physics (IOP) Publishing Bristol and Philadelphia, 1995.

[Greenwald 1984] M. Greenwald, D. Gwinn, S. Milora, J. Parker, R. Parker, S. Wolfe, M. Besen, F. Camacho, S. Fairfax, C. Fiore*et al.* *Energy Confinement of High-Density Pellet-Fueled Plasmas in the Alcator-c Tokamaks.* Phys. Rev. Lett., vol. 53, pages 352–355, 1984.

[Grésillon 1992] D Grésillon, B Cabrit, J P Villain, C Hanuise, A Truc, C Laviron, P Hennequin, F Gervais, A Quemeneur, X Garbet, J Payan and P Devynck. *Collective scattering of electromagnetic waves and crossB plasma diffusion.* Plasma Physics and Controlled Fusion, vol. 34, no. 13, page 1985, 1992.

[Groebner 1990] R. J. Groebner, K. H. Burrell and R. P. Seraydarian. *Role of edge electric field and poloidal rotation in the L-H transition.* Phys. Rev. Lett., vol. 64, pages 3015–3018, 1990.

[Guirlet 2010] R. Guirlet*et al.* *Particle transport in low core turbulence Tore-Supra plasmas.* Nuclear Fusion, vol. 50, no. 9, page 095009, 2010.

[Gusakov 2002] E. Z. Gusakov and A. Yu. Popov. *Non-linear tgheory of fluctuation reflectometry.* Plasma Physics and Controlled Fusion, vol. 44, no. 02, page 2327, 2002.

[Heidbrink 2006] W.W. Heidbrink, E.D. Fredrickson, N.N. Gorelenkov, T.L. Rhodes and M.A. Van Zeeland. *Observation of compressional Alfvén eigenmodes (CAE) in a conventional tokamak.* Nuclear Fusion, vol. 46, no. 2, page 324, 2006.

[Hennequin 1999] P. Hennequin, C. Honoré, A. Quéméneur, A. Truc, F. Fervais, C. Fenzi and R. Sabot. *Analysis of density fluctuation frequency spectra in Tore Supra as a tool for studying plasma motion and transport properties.* In 26th EPS Conf. on Contr. Fusion and Plasma, volume 23J, pages 977 – 980. European Physical Society, Petit-Lancy, 1999.

[Hennequin 2006] P. Hennequin, C. Honoré, A. Truc, A. Quéméneur, C. Fenzi-Bonizec, C. Bourdelle, X. Garbet, G.T. Hoang and the Tore Supra team. *Fluctuation spectra and velocity profile from Doppler backscattering on Tore Supra.* Nuclear Fusion, vol. 46, no. 9, page S771, 2006.

[Hinton 1976] F. L. Hinton and R. D. Hazeltine. *Theory of plasma transport in toroidal confinement systems.* Reviews of Modern Physics, vol. 48, no. 0, pages 239–308, 1976.

[Hoang 2003] G. T. Hoang, C. Bourdelle, B. Pégourié, B. Schunke, J. F. Artaud, J. Bucalossi, F. Clairet, C. Fenzi-Bonizec, X. Garbet, C. Gil, R. Guirlet, F. Imbeaux, J. Lasalle, T. Loarer, C. Lowry, J. M. Travère and E. Tsitrone. *Particle Pinch with Fully Noninductive Lower Hybrid Current Drive in Tore Supra.* Phys. Rev. Lett., vol. 90, page 155002, Apr 2003.

[Holland 2016] C. Holland. *Validation metrics for turbulent plasma transport.* Physics of Plasmas, vol. 23, no. 6, page 060901, 2016.

[Hornung 2013a] G. Hornung. *Study of plasma turbulence by ultrafast sweeping reflectometry on the Tore Supra tokamak (Appendix C).* PhD thesis, Aix-Marseille University, 2013.

[Hornung 2013b] G Hornung, F Clairet, G L Falchetto, R Sabot, H Arnichand and L Vermare. *Turbulence correlation properties measured with ultrafast sweeping reflectometry on Tore Supra.* Plasma Physics and Controlled Fusion, vol. 55, no. 12, page 125013, 2013.

[Howard 2008] Wilson Howard. *Edge Localized Modes in Tokamaks.* Fusion Science and Technology, vol. 53, no. 2T, pages 161–169, 2008.

[Hutchinson 2002] I.H. Hutchinson. *Principles of Plasma Diagnostics*, 2nd edition. Cambridge University Press, 2002.

[Ida 2000] T. Ida, M. Ando and H. Toraya. *Extended pseudo-Voigt function for approximating the Voigt profile.* Journal of Applied Crystallography, vol. 33, no. 6, pages 1311–1316, 2000.

[Jackson 1991] G. L. Jackson, J. Winter, T. S. Taylor, K. H. Burrell, J. C. DeBoo, C. M. Greenfield, R. J. Groebner, T. Hodapp, K. Holtrop, E. A. Lazarus, L. L. Lao, S. I. Lippmann, T. H. Osborne, T. W. Petrie, J. Phillips, R. James, D. P. Schissel, E. J. Strait, A. D. Turnbull, W. P. West and DIII-D Team. *Regime of very high confinement in the boronized DIII-D tokamak.* Phys. Rev. Lett., vol. 67, pages 3098–3101, Nov 1991.

[Jacobson 2011] Mark Z. Jacobson and Mark A. Delucchi. *Providing all global energy with wind, water, and solar power, Part I: Technologies, energy resources, quantities and areas of infrastructure, and materials.* Energy Policy, vol. 39, no. 3, pages 1154 – 1169, 2011.

[Kaldellis 2007] J.K. Kaldellis and D. Zafirakis. *Optimum energy storage techniques for the improvement of renewable energy sources-based electricity generation economic efficiency.* Energy, vol. 32, no. 12, pages 2295 – 2305, 2007.

[Khvesyuk 2002] V I Khvesyuk and A Yu Chirkov. *Low-radioactivity D- 3 He fusion fuel cycles with 3 He production.* Plasma Physics and Controlled Fusion, vol. 44, no. 2, page 253, 2002.

[Kolmogorov 1941] A. N. Kolmogorov. *The local structure of turbulence in incompressible viscous fluid for very large Reynolds numbers.* Proceedings: Mathematical and Physical Sciences, vol. 434, no. 1890, pages 9–13, 1941.

[Kosolapova 2012] N V Kosolapova, E Z Gusakov and S Heuraux. *Numerical modeling of micro turbulence wave number spectra reconstruction using radial correlation reflectometry: I. O-mode reflectometry at the linear plasma density profile*. Plasma Physics and Controlled Fusion, vol. 54, no. 3, page 035008, 2012.

[Kraichnan 1971] Robert H. Kraichnan. *Inertial-range transfer in two- and three-dimensional turbulence*. Journal of Fluid Mechanics, vol. 47, no. 3, pages 525–535, 1971.

[Krämer-Flecken 2004] A. Krämer-Flecken, V. Dreval, S. Soldatov, A. Rogister, V. Vershkov and the TEXTOR-team. *Turbulence studies with means of reflectometry at TEXTOR*. Nuclear Fusion, vol. 44, no. 11, page 1143, 2004.

[Krämer-Flecken 2010] A. Krämer-Flecken, S. Soldatov, B. Vowinkel and P. Mueller. *Correlation reflectometry at TEXTOR*. Review of Scientific Instruments, vol. 81, page 113502, 2010.

[Krämer-Flecken 2015] A Krämer-Flecken, S Soldatov, Y Xu, H Arnichand, S Hacquin, R Sabot and the TEXTOR team. *Long-range correlation properties of quasi-coherent modes at TEXTOR*. New Journal of Physics, vol. 17, no. 7, page 073007, 2015.

[Laviron 1996] C Laviron, A J H Donné, M E Manso and J Sanchez. *Reflectometry techniques for density profile measurements on fusion plasmas*. Plasma Physics and Controlled Fusion, vol. 38, no. 7, page 905, 1996.

[Le Pape 2018] S. Le Pape, L. F. Berzak Hopkins, L. Divol, A. Pak, E. L. Dewald, S. Bhandarkar, L. R. Bennedetti, T. Bunn, J. Biener, J. Crippen, D. Casey, D. Edgell, D. N. Fittinghoff, M. Gatu-Johnson, C. Goyon, S. Haan, R. Hatarik, M. Havre, D. D-M. Ho, N. Izumi, J. Jaquez, S. F. Khan, G. A. Kyrala, T. Ma, A. J. Mackinnon, A. G. MacPhee, B. J. MacGowan, N. B. Meezan, J. Milovich, M. Millot, P. Michel, S. R. Nagel, A. Nikroo, P. Patel, J. Ralph, J. S. Ross, N. G. Rice, D. Strozzi, M. Stadermann, P. Volegov, C. Yeamans, C. Weber, C. Wild, D. Callahan and O. A. Hurricane. *Fusion Energy Output Greater than the Kinetic Energy of an Imploding Shell at the National Ignition Facility*. Phys. Rev. Lett., vol. 120, page 245003, Jun 2018.

[Lebschy 2018] A. Lebschy, R.M. McDermott, C. Angioni, B. Geiger, D. Prisiazhniuk, M. Cavedon, G.D. Conway, R. Dux, M.G. Dunne, A. Kappatou, T. Pütterich, U. Stroth, E. Viezzer and the ASDEX Upgrade Team. *Measurement of the complete core plasma flow across the LOC-SOC transition at ASDEX Upgrade*. Nuclear Fusion, vol. 58, no. 2, page 026013, 2018.

[Lee 2018] J. A. Lee, W. Lee, J. M. Kwon, S. H. Ko, J. Leem, G. S. Yun, H. K. Park, Y. S. Park, K. W. Kim and N. C. Luhmann. *Observation of electron driven quasi-coherent modes and their connection with core intrinsic rotation in KSTAR ECH and ohmic L-mode plasmas*. Physics of Plasmas, vol. 25, no. 2, page 022513, 2018.

[Lennholm 2003] M. Lennholm, G. Agarici, G. Berger-By, P. Bosia, F. Bouquey, E. Cellier, J. Clary, M. Clapit, C. Darbos, G. Giruzzi, M. Jung, R. Magne, D. Roux, J.L. Segui, E. Traisnel and X. Zou. *The ECRH/ECCD system on Tore Supra, a major step towards continuous operation.* Nuclear Fusion, vol. 43, no. 11, page 1458, 2003.

[Leonard 2014] A. W. Leonard. *Edge-localized-modes in tokamaks.* Physics of Plasmas, vol. 21, no. 9, page 090501, 2014.

[Levinton 1995] F. M. Levinton, M. C. Zarnstorff, S. H. Batha, M. Bell, R. E. Bell, R. V. Budny, C. Bush, Z. Chang, E. Fredrickson, A. Janos, J. Manickam, A. Ramsey, S. A. Sabbagh, G. L. Schmidt, E. J. Synakowski and G. Taylor. *Improved Confinement with Reversed Magnetic Shear in TFTR.* Phys. Rev. Lett., vol. 75, pages 4417–4420, Dec 1995.

[Lieber 2003] Chad A. Lieber and Anita Mahadevan-Jansen. *Automated Method for Subtraction of Fluorescence from Biological Raman Spectra.* Appl. Spectrosc., vol. 57, no. 11, pages 1363–1367, Nov 2003.

[Ma 2016] T. Ma, S. MacLaren, J. Salmonson, S. Khan, J. Pino, J. Ralph, R. Rygg, J. Field, R. Tommasini, D. Turnbull, A. Mackinnon, K. Baker, L. R. Benedetti, P. Celliers, E. Dewald, T. Dittrich, L. Berzak Hopkins, N. Izumi, P. Kervin, S. Nagel, A. Pak, R. Tipton, G. Kyrala and J. Kline. *Temporal evolution of the two-shock implosion on the National Ignition Facility.* In 2016 IEEE International Conference on Plasma Science (ICOPS), pages 1–1, 2016.

[Manz 2012] P. Manz, G. S. Xu, B. N. Wan, H. Q. Wang, H. Y. Guo, I. Cziegler, N. Fedorczak, C. Holland, S. H. Müller, S. C. Thakur, M. Xu, K. Miki, P. H. Diamond and G. R. Tynan. *Zonal flow triggers the L-H transition in the Experimental Advanced Superconducting Tokamak.* Physics of Plasmas, vol. 19, no. 7, page 072311, 2012.

[Martin 2008] Y R Martin, T Takizuka and the ITPA CDBM H-mode Threshold Database Working Group. *Power requirement for accessing the H-mode in ITER.* Journal of Physics: Conference Series, vol. 123, no. 1, page 012033, 2008.

[Matthews 1997] G.F. Matthews, S. Allen, N. Asakura, J. Goetz, H. Guo, A. Kallenbach, B. Lipschultz, K. McCormick, M. Stamp, U. Samm, P.C. Stangeby, K.-H. Steuer, A. Taroni, B. Unterberg and P. West. *Scaling radiative plasmas to ITER.* Journal of Nuclear Materials, vol. 241-243, pages 450 – 455, 1997.

[Mattor 1992] N. Mattor and P. W. Terry. *Frequency spectrum in drift wave turbulence.* Physics of Fluids B: Plasma Physics, vol. 4, no. 5, pages 1126–1138, 1992.

[Mazzucato 1991] E Mazzucato and R Nazikian. *Microwave reflectometry for the study of density fluctuations in tokamak plasmas.* Plasma Physics and Controlled Fusion, vol. 33, no. 3, page 261, 1991.

[Mazzucato 1998] E. Mazzucato. *Microwave reflectometry for magnetically confined plasmas.* Review of Scientific Instruments, vol. 69, no. 6, page 2201, 1998.

[Michel 2009] P. Michel, L. Divol, E. A. Williams, S. Weber, C. A. Thomas, D. A. Callahan, S. W. Haan, J. D. Salmonson, S. Dixit, D. E. Hinkel, M. J. Edwards, B. J. MacGowan, J. D. Lindl, S. H. Glenzer and L. J. Suter. *Tuning the Implosion Symmetry of ICF Targets via Controlled Crossed-Beam Energy Transfer.* Phys. Rev. Lett., vol. 102, page 025004, Jan 2009.

[Miller 2004] George H. Miller, Edward I. Moses and Craig R. Wuest. *The National Ignition Facility: enabling fusion ignition for the 21st century.* Nuclear Fusion, vol. 44, no. 12, page S228, 2004.

[Momirlan 2005] Magdalena Momirlan and T.N. Veziroglu. *The properties of hydrogen as fuel tomorrow in sustainable energy system for a cleaner planet.* International Journal of Hydrogen Energy, vol. 30, no. 7, pages 795 – 802, 2005.

[Morales 2018] Rennan Bianchetti Morales. *Density profile reconstruction methods for extraordinary mode reflectometry.* Ph.D. dissertation, University of Lorraine, 2018.

[Moses 2016] E. I. Moses, J. D. Lindl, M. L. Spaeth, R. W. Patterson, R. H. Sawicki, L. J. Atherton, P. A. Baisden, L. J. Lagin, D. W. Larson, B. J. MacGowan, G. H. Miller, D. C. Rardin, V. S. Roberts, B. M. Van Wonterghem and P. J. Wegner. *Overview: Development of the National Ignition Facility and the Transition to a User Facility for the Ignition Campaign and High Energy Density Scientific Research.* Fusion Science and Technology, vol. 69, no. 1, pages 1–24, 2016.

[Motojima 2000] O. Motojima, K. Akaishi, H. Chikaraishi, H. Funaba, S. Hamaguchi, S. Imagawa, S. Inagaki, N. Inoue, A. Iwamoto, S. Kitagawa, A. Komori, Y. Kubota, R. Maekawa, S. Masuzaki, T. Mito, J. Miyazawa, T. Morisaki, K. Murai, T. Muroga, T. Nagasaka, Y. Nakamura, A. Nishimura, K. Nishimura, N. Noda, N. Ohyabu, A. Sagara, S. Sakakibara, R. Sakamoto, S. Satoh, T. Satow, M. Shoji, H. Suzuki, K. Takahata, H. Tamura, K.Y. Watanabe, H. Yamada, S. Yamada, S. Yamaguchi, K. Yamazaki, N. Yanagi, T. Baba, H. Hayashi, M. Iima, T. Inoue, S. Kato, T. Kato, T. Kondo, S. Moriuchi, H. Ogawa, I. Ohtake, K. Ooba, H. Sekiguchi, N. Suzuki, S. Takami, Y. Taniguchi, T. Tsuzuki, N. Yamamoto, K. Yasui, H. Yonezu, M. Fujiwara and A. Iiyoshi. *Progress summary of LHD engineering design and construction.* Nuclear Fusion, vol. 40, no. 3Y, page 599, 2000.

[Muscatello 2014] C. M. Muscatello, C. W. Domier, X. Hu, G. J. Kramer, N. C. Luhmann, X. Ren, P. Riemenschneider, A. Spear, B. J. Tobias, E. Valeo and L. Yu. *Technical overview of the millimeter-wave imaging reflectometer on the DIII-D tokamak (invited).* Review of Scientific Instruments, vol. 85, no. 11, page 11D702, 2014.

[Nagel 2017] S. R. Nagel, K. S. Raman, C. M. Huntington, S. A. MacLaren, P. Wang, M. A. Barrios, T. Baumann, J. D. Bender, L. R. Benedetti, D. M. Doane, S. Felker, P. Fitzsimmons, K. A. Flippo, J. P. Holder, D. N. Kaczala, T. S. Perry, R. M. Seugling, L. Savage and Y. Zhou. *A platform for studying the Rayleigh-Taylor and Richtmyer-Meshkov instabilities in a planar geometry at high energy density at the National Ignition Facility.* Physics of Plasmas, vol. 24, no. 7, page 072704, 2017.

[Nocente 2013] M. Nocente, M. Tardocchi, A. Olariu, S. Olariu, R. C. Pereira, I. N. Chugunov, A. Fernandes, D. B. Gin, G. Grosso, V. G. Kiptily, A. Neto, A. E. Shevelev, M. Silva, J. Sousa and G. Gorini. *High Resolution Gamma Ray Spectroscopy at MHz Counting Rates With $LaBr_3$Scintillators for Fusion Plasma Applications.* IEEE Transactions on Nuclear Science, vol. 60, no. 2, pages 1408–1415, 2013.

[Ongena 2012] J. Ongena and G. Van Oost. *Energy for Future Centuries: Prospects for Fusion Power as a Future Energy Source.* Fusion Science and Technology, vol. 61, no. 2T, pages 3–16, 2012.

[Panwar 2011] N.L. Panwar, S.C. Kaushik and Surendra Kothari. *Role of renewable energy sources in environmental protection: A review.* Renewable and Sustainable Energy Reviews, vol. 15, no. 3, pages 1513 – 1524, 2011.

[Paul 1992] S. F. Paul, N. Bretz, R. D. Durst, R. J. Fonck, Y. J. Kim, E. Mazzucato and R. Nazikian. *Measurements of long-wavelength density fluctuations in TFTR.* Physics of Fluids B: Plasma Physics, vol. 4, no. 9, pages 2922–2928, 1992.

[Petty 1995] C. C. Petty, T. C. Luce, K. H. Burrell, S. C. Chiu, J. S. deGrassie, C. B. Forest, P. Gohil, C. M. Greenfield, R. J. Groebner, R. W. Harvey, R. I. Pinsker, R. Prater, R. E. Waltz, R. A. James and D. Wròblewski. *Nondimensional transport scaling in DIII-D: Bohm versus gyro-Bohm resolved.* Physics of Plasmas, vol. 2, no. 6, pages 2342–2348, 1995.

[Pope 2000] Stephen B. Pope. *Turbulence Flows.* Cambridge University Press, 2000.

[Rentizelas 2009] Athanasios A. Rentizelas, Athanasios J. Tolis and Ilias P. Tatsiopoulos. *Logistics issues of biomass: The storage problem and the multi-biomass supply chain.* Renewable and Sustainable Energy Reviews, vol. 13, no. 4, pages 887 – 894, 2009.

[Rice 2012] J. E. Rice, M. J. Greenwald, Y. A. Podpaly, M. L. Reinke, P. H. Diamond, J. W. Hughes, N. T. Howard, Y. Ma, I. Cziegler, B. P. Duval, P. C. Ennever, D. Ernst, C. L. Fiore, C. Gao, J. H. Irby, E. S. Marmar, M. Porkolab, N. Tsujii and S. M. Wolfe. *Ohmic energy confinement saturation and core toroidal rotation reversal in Alcator C-Mod plasmas.* Physics of Plasmas, vol. 19, no. 5, page 056106, 2012.

[Richardson 1922] Lewis F Richardson. *Weather Prediction by Numerical Process*. Cambridge University Press, 1922.

[Romanelli 1989] F. Romanelli. *Ion temperature-gradient-driven modes and anomalous ion transport in tokamaks*. Physics of Fluids B: Plasma Physics, vol. 1, no. 5, pages 1018–1025, 1989.

[Romanelli 2015] F. Romanelli and on behalf of JET Contributors. *Overview of the JET results*. Nuclear Fusion, vol. 55, no. 10, page 104001, 2015.

[Ross 2015] J. S. Ross, D. Ho, J. Milovich, T. Döppner, J. McNaney, A. G. MacPhee, A. Hamza, J. Biener, H. F. Robey, E. L. Dewald, R. Tommasini, L. Divol, S. Le Pape, L. Berzak Hopkins, P. M. Celliers, O. Landen, N. B. Meezan and A. J. Mackinnon. *High-density carbon capsule experiments on the national ignition facility*. Phys. Rev. E, vol. 91, page 021101, Feb 2015.

[Ryter 1998] F Ryter, W Suttrop, B Brüsehaber, M Kaufmann, V Mertens, H Murmann, A G Peeters, J Stober, J Schweinzer, H Zohm and ASDEX Upgrade Team. *H-mode power threshold and transition in ASDEX Upgrade*. Plasma Physics and Controlled Fusion, vol. 40, no. 5, page 725, 1998.

[Sabot 2004] R. Sabot, C. Bottereau, J.-M. Chareau, F. Clairet and M. Paume. *Single sideband modulator, a key component of Tore-Supra heterodyne reflectometers*. Review of Scientific Instruments, vol. 75, no. 8, page 2656, 2004.

[Sabot 2006a] R Sabot, F Clairet, G D Conway, L Cupido, X Garbet, G Falchetto, T Gerbaud, S Hacquin, P Hennequin, S Heuraux, C Honoré, G Leclert, L Meneses, A Sirinelli, L Vermare and A Truc. *Recent results on turbulence and MHD activity achieved by reflectometry*. Plasma Physics and Controlled Fusion, vol. 48, no. 12B, page B421, 2006.

[Sabot 2006b] R. Sabot, A. Sirinelli, J.-M. Chareau and J.-C. Giaccalone. *A dual source D-band reflectometer for density profile and fluctuations measurements in Tore-Supra*. Nuclear Fusion, vol. 46, no. 9, page S685, 2006.

[Sabot 2016] Roland Sabot, Didier Elbèze, Woochang Lee, Yoonbum Nam, Hyeon Park, Junsong Shen, Gunsu Yun, Minjun Choi, Jean-Claude Giacalone, Timothée Nicolas, Christine Bottereau, Frédéric Clairet, Philippe Lotte and Diego Molina. *Microwave imaging of magnetohydrodynamic instabilities in fusion plasma*. Comptes Rendus Physique, vol. 17, no. 9, page 1018, 2016.

[Sarazin 2012] Y. Sarazin. Turbulence and transport. Lecture given in the french master in fusion sciences, 2012.

[Schmitz 2012] L. Schmitz, L. Zeng, T. L. Rhodes, J. C. Hillesheim, E. J. Doyle, R. J. Groebner, W. A. Peebles, K. H. Burrell and G. Wang. *Role of Zonal Flow Predator-Prey Oscillations in Triggering the Transition to H-Mode Confinement*. Phys. Rev. Lett., vol. 108, page 155002, 2012.

[Schunke 2005] B. Schunke, G. T. A. Huysmans and P. R. Thomas. *Evidence of the influence of reflections on the Zeff profile measurements in the Tore Supra tokamak and their mitigation.* Review of Scientific Instruments, vol. 76, no. 8, page 083501, 2005.

[Ségui 2005] J. L. Ségui, D. Molina, G. Giruzzi, M. Goniche, G. Huysmans, P. Maget and M. Ottaviani. *An upgraded 32-channel heterodyne electron cyclotron emission radiometer on Tore Supra.* Review of Scientific Instruments, vol. 76, no. 12, page 123501, 2005.

[Shabbir 2016] A. Shabbir, G. Hornung, G. Verdoolaege and JET Contributors. *A classification scheme for edge-localized modes based on their probability distributions.* Review of Scientific Instruments, vol. 87, no. 11, page 11D404, 2016.

[Shafiee 2009] Shahriar Shafiee and Erkan Topal. *When will fossil fuel reserves be diminished?* Energy Policy, vol. 37, no. 1, pages 181 – 189, 2009.

[Shaing 1990] K. C. Shaing, E. C. Crume and W. A. Houlberg. *Bifurcation of poloidal rotation and suppression of turbulent fluctuations: A model for the L-H transition in tokamaks.* Physics of Fluids B: Plasma Physics, vol. 2, no. 6, pages 1492–1498, 1990.

[Shelukhin 2006] D. A. Shelukhin, S. V. Soldatov, V. A. Vershkov and A. O. Urazbaev. *Estimates of the local parameters of plasma density fluctuations by reflectometry measurements.* Plasma Physics Reports, vol. 32, no. 9, pages 707–717, 2006.

[Shimomura 1985] Y. Shimomura. *Empirical scaling of energy confinement time in L-mode plasma and optimised mode and some consideration of reactor core plasma in tokamak, Japanese Atomic Energy Research Institute (1985).* Report JAERI-M-85-080, 1985.

[Sirinelli 2006] Antoine Sirinelli. *Étude du Transport et de la Turbulence par Réflectométrie dans un Plasma de Fusion.* Ph.D. dissertation, École Polytechnique, 2006.

[Smeulders 1995] P. Smeulders, L.C. Appel, B. Balet, T.C. Hender, L. Lauro-Taroni, D. Stork, B. Wolle, S. Ali-Arshad, B. Alper, H.J. De Blank, M. Bures, B. De Esch, R. Giannella, R. Konig, P. Kupschus, K. Lawson, F.B. Marcus, M. Mattioli, H.W. Morsi, D.P. O'Brien, J. O'Rourke, G.J. Sadler, G.L. Schmidt, P.M. Stubberfield and W. Zwingmann. *Survey of pellet enhanced performance in JET discharges.* Nuclear Fusion, vol. 35, no. 2, page 225, 1995.

[Stix 1992] Thomas Howard Stix. *Waves in Plasmas.* American Institute of Physics, 1992.

[Sun 2017] Y. Sun, R. Sabot, G. Hornung, S. Heuraux, S. Hacquin, and G. Verdoolaege. *Systematic Study of Core Turbulence by Reflectometry Fluctuation Frequency Spectra.* In Proc. 13th Int. Reflectometry Worshop, Daejeon, Korea, May 2017.

[Sun 2018] Y. Sun, R. Sabot, G. Hornung, S. Heuraux, S. Hacquin and G. Verdoolaege. *Parametrization of reflectometry fluctuation frequency spectra for systematic study of fusion plasma turbulence.* Review of Scientific Instruments, vol. 89, no. 7, page 073504, 2018.

[Sun 2019] Y. Sun, R. Sabot, S. Heuraux, X. Garbet, S. Hacquin, G. Hornung and G. Verdoolaege. *Experimental trends of reflectometry frequency spectra emerging from a systematic analysis of the Tore Supra database.* Physics of Plasmas, vol. 26, no. 3, page 032307, 2019.

[Sung 2016] C. Sung, A. E. White, D. R. Mikkelsen, M. Greenwald, C. Holland, N. T. Howard, R. Churchill and C. Theiler. *Quantitative comparison of electron temperature fluctuations to nonlinear gyrokinetic simulations in C-Mod Ohmic L-mode discharges.* Physics of Plasmas, vol. 23, no. 4, page 042303, 2016.

[Thompson 1987] P. Thompson, D. E. Cox and J. B. Hastings. *Rietveld refinement of Debye–Scherrer synchrotron X-ray data from Al_2O_3.* Journal of Applied Crystallography, vol. 20, no. 2, pages 79–83, 1987.

[Ting 1991] L. Ting. *Viscous Vortical Flows.* Springer-Verlag, 1991.

[Truc 1986] A. Truc and TFR Group. *Correlation between low frequency turbulence and energy confinement in TFR.* Nuclear Fusion, vol. 26, no. 10, page 1303, 1986.

[Verdoolaege 2015] G. Verdoolaege and J-M. Noterdaeme. *Robust scaling in fusion science: case study for the L-H power threshold.* Nuclear Fusion, vol. 55, no. 11, page 113019, 2015.

[Vermare 2011] L. Vermare, P. Hennequin, Ö. D. Gürcan, C. Bourdelle, F. Clairet, X. Garbet, R. Sabot and the Tore Supra Team. *Impact of collisionality on fluctuation characteristics of micro-turbulence.* Physics of Plasmas, vol. 18, no. 1, 2011.

[Vershkov 2005] V.A. Vershkov, D.A. Shelukhin, S.V. Soldatov, A.O. Urazbaev, S.A. Grashin, L.G. Eliseev, A.V. Melnikov and the T-10 team. *Summary of experimental core turbulence characteristics in ohmic and electron cyclotron resonance heated discharges in T-10 tokamak plasmas.* Nuclear Fusion, vol. 45, no. 00, page S203, 2005.

[Vershkov 2011] V. A. Vershkov, A.A. Borschegovskiy, V.V. Chistyakov, M.M. Dremin, L.G. Eliseev, E.P. Gorbunov, S.A. Grashin, A.V. Khmara, A.Ya. Kislov, D.A. Kislov, A.D. Komarov, A.S. Kozachek, V.A. Krupin, L.I. Krupnik, S.V. Krylov, S.E. Lysenko, S.G. Maltsev, V.A. Mavrin, A.V. Melnikov, G.E. Notkin, A.Yu. Novikov, Yu.D. Pavlov, S.V. Perfilov, V.V. Piterskij, G.N. Ploskirev, V.I. Poznyak, K.A. Razumova, I.N. Roy, D.V. Ryzhakov, P.V. Savrukhin, E.A. Shestakov, D.A. Shelukhin, Yu.A. Skosyrev, R.V. Shurygin, G.N. Tilinin, E.V.

Trukhina1 and V.M. Trukhin. *Recent results of the T-10 tokamak.* Nuclear Fusion, vol. 51, no. 9, page 094019, 2011.

[Vlad 2005] M Vlad and F Spineanu. *Larmor radius effects on impurity transport in turbulent plasmas.* Plasma Physics and Controlled Fusion, vol. 47, no. 2, page 281, 2005.

[von der Linden 2014] W. von der Linden, V. Dose and U. von Toussaint. Bayesian probability theory, application in the physical sciences. Cambridge University Press, 2014.

[Wang 2017] Y. Wang, B. Tobias, Y.-T. Chang, J.-H. Yu, M. Li, F. Hu, M. Chen, M. Mamidanna, T. Phan, A.-V. Pham, J. Gu, X. Liu, Y. Zhu, C.W. Domier, L. Shi, E. Valeo, G.J. Kramer, D. Kuwahara, Y. Nagayama, A. Mase and N.C. Luhmann Jr. *Millimeter-wave imaging of magnetic fusion plasmas: technology innovations advancing physics understanding.* Nuclear Fusion, vol. 57, no. 7, page 072007, 2017.

[Ware 1970] A. A. Ware. *Pinch Effect for Trapped Particles in a Tokamak.* Phys. Rev. Lett., vol. 25, pages 15–17, Jul 1970.

[Watts 1996] C. Watts, R. F. Gandy, G. Cima, R. V. Bravenec, D. W. Ross, A. J. Wootton, A. Ouroua, J. W. Heard, T. P. Crowley, P. M. Schoch, D. L. Brower, Y. Jiang, B. Deng, C. W. Domier and N. C. Luhmann. *Poloidal asymmetry and gradient drive in core electron density and temperature fuctuations on the texas experimental tokamak-upgrade.* Physics of Plasmas, vol. 3, no. 5, pages 2013–2021, 1996.

[Welch 1967] P. Welch. *The use of Fast Fourier Transform for the estimation of power spectra: A method based on time averaging over short, modified periodograms.* IEEE Transactions on Audio and Electroacoustics, vol. 15, no. 2, pages 70–73, 1967.

[Wesson 1997] John Wesson. *Tokamaks*, 2nd edition. Oxford University Press, 1997.

[White 2008] A. E. White, L. Schmitz, G. R. McKee, C. Holland, W. A. Peebles, T. A. Carter, M. W. Shafer, M. E. Austin, K. H. Burrell, J. Candy, J. C. DeBoo, E. J. Doyle, M. A. Makowski, R. Prater, T. L. Rhodes, G. M. Staebler, G. R. Tynan, R. E. Waltz and G. Wang. *Measurements of core electron temperature and density fluctuations in DIII-D and comparison to nonlinear gyrokinetic simulations.* Physics of Plasmas, vol. 15, no. 5, page 056116, 2008.

[Wootton 1990] A. J. Wootton, B. A. Carreras, H. Matsumoto, K. McGuire, W. A. Peebles, Ch. P. Ritz, P. W. Terry and S. J. Zweben. *Fluctuations and anomalous transport in tokamaks.* Physics of Fluids B: Plasma Physics, vol. 2, no. 12, pages 2879–2903, 1990.

[Yamashita 2008] Toru Yamashita and Peter Hayes. *Analysis of XPS spectra of Fe2+ and Fe3+ ions in oxide materials.* Applied Surface Science, vol. 254, no. 8, pages 2441 – 2449, 2008.

[Yushmanov 1990a] P.N. Yushmanov, T. Takizuka, K.S. Riedel, O.J.W.F. Kardaun, J.G. Cordey, S.M. Kaye and D.E. Post. *Scalings for tokamak energy confinement.* Nuclear Fusion, vol. 30, no. 10, page 1999, 1990.

[Yushmanov 1990b] P.N. Yushmanov, T. Takizuka, K.S. Riedel, O.J.W.F. Kardaun, J.G. Cordey, S.M. Kaye and D.E. Post. *Scalings for tokamak energy confinement.* Nuclear Fusion, vol. 30, no. 10, page 1999, 1990.

[Zarzoso 2018] D. Zarzoso, D. del Castillo-Negrete, D.F. Escande, Y. Sarazin, X. Garbet, V. Grandgirard, C. Passeron, G. Latu and S. Benkadda. *Particle transport due to energetic-particle-driven geodesic acoustic modes.* Nuclear Fusion, vol. 58, no. 10, page 106030, 2018.

[Zhong 2016] W. L. Zhong, Z. B. Shi, Z. J. Yang, G. L. Xiao, Z. C. Yang, B. Y. Zhang, P. W. Shi, H. R. Du, X. M. Pan, R. B. Zhou, L. H. Wan, X. L. Zou, M. Xu, X. R. Duan, Yong Liu and G. Zhuang. *Experimental observation of turbulence transition and a critical gradient threshold for trapped electron mode in tokamak plasmas.* Physics of Plasmas, vol. 23, no. 6, page 060702, 2016.

[Zohm 1996] H Zohm. *Edge localized modes (ELMs).* Plasma Physics and Controlled Fusion, vol. 38, no. 2, page 105, 1996.

[Zonca 2007] F. Zonca, P. Buratti, A. Cardinali, L. Chen, J.-Q. Dong, Y.-X. Long, A.V. Milovanov, F. Romanelli, P. Smeulders, L. Wang, Z.-T. Wang, C. Castaldo, R. Cesario, E. Giovannozzi, M. Marinucci and V. Pericoli Ridolfini. *Electron fishbones: theory and experimental evidence.* Nuclear Fusion, vol. 47, no. 11, page 1588, 2007.

[Zou 1991] X L Zou, L Laurent and J M Rax. *Scattering of an electromagnetic wave in a plasma close to a cut-off layer. Application to fluctuation measurements.* Plasma Physics and Controlled Fusion, vol. 33, no. 8, page 903, 1991.

Appendix A

Analysis techniques for turbulence signals and spectra

Many data analysis methods have been developed to extract useful information from turbulence signals. Here, some basic linear analysis tools are presented that are used in this work.

A.1 Fourier analysis

Fourier and correlation analysis are the basic techniques in the study of fusion plasma turbulence. By calculating the power spectrum or coherence spectrum, information about the turbulent fluctuations can be extracted. The parametrization method developed in chapter 4 is based on the power spectrum. The coherence spectrum may be used in a similar way in future work. The main Fourier analysis techniques used in this study are briefly described in the following.

The physical quantities to be measured are real and continuous signals in time, while the signals acquired by the reflectometer constitute a discrete series of real or complex values of finite length $(t_1, t_2, \ldots, t_n)$. The Nyquist theorem determines the minimum sampling frequency required to accurately resolve the frequencies present in the turbulent fluctuations. Assuming that the highest desired frequency is F, the minimum sampling frequency is $2F$.

The Fourier transform is the most widely used technique to transform a time series to the frequency domain. The discrete-time Fourier transform (DFT) has been developed to process discrete time series. The DFT decomposes a finite-length discrete signal x_j $(j = 0, \ldots, n-1)$ into a set of n harmonic (complex exponential) components, hence measuring its frequency content. The resulting Fourier coefficients X_k are given by

$$X_k = \sum_{j=1}^{n-1} x_j e^{-2\pi i \frac{(j)(k)}{n}}, k = 0, \ldots, n-1. \tag{A.1}$$

The corresponding frequencies are

$$f_k = k/(n\Delta t), \tag{A.2}$$

where Δt is the sampling period. Then, from the Nyquist theorem we know that the Nyquist frequency is $f_s/2 = 1/2\Delta t$.

X_k is usually a complex value and its amplitude $|X_k|$ is referred as the *spectrum* of the signal at each frequency f_k. The DFT can be calculated conveniently using the fast

Fourier transform (FFT) algorithm. One important factor in calculating the DFT is the choice of the window function, which affects the weights of different frequencies. Some typical window functions include rectangle, triangle, Gaussian, sine/cosine, hann and hamming window, etc.

Furthermore, the discrete time series can be split into small time windows and the DFT can be calculated within each window. Two important applications are:

- **Averaging spectral estimation**: By averaging the spectra obtained from each window one can reduce the noise in the spectrum.

- **Spectrogram**: Since each time-window corresponds to a time index, the time evolution of the spectrum, called the spectrogram, is obtained by selecting consecutive (or overlapping) windows.

In fact, the two approaches are usually combined to obtain spectra with high signal-to-noise ratio at a specific time, or a spectrogram with high frequency and time resolution.

The power spectral density (PSD) of a time series describes the power distribution of the different frequency components in the signal. The PSD is commonly called *power spectrum* and it is defined as:

$$P_{xx}(f_n) = \frac{1}{n^2}\left[|X_n|^2 + |X_{n-n}|^2\right]. \tag{A.3}$$

The most widely used PSD algorithms include periodogram, Bartlett's method and Welch's method.

When dealing with two or more discrete-time signals, statistical correlation analysis plays an important role as well, although we do not apply it in this thesis.

A.2 Statistical analysis of spectra

After normalization of the power spectral density (PSD) $P(f)$ of a signal to 1,

$$\int_{f_{min}}^{f_{max}} P(f)\,\mathrm{d}f, \tag{A.4}$$

the properties of the PDF can be used to study the spectral properties. This is the approach used in the present work. The most widely used properties are the first four moments of the PDF: mean, variance, skewness and kurtosis.

In a discrete series $x_1, x_2, \ldots, x_n$ of any scalar quantity, the sample mean $\overline{x}$ is the averaged value of all n samples:

$$\overline{x} = \frac{1}{n}\sum_n x_i. \tag{A.5}$$

The cumulative distribution function (CDF) gives the probability that x assumes a value smaller or equal than a, $F_x(a) = P[x \leq a]$. The *median* of the series is defined as a

number m, satisfying:

$$P(X \leq m) \geq \frac{1}{2} \text{ and } P(X \geq m) \geq \frac{1}{2}. \tag{A.6}$$

When the probability density function of the series is approximately symmetric, e.g. a Gaussian distribution, the mean and median are almost equal and can both be used as a measure of central tendency. On the other hand, if the distribution is skewed, the median may better reflect the central tendency, as the mean is strongly influenced by the asymmetry of the tails of the distribution, e.g. in the case of outliers.

When using the mean value, the sample standard deviation s of the series,

$$s = \sqrt{\frac{1}{n}\sum_{n}(x_i - \overline{x})^2}, \tag{A.7}$$

is a measure of the spread of the samples around the mean, often used as an error bar. When the median is preferred as a measure of central tendency, it may also be preferable to use the mean absolute deviation around the median:

$$d = \frac{\sum_n |x_i - \text{median}(x)|}{n}. \tag{A.8}$$

The *skewness* or third standardized moment of a distribution is a measure of the asymmetry of the PDF around the mean. The sample skewness is often calculated as

$$\gamma_1 = \frac{\frac{1}{n}\sum_{i=1}^{n}(x_i - \bar{x})^3}{s^3}. \tag{A.9}$$

The *kurtosis*, or fourth standardized moment, is a measure of the peakedness of a distribution, and the heaviness of its tails, often using the Gaussian distribution as a reference. In that case, one speaks of the *excess kurtosis*, and the sample excess kurtosis can be calculated as

$$\gamma_2 = \frac{\frac{1}{n}\sum_{i=1}^{n}(x_i - \bar{x})^4}{s^4} - 3. \tag{A.10}$$

It becomes zero for a Gaussian distribution.

A.3 Fitting functions used in this work

In the parametrization method developed in chapter 4, one fundamental problem is to choose the function to fit each component of the frequency spectra. It should be characterized by only a few parameters, and it should be continuous and have infinite support. In order to represent the most basic features of a spectrum, at least three parameters are required: amplitude, central position and shape. In this study it is assumed that the spectra are symmetric with respect to the central position. Usually, multiple components have to be used to characterize a single spectrum, and the full spectrum is then modeled as the mixture distribution consisting of the components. In this work, the total mixture

distribution is normalized to 1, whereas the individual components are unnormalized, their amplitude adapted to the component which they are meant to fit. In the following, we introduce a number of fitting functions used to model spectrum components in this work. The functions are inspired by PDFs, but they are unnormalized and contain an amplitude parameter.

Gaussian function

The Gaussian (normal) distribution is the most commonly applied continuous probability distribution, and its PDF has been used extensively for spectrum fitting. The expression of the Gaussian function used in this work is:

$$f(x) = A \exp\left[-\frac{1}{2}\left(\frac{x-\mu}{\sigma}\right)^2\right], \tag{A.11}$$

where a general amplitude A has been assumed. The parameters A, μ (the mean or expectation of the corresponding Gaussian distribution) and σ (the standard deviation) represent the intensity, central position and shape of the spectrum component. The Gaussian function has been used to fit both the direct current (DC) and low-frequency (LF) components of spectra in this study.

Generalized Gaussian function

The generalized Gaussian (GG) function has one more parameter in the exponent:

$$G(x) = A \exp\left[-\left(\frac{|x-\mu|}{\alpha}\right)^{\beta}\right]. \tag{A.12}$$

With the *shape parameter* β, the function is more flexible in its shape.

The standard deviation is calculated as $\alpha\sqrt{\frac{\Gamma(3/\beta)}{\Gamma(1/\beta)}}$, where $\Gamma()$ is the Gamma function. Since the standard deviation depends on two parameters, complicating implementation of the parameter constraints in the fitting process, we introduce a modified GG function:

$$GG(x) = A \exp\left[-\left(\frac{|x-\mu|}{\sigma}\sqrt{\frac{\Gamma(1/\beta)}{\Gamma(3/\beta)}}\right)^{\beta}\right]. \tag{A.13}$$

This way, the standard deviation simply becomes σ.

The GG function reduces to the Gaussian function when $\beta = 2$, while $\beta = 1$ represents the Laplace distribution which is more peaked and has heavier tails than the Gaussian. The frequently used Lorentzian (Cauchy) function is approximated, in the vicinity of its maximum, by the GG with β between 1 and 2. The GG function has high flexibility and the parameters have a clear interpretation. Figure A.1 shows some typical GG shapes for varying β ($\sigma = 50$). Increasing β, the distribution transitions from a peaked shape with long tails to an almost rectangular shape.

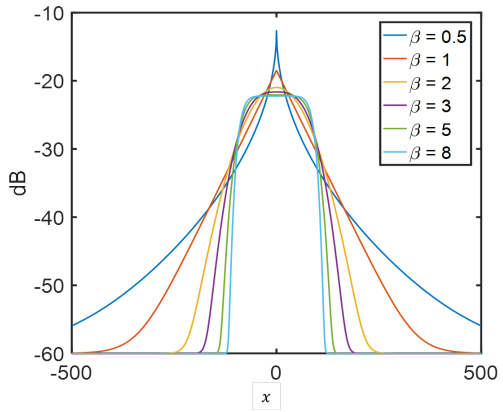

Figure A.1: Examples of GG functions for varying shape parameter β.

Voigt function

The Voigt function is a convolution of a Gaussian function and a Lorentzian function, which has been widely used for fitting purposes in spectroscopy. The function is given by

$$V(x) = \int_{-\infty}^{\infty} G(x')L(x - x')\,\mathrm{d}x', \tag{A.14}$$

where $G(x) = \frac{1}{\sigma\sqrt{2\pi}}e^{-(x-\mu)^2/(2\sigma^2)}$ is the Gaussian PDF and $L(x) = \frac{\gamma}{\pi(x^2+\gamma^2)}$ the centered Lorentzian function. Equivalently, the position parameter μ can be introduced in the Lorentzian function and the centered Gaussian function can be employed. However, in implementing the convolution, calculation of the Faddeeva function is time-consuming. Therefore, in practical applications, an approximate function, called the pseudo-Voigt function is often used, which is a weighted mixture of the Lorentzian and Gaussian function, with weight η:

$$V_p(x) = \eta \cdot L(x) + (1 - \eta) \cdot G(x), \quad 0 \leq \eta \leq 1. \tag{A.15}$$

Taylor function

The Taylor function is the Fourier transform of a specific kind of correlation function. When the correlation function is defined as:

$$F_{\mathrm{corr}}(x) = \exp\left[-k^2u^2\tau^2\left(\frac{x}{\tau} - 1 + e^{-x/\tau}\right)\right], \tag{A.16}$$

defining $\Delta = k^2D = k^2u^2\tau$, where $D = u^2\tau$, the above expression becomes:

$$F_{\mathrm{corr}}(x) = \exp\left[-\Delta(x - \tau + e^{-t/\tau})\right]. \tag{A.17}$$

Then the Taylor function is the Fourier transform of F_{corr} and acquires the following form:

$$T(x) = \mathrm{FFT}\left\{\exp\left[-\Delta_{BB}(t - \tau_{BB} + e^{-t/\tau_{BB}})\right] \times \delta\varphi\right\}, \tag{A.18}$$

where we have introduced the position parameter by adding $\delta\varphi = \exp(i2\pi\mu t)$. The high flexibility of the Taylor function is shown in figure A.2. Specifically, when Δ is relatively large ($\Delta = 1$), the distribution shape can vary from Gaussian to Laplacian. At smaller Δ ($\Delta \simeq 0.1$), the Taylor function resembles the Lorentzian function.

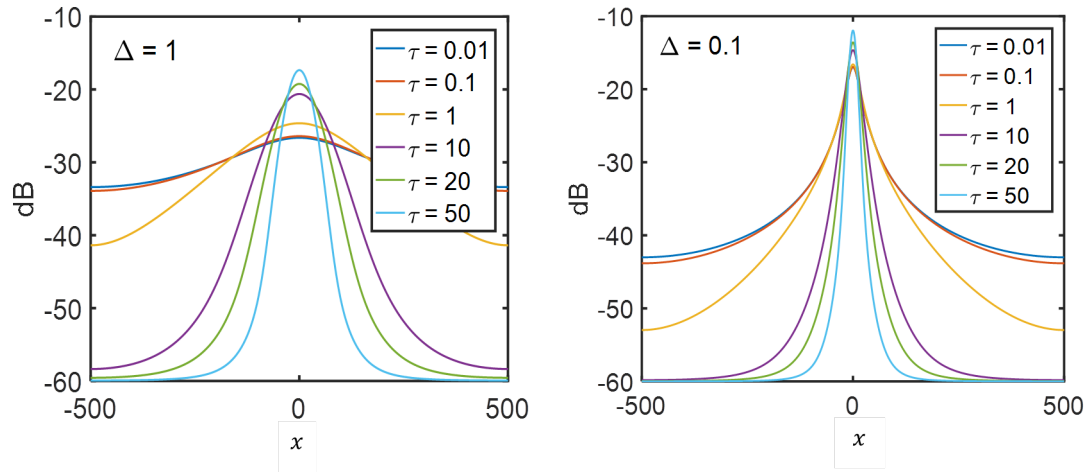

Figure A.2: Examples of Taylor functions with varying τ at two different values of Δ.

Abstract

To systematically study the plasma turbulence in tokamaks, a parametrization method of frequency spectra from the Tore Supra reflectometry database has been developed. The database includes $350,000$ acquisitions obtained from $6,000$ discharges with different heating scenarios. In the parametrization, each spectrum has been decomposed into four component: the direct current component, the low-frequency (LF) fluctuations, the broadband (BB) turbulence and the noise level, and each component has been fitted by a function. Specifically for the BB turbulence component, three different functions have been tested and compared. The generalized Gaussian function and the Taylor function have shown excellent fitting performance. The radial profiles of the BB contribution (E_{BB}) with different edge safety factor have been investigated. In Ohmic plasmas, E_{BB} in the saturated Ohmic confinement regime is observed to be systematically higher than in the linear Ohmic confinement regime. In L-mode plasmas, E_{BB} in the ion cyclotron resonance heating plasmas is globally much higher than in the lower hybrid heating plasmas. To understand the observations, the collisional effects on the modifications of the spectra have also been studied. With the previous kinetic simulation results, a change of the dominating micro-instabilities, i.e., between the trapped electron modes and the ion temperature gradients modes, has been proposed to explain the behaviors of E_{BB}, supported by further database analysis of the density peaking and the LF component. This database study of plasma turbulence motivates more detailed studies by full-wave and gyrokinetic simulations, in order to confirm the link between the modifications of spectra and the micro-instabilities for both Ohmic and L-mode plasmas.

Résumé

L'étude systématique de la turbulence plasma dans les tokamaks, via une méthode de paramétrisation des spectres de fréquence extraits de la base de données de réflectométrie de Tore Supra a été effectuée. Cette base de données est constituée de 350 000 acquisitions obtenues à partir de 6 000 chocs incluant différents scénarios de chauffage. La paramétrisation consiste en une décomposition de chaque spectre en quatre composantes: la composante dite continue, les fluctuations de basse fréquence (BF), la turbulence à large bande en fréquence (BB) et le niveau de bruit où chaque composante a été approchée par une fonction prédéfine. Pour la composante de turbulence BB, trois fonctions différentes ont été testées et comparées. La fonction gaussienne généralisée et la fonction de Taylor ont montré d'excellentes performances dans la plupart des cas. Les profils radiaux de la contribution BB (E_{BB}) pour différents facteurs de sécurité ont été étudiés. Dans les plasmas ohmiques, E_{BB} dans le régime de confinement ohmique saturé est systématiquement plus élevé que dans le régime de confinement ohmique linéaire. Dans les plasmas en mode bas confinement L, E_{BB} dans les plasmas chauffés par une onde à la résonance

cyclotron ionique est globalement beaucoup plus élevé que dans les plasmas chauffés par onde hybride inférieur. Pour comprendre les observations, les effets des collisions sur les modifications du spectre ont également été introduits. En utilisant les résultats de simulations cinétiques, il a été proposé que les micro-instabilités dominantes, c'est-à-dire entre les modes d'électrons piégés et les modes de gradients de température des ions, suffisent pour expliquer le comportement de E_{BB}, ceci étant confortés par une analyse de la base de données de la forme du profil de densité et de la composante LF. Cette base de données sur la turbulence plasma incite à poursuivre des études plus détaillées par simulations des résultats de réflectométrie et gyrocinétiques, afin de confirmer le lien entre les modifications du spectre et les micro-instabilités des plasmas à la fois en mode ohmique et en mode L.